Electromagnetic metagratings for efficient wavefront manipulation

Zhen Tan

Université Paris Nanterre
200 av. de la République
92001 Nanterre Cedex
www.parisnanterre.fr

西安交通大學
XI'AN JIAOTONG UNIVERSITY

Membre de l'université Paris Lumières
École doctorale 139 : Connaissance, langage, modélisation
Laboratoire Energétique Mécanique Electromagnétisme (LEME)

Zhen TAN

Electromagnetic metagratings for efficient wavefront manipulation

Thèse présentée et soutenue publiquement le 07/05/2024
en vue de l'obtention du doctorat de Electronique, optronique et systèmes
de l'Université Paris Nanterre
sous la direction de M. Shah Nawaz Burokur (Université Paris Nanterre)
et de M. Jianjia Yi (Xi'an Jiaotong University)

Jury :

Président :	M. Said ZOUHDI	Professeur, Université Paris-Saclay
Rapporteur :	M. Guido VALERIO	Professeur, Sorbonne Université
Rapporteur :	M. Hexiu XU	Professeur, Air Force Engineering University
Examinateur :	Mme. Juan CHEN	Professeure, Xi'an Jiaotong University
Examinateur :	M. Badr Eddine RATNI	Maître de Conférences, Université Paris Nanterre
Examinateur :	M. Kuang ZHANG	Professeur, Harbin Institute of Technology
Directeur :	M. Shah Nawaz BUROKUR	Maître de Conférences, Université Paris Nanterre
Co-Directeur :	M. Jianjia YI	Professeur, Xi'an Jiaotong University

Acknowledgements

Upon the culmination of this dissertation, the culmination of my doctoral studies will also draw near.

Primarily, I wish to extend my deepest gratitude to my supervisor, Jianjia Yi. Beyond imparting me with profound expertise, he has also guided me in the art of problem analysis and cogitation, as well as the art of navigating the complexities of interpersonal relationships. I am indebted to Jianjia Yi for introducing me to the realm of electromagnetic metamaterials. In the nascent stages of my research, I encountered numerous obstacles, yet Jianjia Yi consistently exhibited unwavering enthusiasm in aiding me in surmounting them.

Concurrently, I wish to express my heartfelt appreciation to another supervisor, Shah Nawaz Burokur. During the duration of my two-year study in France, Nawaz provided invaluable assistance. I shall forever cherish the memory of my initial arrival in France, when Nawaz generously assisted me in resolving the intricacies of securing an apartment, establishing basic amenities such as electricity and water, and addressing the challenges of daily life. As a newcomer in a foreign land, his warmth and support were truly comforting. Moreover, Nawaz offered essential guidance throughout my research endeavors. When I confronted obstacles in my scholarly pursuits, his extensive and specialized research acumen consistently proved instrumental. Our collaboration has resulted in meaningful scientific contributions, for which I am immensely grateful.

I would also like to thank the members of my dissertation committee for their insightful discussions during my defense and extend special thanks to the two reviewers Hexiu Xu and Guido Valerio who provided detailed reports on my work. Their feedback greatly contributed to the improvement of my thesis.

Furthermore, I extend my gratitude to my colleagues within my research group, whose presence has fostered an enriching environment and a conducive research atmosphere. Furthermore, I would like to express my special thanks to LEME (Energetics, Mechanics, Electromagnetism Laboratory) in Paris Nanterre University for giving me the opportunity to study and research in France, during this time I have accomplished a lot of research works, and the persons here have given me a lot of warmth and help, especially Dawei Zhang, who have been very helpful to me in my daily life, and Badreddine Ratni and Nawel Meftah have helped

me a lot with my French university life. I am equally extended my appreciation to Jing Wang, Shan Xuan, Sidi Wang, Ruoyu Dai, and Wei Zhou, who collaborated with me on electromagnetic metagratings in China. Additionally, the positive and diligent work ethic demonstrated by Menglan Lin, Xin Zhao, Jiahui Ji and Ruimeng Zhang within my China research group has also had an indelible, positive impact on my own endeavors.

Finally, I wish to express my profound gratitude to my parents, Zhizhong Tan and Fengying Wang, whose unwavering support and encouragement have quietly guided me throughout the years. Their selfless love, as the embodiment of paternal and maternal devotion, has afforded me the tranquillity of mind requisite for my scholarly pursuits throughout my doctoral journey.

I extend my heartfelt appreciation to the China Scholarship Council for my scholarship support.

To all those who have demonstrated care, provided assistance, and offered unwavering support, I am sincerely grateful.

Table of Contents

Résumé en français

Introduction générale

Au cours du siècle dernier, la prolifération et l'utilisation des ondes électromagnétiques ont eu un impact transformateur sur l'engagement sociétal et l'interaction avec l'environnement. Le contrôle délibéré et la configuration des ondes électromagnétiques ont engendré le développement de nombreuses applications impressionnantes, couvrant les domaines civils et militaires, notamment pour les communications sans fil, la détection et l'imagerie, entre autres. Une stratégie importante pour manipuler les fronts d'ondes électromagnétiques implique la manipulation du milieu physique à travers lequel ces ondes se propagent. L'introduction des métamatériaux au 20ème siècle représente une avancée cruciale dans cette quête. Grâce à un ajustement précis des paramètres des matériaux constitutifs, les métamatériaux présentent des propriétés qui ne sont pas présentes dans les matériaux naturels, permettant ainsi un contrôle précis des ondes électromagnétiques.

Cette thèse de doctorat vise, dans un premier temps, à passer en revue de manière non-exhaustive les avancées antérieures dans le domaine des métamatériaux, en mettant l'accent sur les métamatériaux 2D, communément appelés métasurfaces, qui présentent des capacités notables dans la manipulation des ondes électromagnétiques. Par la suite, la méthodologie avancée de conception des métasurfaces pour la manipulation des fronts d'ondes, en particulier les métaréseaux, sera exposée. Les étapes clés pertinentes pour la conception de métaréseaux seront présentées en détail, incluant la dérivation des coefficients de réflexion et de transmission de Fresnel dans les milieux multi-couches, la modélisation du champ rayonné émanant d'un réseau périodique de ligne de courants et les méthodes pour obtenir l'impédance de charge des fils dans les métaréseaux afin de manipuler les fronts d'ondes. Les hypothèses concernant le choix de la période des métaréseaux par rapport à la couverture angulaire du diagramme de diffraction seront aussi abordées.

De plus, cette thèse englobera une exploration détaillée de diverses techniques de manipulation de fronts d'ondes pour les ondes planes incidentes normales en utilisant respectivement des métaréseaux réfléchissants et transmissifs. La validité et l'efficacité des méthodologies de conception proposées seront rigoureusement évaluées au moyen d'une

combinaison d'analyses fondées sur la simulation numérique et la validation expérimentale. Dans ce qui suit, un exposé détaillé du contenu de chaque chapitre est fourni.

Etat de l'art sur les métamatériaux, métasurfaces et métaréseaux

Depuis 1964, le scientifique soviétique V. G. Veselago a postulé l'hypothèse d'avoir des matériaux à indice de réfraction négatif sur la base de matériaux présentant simultanément une permittivité ε et une perméabilité μ négatives. Ce paradigme, appelé milieu à indice de réfraction négatif ou milieu gaucher en raison de la relation contre-intuitive entre les champs électrique et magnétique, a connu un regain d'intérêt à la fin des années 1990, promulgué par les travaux de J. B. Pendry, qui a proposé des structures telles que des réseaux périodiques de fils métalliques et des résonateurs à anneaux fendus pour obtenir une permittivité et une perméabilité négatives. D. R. Smith a poursuivi ses recherches en fabriquant avec succès des prototypes, validant expérimentalement l'indice de réfraction négatif dans les métamatériaux et la réfraction négative. Des recherches ultérieures menées par Pendry, U. Leonhardt et d'autres ont étendu le domaine d'application des métamatériaux, permettant des manipulations sophistiquées de fronts d'ondes en tirant parti du concept d'optique de transformation.

Cependant, le champ d'application des métamatériaux électromagnétiques tridimensionnels est resté limité en raison de leur profil volumineux et de leur complexité de fabrication. En 2011, F. Capasso et son équipe ont introduit la loi de Snell généralisée, annonçant une nouvelle ère dans la manipulation des ondes électromagnétiques, facilitée par les métamatériaux bidimensionnels communément appelés métasurfaces. Cette approche de conception, connue sous le nom de métasurfaces à gradient de phase, s'appuie sur les principes de l'optique des rayons pour contrôler la déviation du faisceau par un gradient de phase à l'interface entre deux milieux. Comme illustré sur la Figure 0.1(a), les éléments résonants en forme de V avec des angles d'ouverture et des orientations variables sont conçues pour obtenir un contrôle de la phase s'étendant sur 2π. En disposant ces éléments résonants dans un réseau bidimensionnel avec une distribution (ou gradient) de phase prédéterminée, on est en mesure de contrôler les fronts d'ondes électromagnétiques incidents.

Les métasurfaces à gradient de phase permettent la manipulation des ondes électromagnétiques en introduisant un gradient de phase à l'interface entre deux milieux. Cependant, cette approche se heurte à des défis, notamment en ce qui concerne l'efficacité dans la manipulation des ondes dans le cas où il existe une désadaptation d'impédance importante entre ondes entrante et sortante, liée à la différence d'angle entre l'onde incidente et l'onde

sortante (réfléchie ou transmise), ce qui entraîne une diminution de l'efficacité. En 2013, une solution à ce défi a été proposée grâce à au concept de métasurfaces de Huygens. Cette méthodologie novatrice se concentre sur la manipulation indépendante des champs électrique et magnétique pour contrôler les ondes électromagnétiques, comme le montre la Figure 0.1(b). Notamment, l'impédance d'onde est représentée comme le rapport entre le champ électrique et le champ magnétique. Par conséquent, les métasurfaces de Huygens permettent de s'affranchir du problème de désadaptation d'impédance d'onde en concevant avec précision les réponses électriques et magnétiques de ces métasurfaces. En découplant la manipulation des champs électrique et magnétique, les métasurfaces de Huygens offrent une solution intéressante aux limitations d'efficacité associées au désadaptation d'impédance d'onde observée dans les métasurfaces à gradient de phase. Cependant, leur mise en œuvre typique implique souvent des structures multi-couches complexes pour contrôler indépendamment les champs électrique et magnétique des ondes électromagnétiques, ce qui pose des défis importants dans la fabrication et l'application pratique.

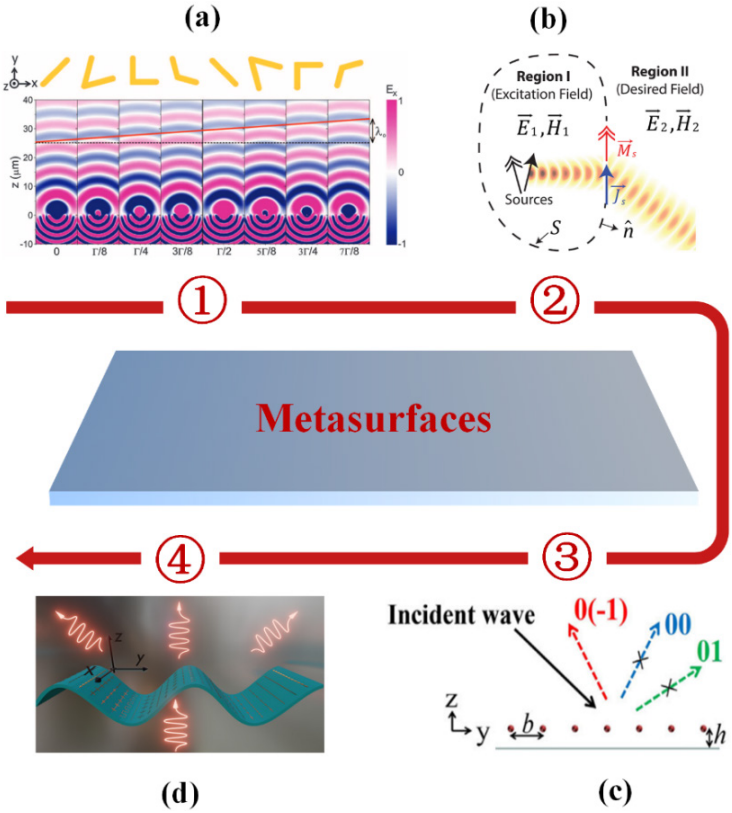

Figure 0.1 : (a) Métasurface composée de cellules unitaires en forme de V avec un gradient de phase de l'ordre de 2π. (b) Le principe de la métasurface de Huygens : les champs électriques et magnétiques sont contrôlés indépendamment pour manipuler les ondes électromagnétiques. (c) Méthodologie de conception des métaréseaux : la réflexion anormale est obtenue en supprimant les modes de diffraction indésirables. (d) Métasurfaces éparses : manipulation de fronts d'ondes arbitraires avec une structure non planaire.

En 2017, le groupe d'A. Alù a introduit un nouveau paradigme de conception connu sous le nom de métaréseaux pour la manipulation de fronts d'ondes, comme illustré sur la Figure 0.1(c). Les métaréseaux sont constitués d'un arrangement éparse d'éléments sub-longueur d'onde polarisables, contrairement aux métasurfaces traditionnelles à gradient de phase et les métasurfaces de Huygens où la structuration des méta-atomes est dense. Cette approche innovante associe des méta-atomes avec les réseaux de diffraction pour obtenir une réflexion anormale en supprimant les modes de diffraction indésirables tout en préservant ceux souhaités. Lors de la manipulation de fronts d'ondes à l'aide des métaréseaux, il est possible d'obtenir une efficacité quasi optimale, même pour des angles de déviation extrêmes. De plus, cette structuration éparse offre des avantages pratiques, rendant les métaréseaux faciles à fabriquer et à déployer dans des scénarios réels. La simplicité de la structure, associée à ses capacités efficaces de manipulation de fronts d'ondes, positionne les métaréseaux comme une solution prometteuse et pratique pour réaliser des déviations désirées de faisceau et d'autres applications liées au contrôle de fronts d'ondes.

Une manipulation efficace du front d'onde avec des métaréseaux périodiques nécessite deux conditions préalables : l'onde incidente doit être une onde plane et la structure de métaréseau doit être plane. En 2020, Popov et ses co-auteurs ont introduit une méthode de conception de métasurfaces éparses, comme le montre la Figure 0.1(d). La conception de métasurfaces éparses exploite une analyse basée sur les lignes de courant semblable à celle des métaréseaux, à la différence que l'onde incidente peut être non-plane. De plus, la méthodologie exploite l'utilisation d'un logiciel de simulation numérique, ce qui permet de l'appliquer aux structures non planaires.

Bases pour la méthodologie de conception analytique

Dans cette thèse, je me concentre principalement sur la conception des métaréseaux, où l'onde incidente est une onde plane et le métaréseau est une structure périodique plane, ce qui facilite l'expression et le calcul des champs dans la conception sous une forme analytique sans avoir recours à des simulations numériques intensives. Quatre aspects clés régissant la conception et l'analyse des métaréseaux seront examinés dans le chapitre 2, brièvement décrits ci-dessous :

- Analyse de la réflexion et de la transmission : un système de métaréseau peut être conceptualisé comme un système multi-couches, ce qui nécessite un examen approfondi de la réflexion et de la transmission des ondes électromagnétiques au sein de ce système,

comme illustré sur la Figure 0.2(a). Le chapitre commence par une analyse et une dérivation des coefficients de réflexion et de transmission de Fresnel, adaptés respectivement aux métaréseaux réfléchissants et transmissifs.

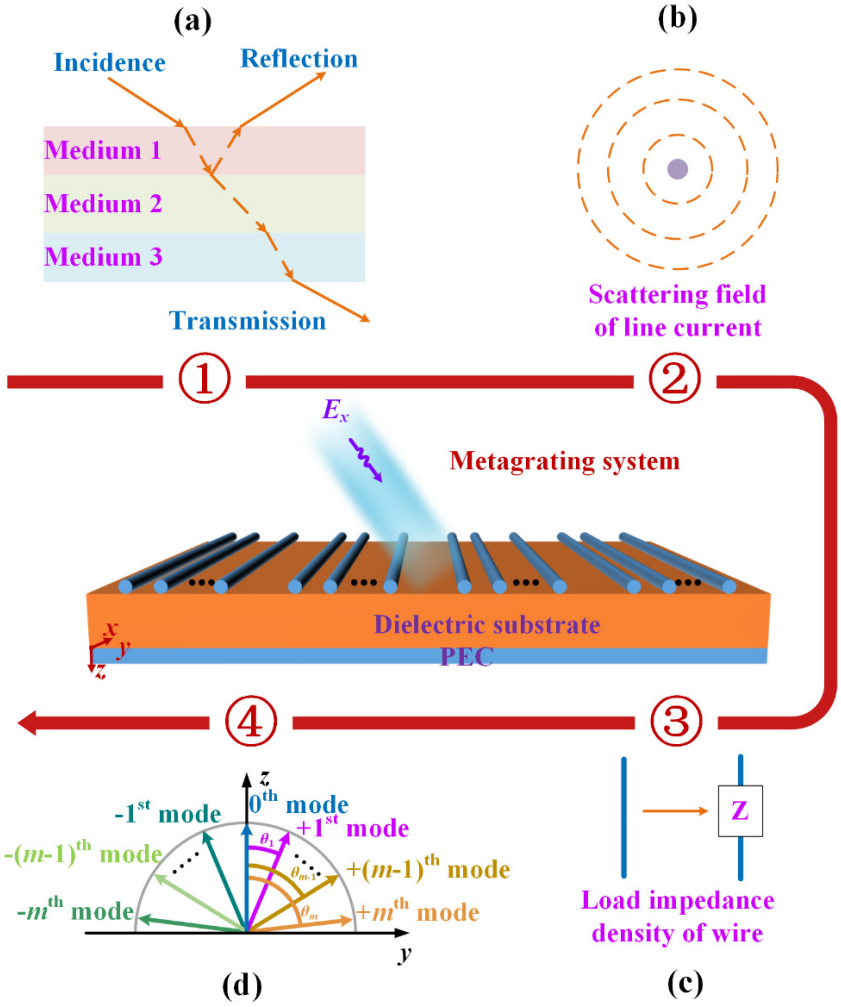

Figure 0.2 : Analyse des caractéristiques électromagnétiques dans les métaréseaux. (a) Réflexion et transmission dans les milieux multicouches. (b) Champ diffusé d'un réseau de lignes de courant périodique. (c) Densité d'impédance de charge du métaréseau requise pour réaliser la manipulation de fronts d'ondes. (d) Couverture angulaire du diagramme de diffraction d'un métaréseau par rapport à la taille de la période.

- Caractéristiques de rayonnement des réseaux de courants de polarisation : les métaréseaux permettent de manipuler les fronts d'ondes en synthétisant les ondes incidentes et les ondes diffractées. Ces derniers émanent du rayonnement secondaire des courants de polarisation générés par les ondes incidentes dans les éléments polarisables du métaréseau, comme le montre la Figure 0.2(b). Par conséquent, le chapitre se penche sur l'analyse des champs rayonnés provenant de lignes de courant seuls, en étendant cette analyse pour caractériser la distribution spatiale des champs rayonnés pour des réseaux de lignes de courant périodiques uniformes et non uniformes.

- Conception de la structure : après avoir déterminé les courants requis pour la manipulation de fronts d'ondes souhaitée, l'attention se porte sur la conception du métaréseau pour réaliser ces courants dans des conditions d'incidence spécifiques. Cela nécessite une analyse des caractéristiques d'impédance de charge des éléments polarisables du métaréseau et le calcul de la densité d'impédance de charge correspondante via la loi d'Ohm, comme illustré sur la Figure 0.2(c). De plus, il est important d'imposer une contrainte d'une partie réelle nulle de l'impédance de charge pour une manipulation passive et sans perte de fronts d'ondes.
- Sélection de la taille de la période : le nombre et l'angle des modes de diffraction d'un métaréseau dépend de sa période, comme le montre la Figure 0.2(d). Par conséquent, le choix de la période appropriée a une importance considérable. Le chapitre 2 entreprend une analyse de la relation entre la couverture angulaire du diagramme de diffraction des métaréseaux et la taille de la période, fournissant une base théorique pour la conception de dispositifs spécifiques dans les chapitres suivants.

Le chapitre 2 offre une exploration complète des caractéristiques électromagnétiques et des considérations analytiques qui font partie intégrante de la conception et de l'analyse des métaréseaux, jetant les bases de la conception et de la mise en œuvre détaillées des dispositifs proposés dans les chapitres suivants.

Métaréseaux réfléchissants pour la manipulation de front d'onde

S'appuyant sur la théorie fondamentale des métaréseaux développée dans le chapitre 2, le chapitre 3 est dédié à la conception et la mise en œuvre d'une manipulation efficace de fronts d'ondes à l'aide de métaréseaux réfléchissants. Cette démarche s'articule autour de quatre axes distincts :

- Génération d'un faisceau unique : l'accent est d'abord mis sur la génération d'un faisceau unique, comme le montre la Figure 0.3(a). En supprimant sélectivement les modes de diffraction indésirables, la conception vise à ne conserver qu'un seul mode correspondant à l'angle de sortie du faisceau souhaité, ce qui permet d'obtenir une réflexion anormale. Le chapitre 3 détaille les calculs analytiques spécifiques pour atteindre cet objectif.
- Génération de faisceaux multiples : au-delà de la génération d'un faisceau unique, le chapitre 3 traite les complexités pour la génération de multifaisceaux, comme illustré sur la Figure 0.3(b). La génération de multifaisceaux nécessite non seulement la

suppression de modes de diffraction non désirés, mais aussi un contrôle précis de la distribution d'énergie des différents modes de diffraction. La méthodologie détaillée, ainsi que des exemples de conceptions à deux et trois faisceaux avec des rapports de puissance réglables, sont présentés.

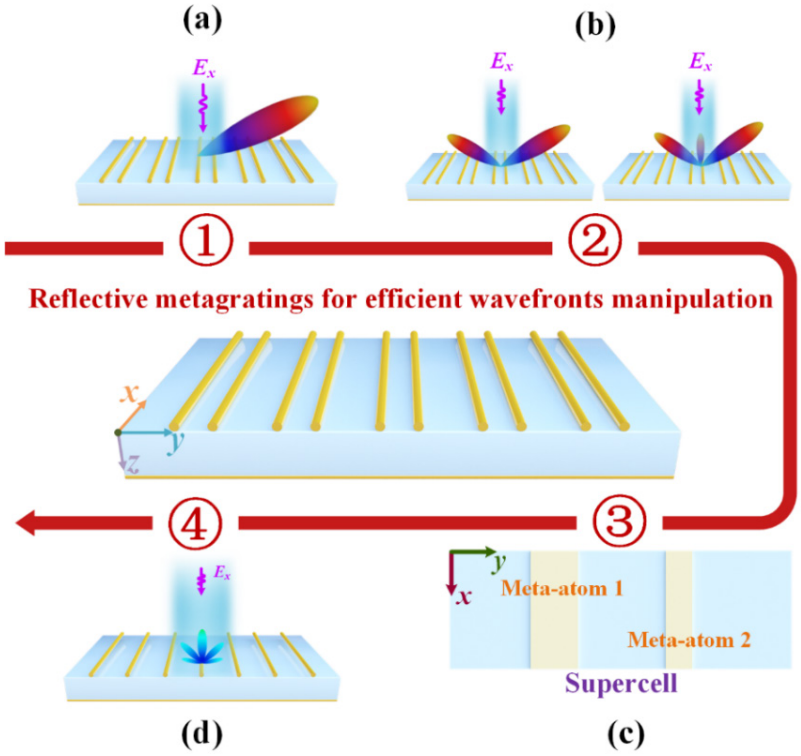

Figure 0.3 : Métaréseaux réfléchissants pour une manipulation efficace des fronts d'ondes. (a) Génération d'un faisceau unique. (b) Génération de faisceaux multiples. (c) Exemple d'une supercellule à impédance de charge nulle. (d) Absorption des ondes électromagnétique par un métaréseau réfléchissant.

- Métaréseaux réfléchissants à impédance de charge nulle : les métaréseaux traditionnels nécessitent souvent des éléments polarisables avec des impédances de charge spécifiques, généralement mis en œuvre par des structures capacitives ou inductives. Cependant, à des fréquences plus élevées telles que les bandes de fréquences millimétriques ou le térahertz, la complexité de ces structures pose des défis de fabrication. Pour pallier à ce problème, je propose le concept de métaréseaux à impédance de charge nulle. La supercellule de ces métaréseaux, comme le montre la Figure 0.3(c), permet une manipulation de fronts d'ondes à l'aide de structures microrubans simples, offrant une solution viable pour la conception de métaréseaux à hautes fréquences.
- Absorption électromagnétique efficace : les métaréseaux réfléchissants peuvent également faciliter une absorption électromagnétique efficace, comme le montre la

Figure 0.3(d). En supprimant efficacement tous les modes de diffraction de propagation, l'absorption des ondes électromagnétiques peut être réalisée. Je présente les principes de conception permettant d'obtenir une absorption parfaite des ondes électromagnétiques avec un métaréseau, ainsi qu'une analyse complète de l'impact des différentes configurations structurelles sur la bande passante d'absorption.

En résumé, le chapitre 3 fournit une exploration complète des métaréseaux réfléchissants pour une manipulation efficace de fronts d'ondes, englobant la génération de faisceaux, les métaréseaux à impédance de charge nulle et les mécanismes d'absorption électromagnétique efficace.

Métaréseaux transmissifs pour la manipulation de front d'onde

Après l'exploration de la conception d'une manipulation efficace de fronts d'ondes par le biais de métaréseaux réfléchissants dans le chapitre 3, le chapitre 4 est dédié aux métaréseaux transmissifs, qui présentent des modes de diffraction dans les moitiés supérieure et inférieure de l'espace. Par conséquent, la manipulation du front d'onde avec des métaréseaux transmissifs englobe un spectre plus large, mais implique une plus grande complexité de conception en raison du nombre accru de modes de diffraction et des exigences structurelles complexes.

- Génération d'un faisceau unique : le chapitre 4 commence par la génération d'un faisceau unique, comme illustré sur la Figure 0.4(a). Cependant, les métaréseaux transmissifs présentent à la fois des modes de diffraction en réflexion et en transmission, ce qui permet de réaliser non seulement une réflexion anormale, mais aussi une réfraction anormale. Le chapitre détaille comment supprimer les modes de propagation indésirables pour obtenir le rayonnement souhaité.
- Génération de faisceaux multiples : le chapitre 4 présente aussi la génération de faisceaux multiples, comme illustré sur la Figure 0.4(b). En composant la distribution d'énergie pour les modes diffraction en réflexion et en transmission, il est possible de réaliser un large éventail de scénarios de génération multifaisceaux. Par exemple, la distribution d'énergie se concentrant uniquement sur les modes de diffraction en transmission permet une division du faisceau du même côté, tandis que la prise en compte complète des modes de diffraction en réflexion et en transmission facilite la division du faisceau dans les deux moitiés de l'espace.
- Absorption électromagnétique : le chapitre 4 se penche également sur l'absorption électromagnétique à l'aide de métaréseaux transmissifs, comme le montre la Figure

0.4(c). Comme pour les métaréseaux réfléchissants, la suppression de tous les modes de diffraction permet une absorption unidirectionnelle des ondes. De plus, les métaréseaux transmissifs peuvent être excités à la fois de l'avant et de l'arrière, ce qui permet de réaliser une absorption d'ondes bidirectionnelle en tenant compte simultanément de l'absorption des deux côtés.

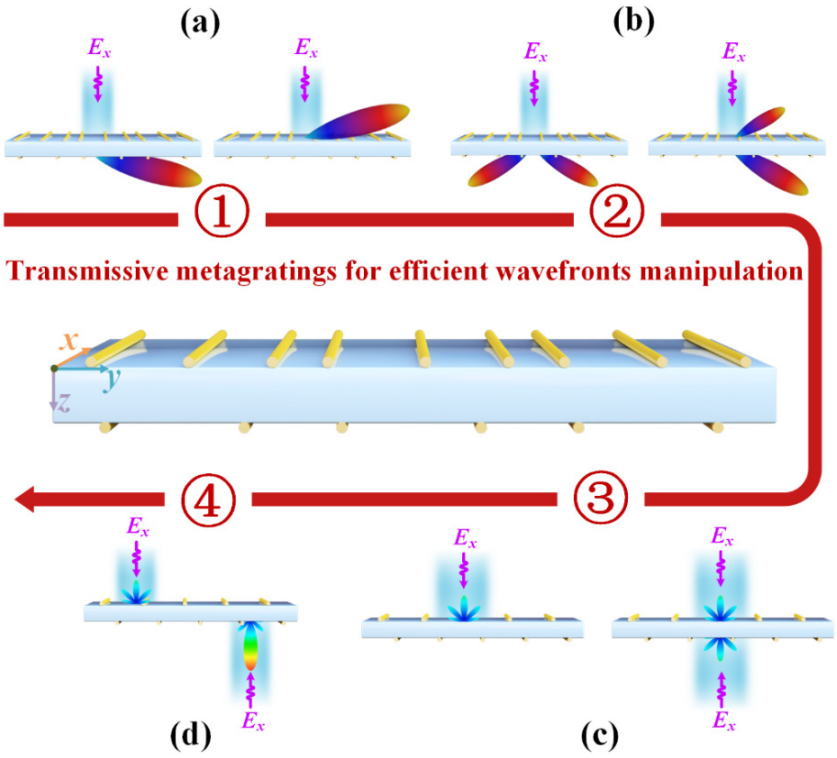

Figure 0.4 : Métaréseaux transmissifs pour une manipulation efficace des fronts d'ondes. (a) Génération d'un faisceau unique. (b) Génération de faisceaux multiples. (c) Absorption d'ondes unidirectionnelle et bidirectionnelle. d) Absorption et réflexion asymétriques.

- Métaréseaux de Janus : cette section explore la manipulation de fronts d'ondes adaptée à différentes directions d'excitation, appelées métaréseaux de Janus. En examinant diverses combinaisons de transmission, de réflexion et d'absorption, la faisabilité d'avoir des fonctionnalités asymétriques est étudiée. Le chapitre se termine par la conception d'absorption/réflexion asymétrique, comme illustré sur la Figure 0.4(d), à la suite d'une analyse théorique rigoureuse.

En résumé, le chapitre 4 fournit une exploration approfondie des métaréseaux transmissifs pour une manipulation efficace de fronts d'ondes, englobant la génération de faisceau unique et de faisceaux multiples, l'absorption électromagnétique et les métaréseaux Janus pour la mise en œuvre de fonctionnalités en fonction de la direction de l'onde incidente.

Conclusions

En conclusion, cette thèse est dédiée au domaine des métaréseaux, présentant un cadre analytique complet pour la conception de techniques fondamentales de manipulation de fronts d'ondes, incluant la réflexion et la réfraction anormales, la division de faisceau, l'absorption unidirectionnelle et bidirectionnelle d'ondes, ainsi que l'absorption/réflexion asymétrique. L'objectif principal est d'établir une méthodologie de conception intuitive pour relever les défis associés à la complexité des approches traditionnelles basées sur l'optimisation via des simulations numériques intensives.

À travers l'exploration des métaréseaux réfléchissants et transmissifs, cette thèse a démontré leur efficacité dans la manipulation de fronts d'ondes, vérifiées par des simulations rigoureuses et des validations expérimentales. En établissant une base théorique solide pour la conception de métaréseaux, ce travail fait non seulement progresser la compréhension théorique, mais a également des implications significatives pour les applications pratiques dans le contrôle de rayonnement électromagnétique.

Pour le futur, l'avenir offre des perspectives prometteuses pour des solutions innovantes et de nouvelles avancées dans le domaine des métaréseaux. Les efforts continus dans ce domaine permettront de produire de nouvelles idées et percées, ouvrant potentiellement de nouvelles voies pour des applications transformatrices dans divers domaines nécessitant un contrôle précis des ondes électromagnétiques. Avec les progrès continus et les collaborations interdisciplinaires, le potentiel des métaréseaux pour révolutionner le contrôle du rayonnement reste vaste et passionnant.

General introduction

Throughout the past century, the proliferation and utilization of electromagnetic waves have brought a transformative impact on the way individuals live and are engaged with the world. The deliberate control and tailoring of electromagnetic waves have led to the development of numerous impactful civilian and military applications, such as wireless communications, sensing, radar detection, imaging, and more. A prominent approach to electromagnetic wavefront control involves manipulating the physical medium through which electromagnetic waves propagate. The introduction of the concept of metamaterials in the 20th century marked a significant leap in this endeavor. Through meticulous adjustment of constituent material parameters, metamaterials acquire properties not found in natural materials, enabling intricate control over electromagnetic waves.

As metamaterials have evolved, a two-dimensional counterpart has emerged, known as metasurfaces, possessing also high capabilities in electromagnetic wave control. Notably, their low-profile features facilitate cost-effective fabrication and seamless integration into various wavefront manipulation applications. The evolution of metasurfaces has seen diverse developments categorized by different design approaches:

Phase Gradient Metasurfaces (2011): The introduction of the generalized Snell‘s law in 2011 marked a pivotal milestone in electromagnetic wave tailoring using electromagnetic metasurfaces. These metasurfaces, known as phase-gradient metasurfaces, operate on the ray optics method, controlling beam deflection by designing phase gradients on the surface. However, a drawback lies in the wave impedance mismatch between incident and outgoing waves, resulting in low efficiency for large angle differences.

Huygens Metasurfaces (2013): In 2013, the Huygens metasurface design method was proposed, enabling beam deflection by independently controlling the electric and magnetic fields. This approach resolves the efficiency problem by designing the wave impedance through the electric-to-magnetic field ratio. Nevertheless, it requires at least two layers of complex structures, often leading to mutual interference. To mitigate this issue, a third layer is introduced, complicating the overall structure.

Metagratings (2017): The metagrating design method, based on the diffraction grating approach, was introduced in 2017. It achieves beam deflection by suppressing unwanted diffraction modes,

retaining only the desired diffraction mode, thereby achieving optimal efficiency. Importantly, this design only necessitates consideration of load impedance, resulting in a simple and sparse structure that is practical for implementation.

Sparse Metasurfaces (2020): Built upon the sparse arrangement design of metagratings, the concept of sparse metasurfaces was proposed in 2020. Its distinctive feature of not being constrained by the excitation source enhances flexibility in practical applications, allowing effective wavefront control through a versatile excitation source. However, the design of sparse metasurfaces necessitating the use of numerical software for calculation of Green's function in complex environments and optimization procedures, seems to be unfeasible using fully analytical procedures.

This thesis is dedicated to the pursuit of fully analytical design of metagratings, with a primary focus on achieving fundamental wavefront control encompassing anomalous reflection, anomalous refraction, beam splitting, uni- and bi-directional wave absorption and asymmetrical reflection and absorption. The objective is to address the prevailing challenges associated with the intractability and complexity of these designs when employing optimization algorithms. This PhD thesis concentrates on the design of various categories of these wavefront manipulations based on both reflective and transmissive metagratings. The thesis comprises five chapters structured as follows. Chapter 1 introduces the origin and development of metamaterials and metasurfaces. It deals with the evolutionary history of various metasurfaces, detailing the steps researchers have taken to achieve efficient wavefront manipulation of electromagnetic waves through different methods. Chapter 2 conducts a detailed analysis of the reflection and transmission of electromagnetic waves within metagratings. This encompasses the examination of the radiation characteristics of the metagrating's line current arrays and the intricate relationship between the energy distribution of each diffraction mode of the metagrating and the position/load impedance of the meta-atoms. Detailed theoretical formulas are derived, providing a robust theoretical foundation for subsequent chapters. Chapter 3 presents a series of fully analytical designs for electromagnetic wavefront manipulation based on reflective metagratings. This includes the design and simulation of beam deflection and beam splitting. The introduction of the zero load-impedance metagrating concept is followed by the design, simulation, and experimental verification of beam splitting under varying power ratios and angles in the millimeter wave frequency. The chapter concludes with the design of an electromagnetic wave absorber, discussing in detail the influence of meta-atoms with different structures on absorption bandwidth. Chapter 4 extends the analytical designs to transmissive metagratings. It includes the design of extreme angle anomalous reflection and

anomalous refraction based on transmissive metagratings, as well as the design of same-side and opposite-side beam splitting with arbitrary power ratios. Designs for unidirectional and bidirectional wave absorption are also presented. The chapter concludes with an analysis of the feasibility of a Janus metagrating design with different functionalities when it is illuminated from different sides. The last part concludes the thesis by summarizing the work done in the different chapters and by proposing some ideas for further exploration in the field of metagratings.

This thesis has explored the concept of metagratings and their fully analytical designs for fundamental wavefront control. The pursuit of these objectives aimed to overcome the existing challenges associated with the complexity and intractability of designs that traditionally rely on optimization algorithms.

Chapter 1
State-of-the-art in metamaterials and metasurfaces

Contents

1.1 Introduction

The manipulation of electromagnetic waves has always been the focus of attention of academic scientists and industrial engineers. It plays an extremely wide range of roles not only in the science of far-reaching research value, but also in wireless communication systems. However, the relatively fixed electromagnetic parameters of natural materials have kept the ability to control electromagnetic waves within a limited range. It was not until the emergence of the concept of electromagnetic metamaterials that the development of wave control took a great step forward. Metamaterials are composed of periodic or non-periodic arrangement of sub-wavelength artificial unit cells of specific geometrical shapes. They provide a novel method for designing and manipulating electromagnetic waves. The emergence of electromagnetic metamaterials has greatly compensated for the lack of electromagnetic properties of natural materials.

The design methodology of metamaterials has also been continuously developed and updated. In this chapter, I will introduce succinctly the concept of metamaterials and its main features. With the goals of efficient manipulation of electromagnetic waves and easy fabrication and integration, metamaterials have evolved from three-dimensional (3D) structures to two-dimensional (2D) structures, known as metasurfaces, which can be categorized into different types: phase-gradient metasurfaces, Huygens metasurfaces, metagratings, and sparse metasurfaces. These types of metasurfaces will be introduced one by one, and finally a particular attention will be paid to the current research status of metagratings, which will be studied in the framework of this thesis.

1.2 Metamaterials

To understand what metamaterials are, we must first start with the prefix “meta”, which comes from the Greek word “beyond”. As the word implies, metamaterials are not natural materials and their properties go beyond those of natural materials. They are materials whose structural properties have been artificially and judiciously engineered. Natural materials are generally made up of a large number of microstructures (atoms or molecules), and the nature of these microstructures themselves and the way they are arranged in space determine the basic properties of these materials. The electromagnetic properties of conventional materials are mainly described by two parameters, permittivity and permeability, which reflect the ability of

the materials to respond to an applied electric and magnetic field, respectively. The permittivity and permeability of natural materials are fixed and cannot be changed. On the other hand, the progress of science and technology has promoted the development of various materials, such as nanomaterials, ceramics, polymers, etc. However, in terms of electromagnetic properties, their permittivity and permeability are basically in the range of $\varepsilon \geq 1$ and $\mu = 1$, which are still insufficient to effectively manipulate the propagation of electromagnetic waves.

In 1964, the Soviet scientist V. G. Veselago wrote an article in Russian, which was then translated in English in 1968, to analyse the negative refractive index characteristics of light propagating in a medium with permittivity ε and permeability μ less than 0 at the same time (this medium is also known as a negative refractive index medium or left-handed medium due to the left-handed relationship of the electric field, the magnetic field and the wave vector directions) [1]. However, this theoretical analysis did not attract attention in the scientific community at that time, because there is no such a negative refractive index material in nature.

More than thirty years later, J. B. Pendry from Imperial College in the United Kingdom rethought this issue. Considering the microwave band has relatively low fabrication requirements for artificial medium, he achieved the realization of negative permittivity and negative permeability materials in the microwave band by metals wires [2] and split ring resonators (SRRs) [3], respectively. This catching the attention of D. R. Smith. Smith successfully demonstrated a negative refractive index medium in 2001 by coupling wire medium with split ring resonators, sparking widespread interest in metamaterials [4].

Pendry's 2006 theory of transformation optics revolutionized electromagnetic metamaterial design [5]. This method employs coordinate transformations to control wave propagation by altering the refractive index. Meanwhile, U. Leonhardt proposed an alternative based on optical conformal mapping [6]. Pendry's approach, simpler in derivation, transformed complex computational problems into spatial coordinate transformations.

Transformation optics paved the way for diverse metamaterial applications. Schurig *et al*. used split ring resonators to create a two-dimensional columnar electromagnetic cloak [7], exemplifying the potential for wavefront manipulation in devices such as cloaks, rotators, tapers, antennas, and lenses. This transformative concept expanded the scope of electromagnetic wave control.

1.3 Metasurfaces

The limitations of three-dimensional electromagnetic metamaterials, characterized by their

high profile and cost, have led to the exploration of planar alternatives known as electromagnetic metasurfaces. These metasurfaces, arranged in a two-dimensional plane either periodically or non-periodically, have demonstrated exceptional control over electromagnetic waves. Their key advantages include greater flexibility in fabrication and design, cost-effectiveness, and the potential for miniaturization.

In contrast to three-dimensional metamaterials, metasurfaces cannot be effectively described using permittivity and permeability due to their ultra-thin thickness. Instead, their properties are better characterized in terms of surface impedance or admittance. Consequently, novel characterization methods have been proposed to accurately capture the distinctive features of electromagnetic metasurfaces.

Moving forward, I will delineate the two predominant traditional approaches to metasurface design.

1.3.1 Phase gradient metasurfaces

In 2011, Capasso and his research team introduced the groundbreaking concept of generalized Snell's law, marking a significant milestone in the manipulation of electromagnetic waves through metasurfaces [8]. This design methodology, often referred to as phase gradient metasurfaces, operates on the principles of ray optics. It controls beam deflection by strategically designing varying phase gradients at the interface between two media.

As depicted in Figure 1.1, the metasurface incorporates V-shaped units characterized by distinct opening angles to modulate the phase response across the 2π spectrum. Through the spatial arrangement of these V-shaped units on a two-dimensional plane with either a gradient or specific phase distribution, the metasurface achieves functionalities such as anomalous reflection and refraction of incident electromagnetic waves. This innovative design paradigm has paved the way for novel approaches in controlling electromagnetic waves with metasurfaces, offering a versatile and efficacious means of realizing desired wavefront control.

The conceptual framework established by the generalized Snell's law and phase gradient metasurfaces has been pivotal in driving advancements in the design of electromagnetic wave manipulation devices [9–11]. As illustrated in Figure 1.2(a), the employment of phase gradient metasurfaces facilitates the conversion of propagating waves into surface waves [12], Traditional devices encounter challenges in effecting this conversion owing to the momentum mismatch between plane waves and surface waves. However, through gradient-index metasurfaces, the conversion of propagating waves to surface waves is rectified by the

reflection-phase gradient, thereby achieving near-perfect conversion across all incident angles.

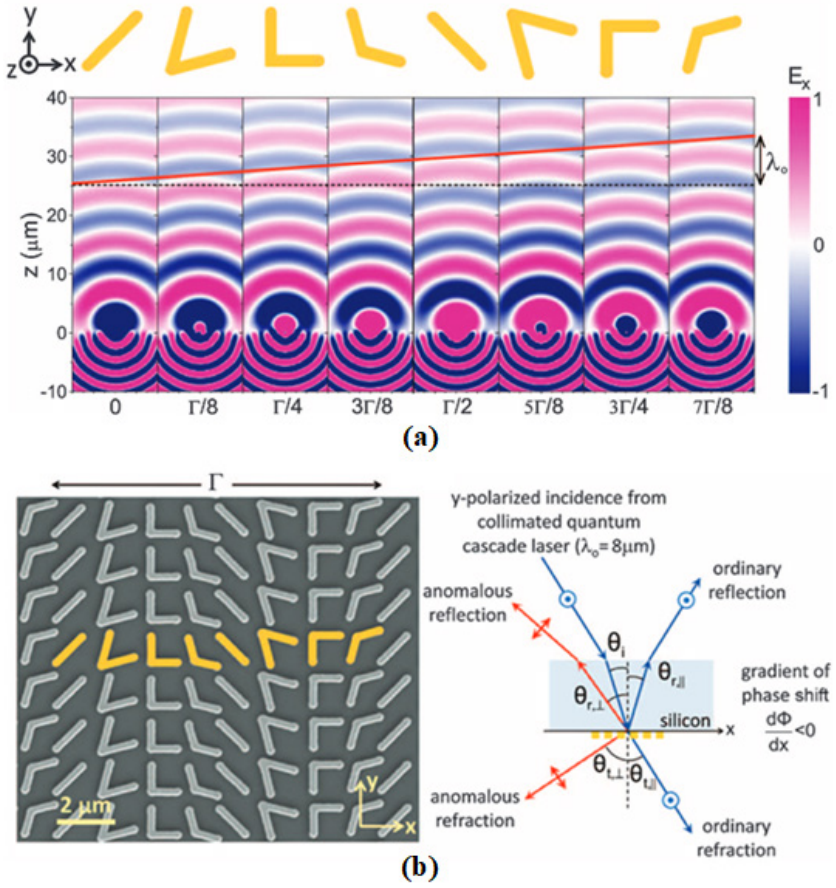

Figure 1.1: (a) Metasurface composed of V-shaped unit cells with gradient phase distribution in the 2π range. (b) Gradient phase allows to realize anomalous reflection/refraction [8].

Furthermore, the realization of the ultra-high efficiency photonic spin Hall effect [13], depicted in Figure 1.2(b), necessitates meticulous analysis of Jones matrices by researchers to establish criteria for designing metasurfaces capable of attaining high-efficiency PSHE. Two practical meta-atom designs are proposed: one leveraging mirror symmetry and the other exploiting asymmetrical responses, as demonstrated in Figure 1.2(c) and Figure 1.2(d). Meta-atoms exhibiting symmetry along specific axes streamline the design and fabrication process, interacting predictably with electromagnetic waves upon illumination, thereby enabling efficient manipulation of spin-polarized photons. Conversely, certain meta-atoms eschew reliance on mirror symmetry, manifesting asymmetrical responses to incident electromagnetic waves, leading to diverse light interactions contingent upon the direction of incidence and polarization. By finely engineering the asymmetry of these meta-atoms, researchers can exert precise control over the spin-dependent characteristics of scattered light, facilitating efficient photonic spin manipulation. Moreover, phase-gradient metasurfaces find applications in

ultrathin invisibility cloaks, polarization-dependent light splitting, and various other domains [14].

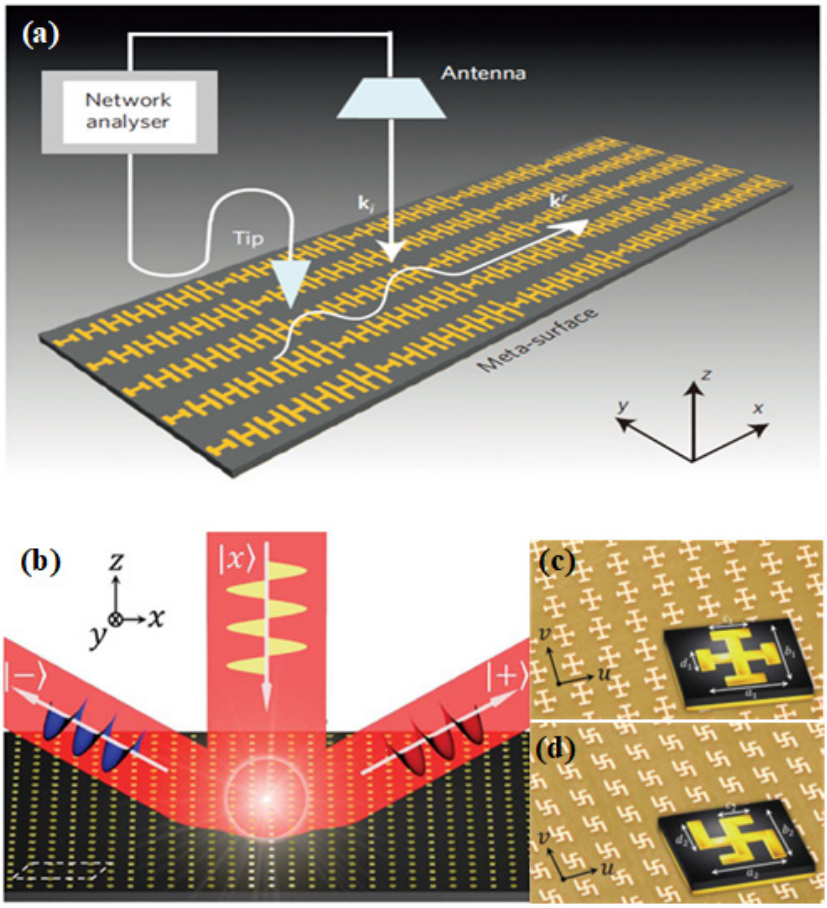

Figure 1.2: (a) Conversion of plane waves to surface waves facilitated by phase gradient metasurfaces and the associated measurement methodology [12]. (b) Linearly polarized incident beam undergoing split into two spin-polarized reflection beams propagating towards two off-normal directions, with complete disappearance of the specular reflection mode [13]. (c) Meta-atom employing mirror symmetry. (d) Meta-atom utilizing asymmetrical responses.

1.3.2 Huygens metasurfaces

The phase gradient metasurfaces previously discussed achieve manipulation of electromagnetic waves by introducing varying phases at the interface between two media. However, this approach encounters a potential challenge that can significantly impact the efficiency of wave manipulation under certain circumstances, primarily stemming from the impedance mismatch between incoming and outgoing waves. This impedance mismatch becomes particularly pronounced when there is a substantial disparity in angle between the outgoing and incident waves, resulting in decreased efficiency.

In 2013, a solution to this challenge was proposed through the introduction of the Huygens

metasurface design method [15]. This innovative approach focuses on controlling electromagnetic waves by independently and separately manipulating the electric and magnetic fields, as depicted in Figure 1.3(a). Notably, the wave impedance is characterized as the ratio of the electric field to the magnetic field. Consequently, Huygens metasurfaces mitigate the wave impedance mismatch issue by meticulously engineering the electric and magnetic responses of the meta-atoms depicted Figure 1.3(b). The practical fabrication of Huygens metasurfaces involves arranging copper traces on a dielectric substrate into specific patterns to achieve the desired electric and magnetic field responses, potentially necessitating multiple layers of such metasurfaces to be laminated, as illustrated in Figure 1.3(c).

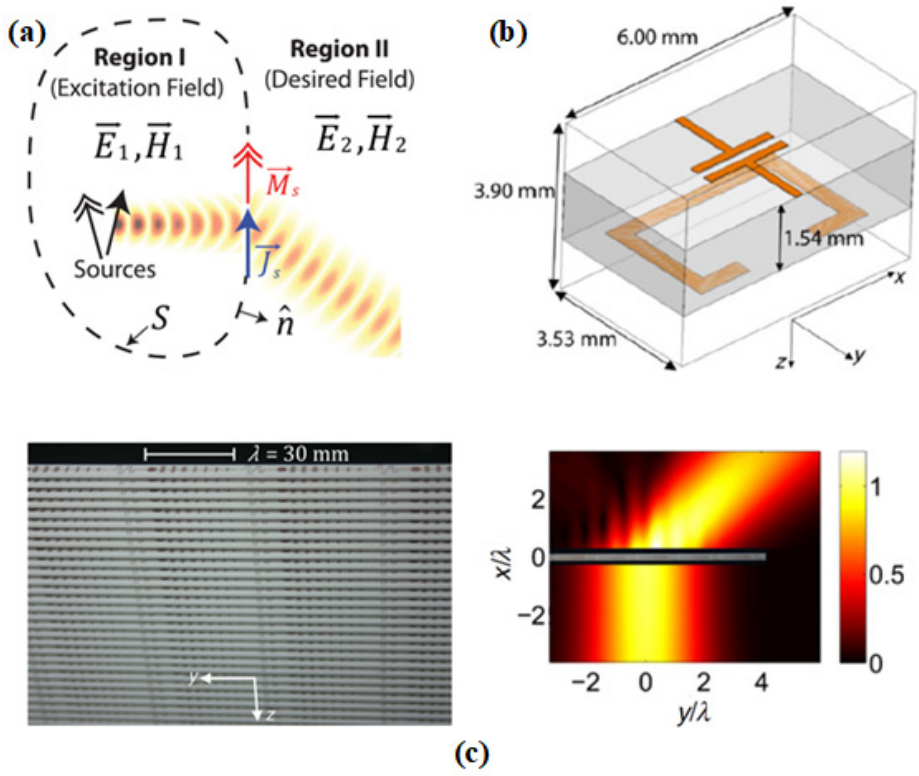

Figure 1.3: (a) Huygens metasurface principle: independent control of electric and magnetic fields to achieve manipulation of electromagnetic waves. (b) Huygens unit cell: the resonator on the upper surface controls the electrical response, while the one on the lower surface controls the magnetic response. (c) Fabricated Huygens metasurface prototype with a multi-layer structure for anomalous refraction and the corresponding measured near-field results [15].

The near-field measurement results depicted in Figure 1.3(c) demonstrate the metasurface's efficient realization of anomalous refraction. By decoupling the control of electric and magnetic fields, Huygens metasurfaces offer a solution to the efficiency limitations associated with the wave impedance mismatch observed in phase gradient metasurfaces. This method enhances the adaptability and effectiveness of metasurface-based wave manipulation

in scenarios with significant disparities in angle between incident and outgoing waves [16].

The widely adopted approach for designing Huygens metasurfaces involves specifying the fields on either side of the metasurface according to the desired field transformation. The equivalence principle, embodied by the generalized sheet transition conditions, is then applied to derive the requisite electric surface impedance and magnetic surface admittance. These parameters induce the necessary surface currents to support the desired field discontinuity [17]. Once the macroscopic impedance modulation is determined, subwavelength elements with electric and magnetic responses are designed, typically utilizing full-wave simulations.

Subsequently, a lookup table is constructed, associating meta-atoms with varying geometrical parameters to their effective electric surface impedance and magnetic surface admittance [18]. This lookup table serves as a reference for the microscopic implementation of the metasurface. The designed subwavelength elements are then employed for the microscopic realization of the Huygens metasurface.

Researchers have successfully employed this methodology to develop a variety of wave-manipulating Huygens' metasurfaces, enabling engineered refraction and focusing [19,20], nonreciprocal one-way propagation [21], asymmetrical reflection [22] and polarization control [23]. Notably, converting an arbitrary excitation source into a desired directional radiating wave holds significant promise in the realm of future wireless communication [24]. By expressing the fields via their plane-wave spectrum and leveraging the slowly-varying envelope approximation, semianalytical formulas for the scattered fields can be derived to prescribe the surface reactance required for metasurface implementation. Subsequently, the arbitrary source can be converted into the desired directional radiation, such as converting the line current source excitation into 30° and 60° radiation, as exemplified in Figure 1.4(a). When such a Huygens metasurface is applied to an antenna, near-perfect aperture efficiency can be achieved [25]. The fabricated antenna, as depicted in Figure 1.4(b), bears resemblance to a typical shield Fabry-Perot leaky wave antenna, featuring an electric line source surrounded by three PEC walls and a Huygens metasurface replacing the standard partially reflecting surface. By invoking the equivalence principle and evaluating the electric surface impedance and magnetic surface admittance required to support the resultant field conversion, simulated and measured antenna patterns, shown in Figure 1.4(b), demonstrate an aperture efficiency of over 90%. This achievement, despite the presence of inevitable external environmental influences, provides a robust design foundation for realizing highly directional beam antennas in future applications.

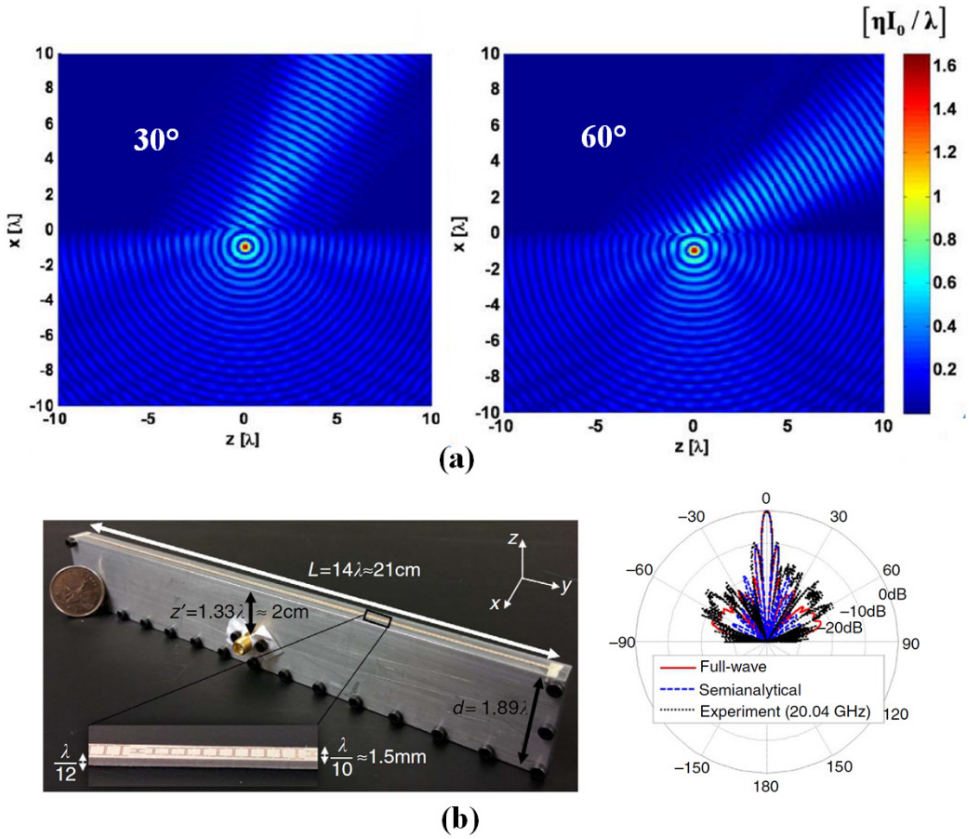

Figure 1.4: (a) Utilizing Huygens' principle to convert electric line source excitation into 30° and 60° radiating plane wavese [24]. (b) Fabricated Huygens metasurface antenna with simulated and measured radiation patterns [25].

1.4 Metagratings

While Huygens metasurfaces effectively address the challenge of inefficient beam deflection at large angles, their typical implementation often necessitates two layers of complex structures to independently control the electric and magnetic fields of electromagnetic waves. However, these two layers are frequently subject to coupling, compelling the introduction of a third layer in the middle of the structure to mitigate mutual coupling issues. This additional layer presents a significant hurdle in practical fabrication and application.

In 2017, Alu's group proposed a novel design concept termed metagratings for wavefront manipulation [26]. Metagratings comprise sparse arrangements of subwavelength polarizable particles, diverging from the densely packed meta-atoms characteristic of traditional metasurfaces such as phase gradient and Huygens' metasurfaces. This innovative approach amalgamates meta-atoms with the principles of diffraction gratings to achieve anomalous reflection by suppressing undesired diffraction modes while preserving the desired ones, as illustrated in Figure 1.5(a). As depicted in Figure 1.5(b), by attenuating the 0^{th} diffraction mode,

all incident energy can be directed towards the -1st diffraction mode. If the diffraction angle of the -1st diffraction mode aligns with the incident angle, retroreflection can be realized. For instance, when the incident wave impinges at a 30° angle, as shown in Figure 1.5(c), the reflected wave will be entirely retroreflected along the original angle.

Unlike conventional metasurfaces such as phase gradient and Huygens metasurfaces, metagratings exhibit sparsely arranged meta-atoms. This sparse arrangement offers practical advantages, rendering metagratings straightforward to fabricate and deploy in real-world scenarios. The simplicity of the structure, combined with its efficient wavefront manipulation capabilities, positions metagratings as a promising and viable solution for achieving controlled beam deflections and other wavefront control applications.

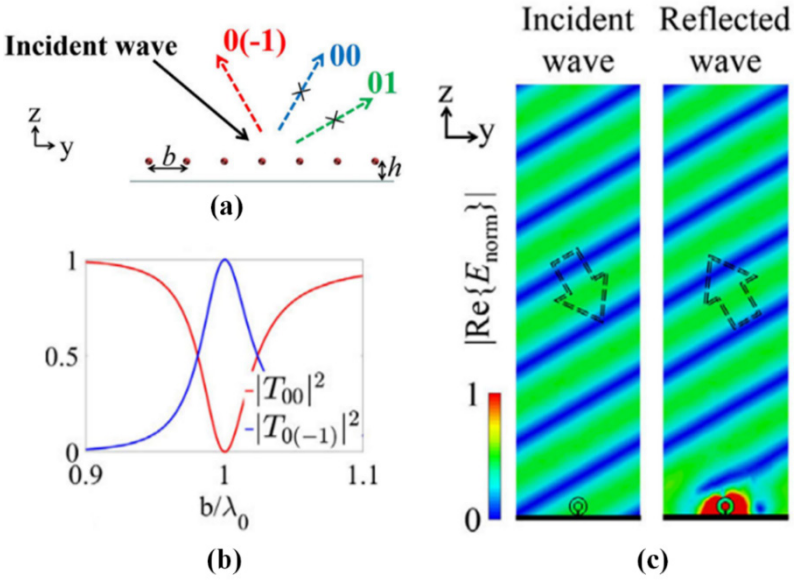

Figure 1.5: (a) Metagratings design concept: achieving anomalous reflection by suppressing undesired diffraction modes. (b) Suppression of the 0th mode enables full coupling of incident wave energy to the -1st mode. (c) Retroreflection under oblique incidence [26].

1.4.1 Single-atom metagratings

The introduction of the concept of metagratings garnered swift attention from scholars. In the same year, Epstein's group delved into a realistic fabrication perspective by analyzing and designing metagratings [27]. Illustrated in Figure 1.6(a), their work focused on controlling the period length of metagratings to facilitate the propagation of only three diffraction modes (-1st, 0th, and 1st order) in free space, thereby enabling perfect equal-power beam splitting by completely suppressing the 0th diffraction mode. As depicted in Figure 1.6(b), the utilization of strip capacitor structures as meta-atoms introduced a practical and feasible dimension to the implementation of metagratings, enhancing their applicability in real-world fabrication

scenarios. The electric field maps of equal power beam splitting with different outgoing angles are presented in Figure 1.6(c), where the field distribution exhibits remarkable symmetry, indicating effective suppression of specular reflection and nearly identical power distribution among the two split beams.

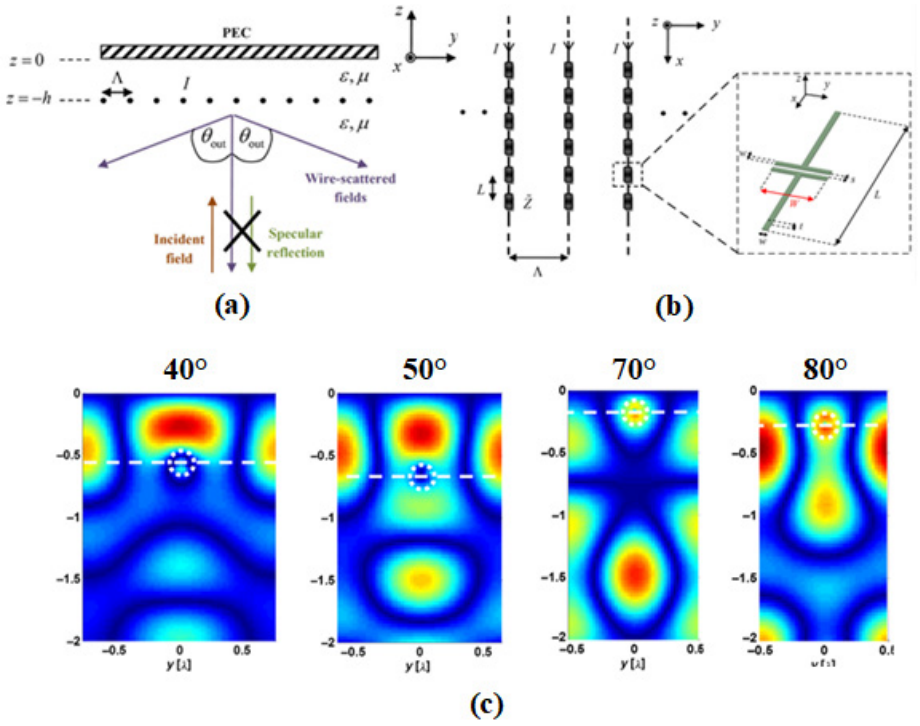

Figure 1.6: (a) Perfect equal-power beam splitting achieved by complete suppression of the 0th diffraction mode. (b) Utilizing a strip capacitor structure to design meta-atoms. (c) Electric field distribution for equal-power beam splitting at different outgoing angles [27].

Epstein *et al*. extended their investigation by exploring the design of anomalous reflection under oblique incidence using the single-atom metagratings structure [28,29], as illustrated in Figure 1.7(a). The fabricated prototype in Figure 1.7(b) featured a metagrating composed of sparsely arranged simple strip capacitors, highlighting its ease of PCB fabrication and practical application. To measure the prototype, the experimental setup was assembled in an anechoic chamber comprising transmitter and receiver standard horn antennas, along with a rotatable arm. While the transmitter antenna and the metagrating prototype remained fixed, the receiver antenna rotated and recorded the scattered power at each angle. The measurement results, depicted in Figure 1.7(c), exhibited remarkable characteristics—regardless of the magnitude of the anomalous reflection, the efficiency consistently approached close to 100%. This underscored the metagratings' ultra-high efficiency for large-angle beam deflection. Moreover, the design was grounded in rigorous analytical models, obviating the need for time-consuming full-wave simulations and optimizations. This simplicity, coupled with the metagrating's

exceptional efficiency, further solidified their appeal for real-world implementation in scenarios requiring large-angle beam deflection.

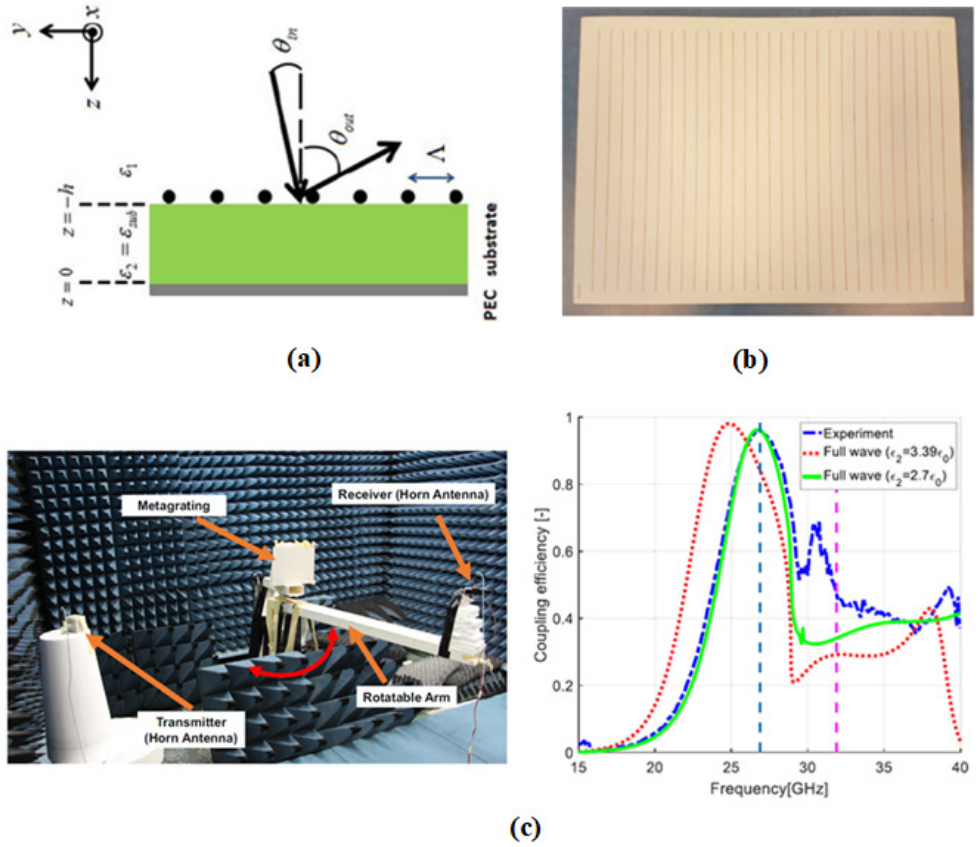

Figure 1.7: (a) Anomalous reflection achieved through metagratings. (b) Fabricated metagrating prototypes. (b) Fabricated metagrating prototypes. (b) Experimental setup utilized for measuring the performance of the metagrating, with efficiency for large-angle beam deflection approaching 100% [28,29].

1.4.2 Multi-atoms metagratings

For single-atom-based metagratings, their capability in beam manipulation is constrained due to their limitation in suppressing only one diffraction mode. Specifically, they exhibit anomalous reflections under oblique incidence and beam splitting with equal power. To broaden the spectrum of functionalities and manipulate more diffraction orders, the integration of additional meta-atoms becomes imperative. In response to this constraint, Popov et al. introduced the concept of multi-atom-based metagratings, as illustrated in Figure 1.8(a) [30]. In this configuration, each period comprises *N* meta-atoms to govern *N* propagating diffraction modes. Consequently, multi-atom metagratings extend control over a greater number of diffraction modes compared to their single-atom counterparts, facilitating the realization of more intricate beam manipulations, including anomalous reflection and asymmetric beam splitting at normal incidence.

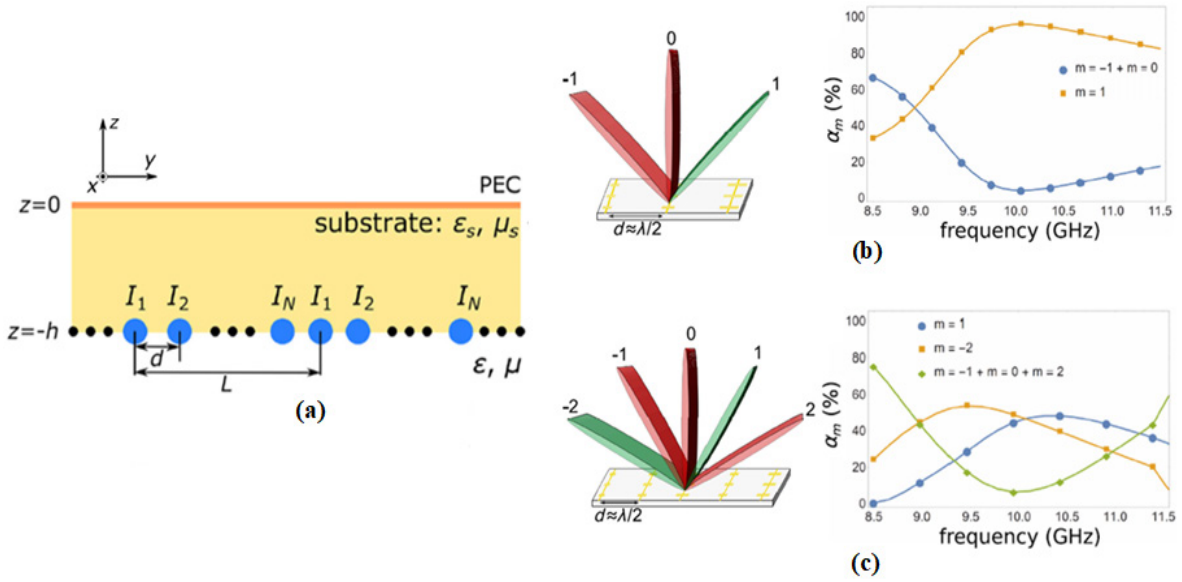

Figure 1.8: (a) Side view of multi-atoms metagratings. (b) Scheme and simulation results demonstrating anomalous reflection and asymmetric beam splitting at normal incidence based on multi-atom metagratings [30].

Figure 1.8(b) demonstrates two devised beam manipulation schemes for normal incidence. Both designs are tailored to suppress the -1st and 0th modes, achieving anomalous reflection by exclusively propagating the 1st mode in one case, while in the other case, the suppression extends to -1st, 0th, and 2nd modes, with the -2nd and 1st modes propagating to effectuate beam splitting. Simulation results indicate exceedingly high efficiency in beam manipulation, surpassing 90% in both scenarios.

Subsequently, to bolster the efficiency of diffraction mode control, a design methodology was introduced, involving the incorporation of 2*N* meta-atoms per period [31]. This approach enhances beam manipulation efficiency by doubling the number of meta-atoms in comparison to the diffraction modes. However, it results in a denser arrangement of metagratings. To strike a balance between efficiency and sparse arrangement, advanced optimization algorithms can be employed to ascertain the optimal impedance density required for meta-atoms [32,33]. This optimization strategy contributes to achieving both efficient beam manipulation and a practically sparse metagrating structure.

Reflective metagratings, due to the presence of a ground plane, inherently limit the diffraction pattern on the opposite side of the metagratings. To surmount this limitation, in 2020, Bilotti *et al*. introduced the concept of transmissive metagratings [34], as depicted in Figure 1.9(a). Unlike reflective metagratings, the diffraction modes in transmissive metagratings are symmetrical both upwards and downwards. Consequently, the number of controllable

diffraction modes is doubled for transmissive metagratings compared to reflective metagratings with the same period length. In this context, lumped capacitors with varying capacitance are employed to realize meta-atoms with desired load impedance. By appropriately setting the capacitance value of the capacitor, both reflection and transmission diffraction modes can be simultaneously controlled, enabling various beam manipulations such as anomalous refraction and transmissive beam splitting as shown in Figure 1.9(b). Simulation results indicate a high efficiency of up to 96% for anomalous refraction and a power ratio in line with expectations for beam splitting. Transmissive metagratings pave the way for novel possibilities in beam manipulation.

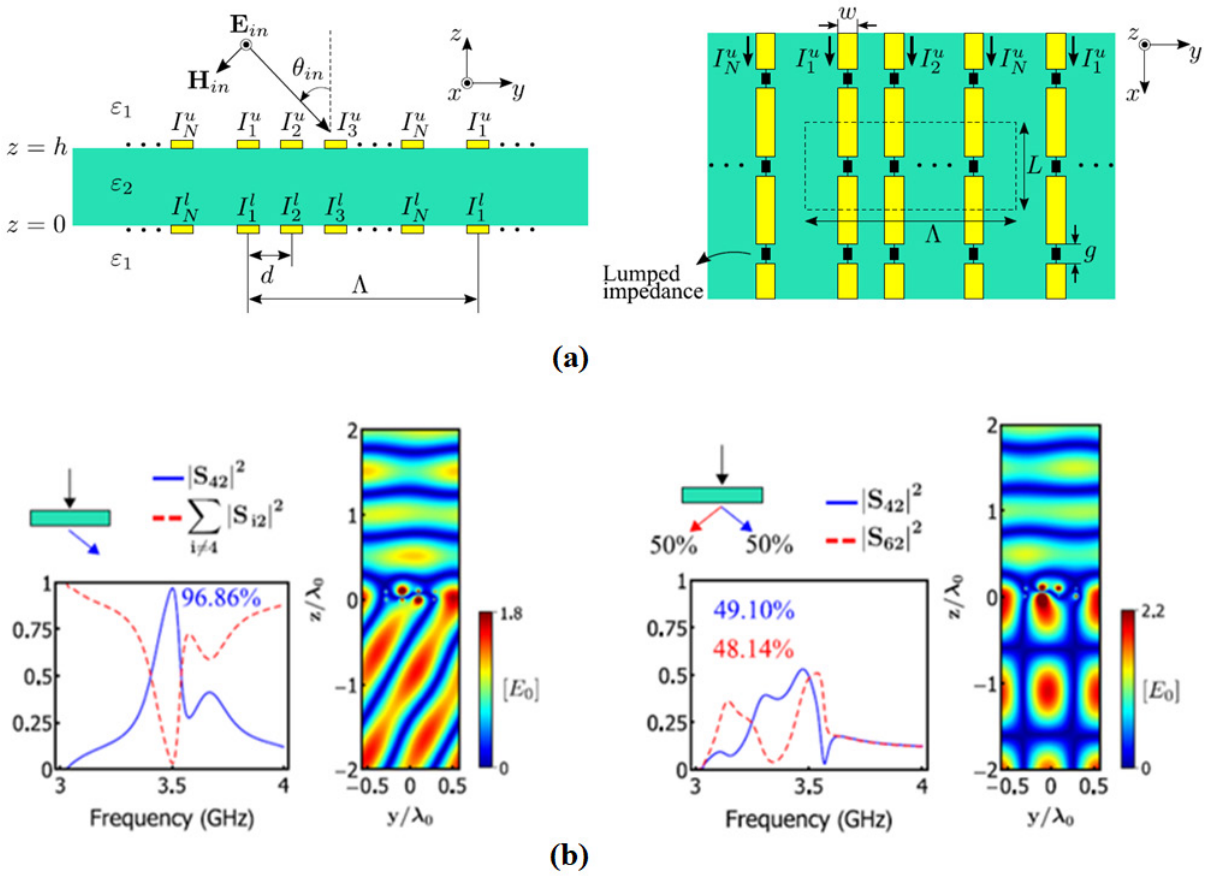

Figure 1.9: (a) Side and top views of transmissive metagratings, utilizing lumped capacitors to form the meta-atom. (b) Design scheme and simulation results illustrating anomalous refraction and transmissive beam splitting based on transmissive metagratings [34].

Epstein *et al*. further advanced the capabilities of transmissive metagratings by proposing the design of multilayer metagratings for more intricate beam manipulation, including focusing functions, as illustrated in Figure 1.10 (a) [35]. In this manner, not only can the amplitude of diffraction modes be controlled, but their phase can also be flexibly manipulated. The simulated

electric field distribution of focusing demonstrates clear focus presentation, breaking the traditional diffraction limit and providing a promising avenue for future holographic technology. The design of multilayer multi-atom metagratings typically involves a complex optimization process. To streamline this process and reduce complexity when utilizing optimization algorithms, Gengyu Xu *et al*. introduced an equivalent circuit model for multilayer multi-atom metagratings [36]. Each diffraction mode is equated to a circuit port, and each layer of the dielectric medium is equated to transmission. Since the circuit's response can be rapidly obtained in simulation, this method accelerates the metagrating design process. To validate the effectiveness of this equivalent circuit model, a metagrating retroreflector was designed based on this methodology, as depicted in Figure 1.10 (b). Near-field simulation results demonstrate that for a transmissive metagrating, under obliquely incident waves, it can reflect back almost completely along the original incident angle.

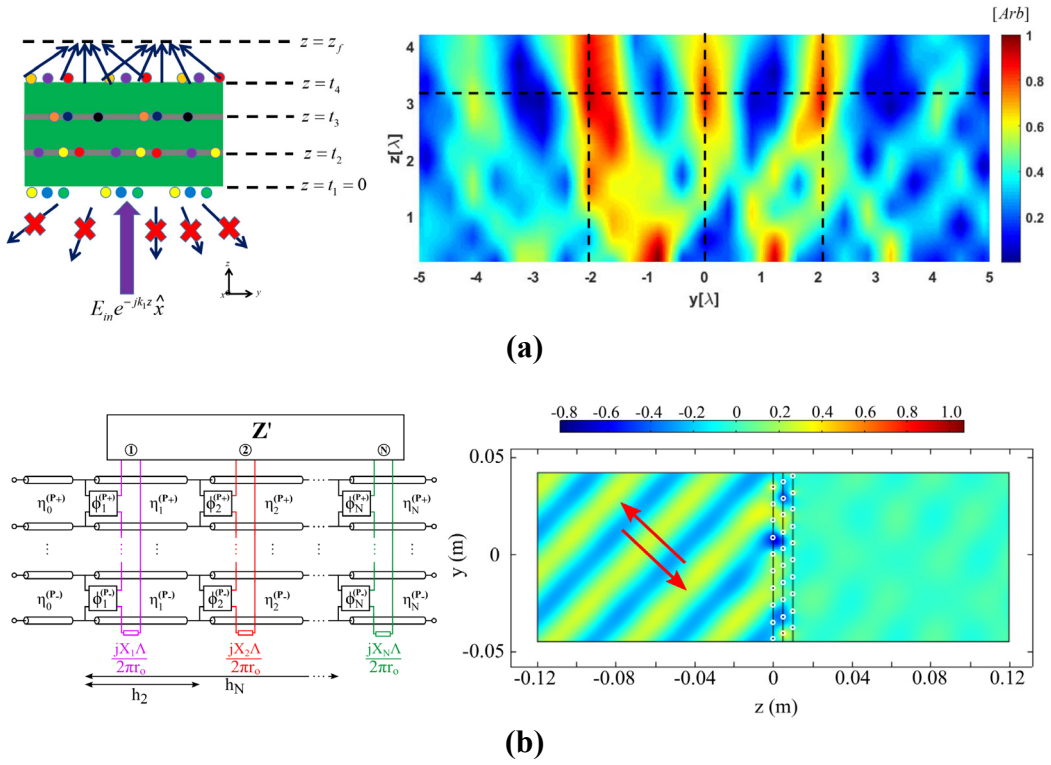

Figure 1.10: (a) Side view of multilayer metagratings and simulated electric field distribution demonstrating the designed beam focusing [35]. (b) Equivalent circuit model of the multilayer metagratings and simulated electric field distribution illustrating the designed retroreflectio [36].

Beyond the aforementioned designed functions, metagratings offer a versatile platform for various electromagnetic wave manipulations, including nonradiative near-field pattern manipulation [37,38]. Ongoing exploration of metagratings' potential applications underscores their adaptability and effectiveness in controlling and manipulating electromagnetic waves

across different scenarios.

It is worth noting that several multi-space harmonic metasurface designs utilizing the "phase-shift" approach have also been proposed to achieve efficient wavefront manipulation [39–41]. However, many of these designs rely on densely arranged meta-atoms or full-wave optimizations, lacking intuitive design guidance. Hence, metagratings featuring sparsely arranged meta-atoms designed using explicit analytical design guidance offer an excellent alternative for efficient wavefront manipulation.

1.5 Sparse metasurfaces

In metagratings, the conventional excitation source predominantly involves a plane wave, a requirement that may pose practical challenges in various applications. To surmount this constraint, the innovative concept of sparse metasurface design, grounded in the metagrating analysis method, has been introduced [42], as depicted in Figure 1.11(a). The design framework of sparse metasurfaces leverages a line-current-based analysis similar to that of metagratings. However, it diverges in that the incident wave field is extracted via sophisticated simulation software, thereby liberating the design from the confinement to plane waves. Furthermore, the extraction of self-impedance and mutual impedance associated with the radiation field of the line current is facilitated by simulation software, enhancing adaptability to non-planar geometries such as curved conformal structures. A prototype of the fabricated sparse metagrating is illustrated in Figure 1.11(a), featuring a PCB-printed dipole antenna at its base, connected to a waveguide port serving as the excitation source. The upper portion of the metagrating comprises a semi-cylindrical sparse metasurface, tailored for efficient directional beam radiation. Beyond beam steering capabilities, sparse metasurfaces hold promise for radar cross-section (RCS) reduction. In literature [43], a sparse metasurface design adept at conforming to cylindrical or ellipsoidal objects is proposed to achieve highly effective wave absorption.

In the pursuit of augmenting the tunability and reconfigurability of sparse metasurfaces, researchers have realized reconfigurable sparse metasurfaces by integrating varactor diodes as meta-atoms [44]. As delineated in Figure 1.11(b), the dynamic modulation of the radiation beam is achieved through the modulation of external bias voltage applied to the varactor diodes. This technological advancement not only enhances the adaptability of sparse metasurfaces but also aligns with the burgeoning interest in reconfigurable intelligent surfaces, a focal point in recent advancements in wireless communications. The capacity to dynamically manipulate and

regulate electromagnetic wave interactions with these surfaces holds significant promise for a plethora of applications in future communication technologies.

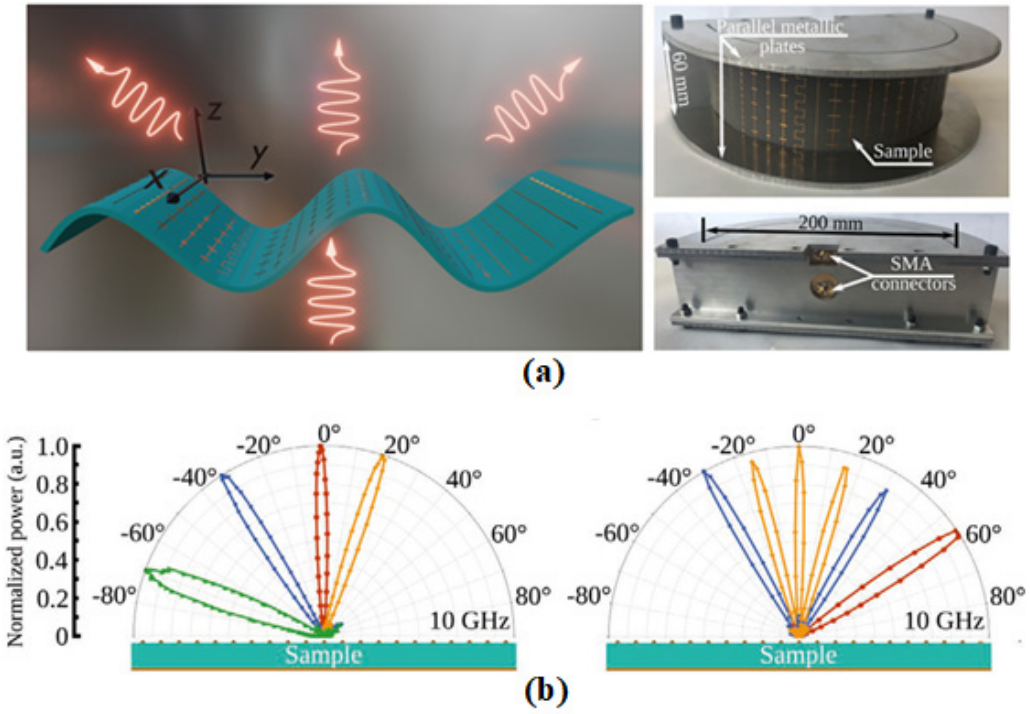

Figure 1.11: (a) Sparse metasurface manipulating non-plane wave wavefront with conformal structure, along with the fabricated prototype [42]. (b) Dynamic beam manipulation: beam steering and manipulation of the number of beams [44].

1.6 Conclusion

This chapter presents a historical overview of the evolution of metamaterials, tracing its origins to Veselago's groundbreaking work on negative refractive index materials in 1968 and culminating in the experimental validation of metamaterials in the early 2000s. The advent of metasurfaces, catalyzed by Capasso's introduction of the generalized Snell's law in 2011, represented a pivotal advancement in wave manipulation, enabling precise control over electromagnetic wavefronts.

Owing to conventional metasurfaces often encounter challenges related to low efficiency in achieving large-angle beam deflections and tightly packed structures. To mitigate these limitations, the concept of metagratings is introduced, with subsequent sections offering a thorough exploration of metagratings development. To date, researchers have devised a diverse array of wavefront manipulation techniques leveraging metagratings, including anomalous reflection, anomalous refraction, beam splitting, retroreflection, and focusing.

These metagrating-based designs have exhibited nearly flawless beam manipulation

efficiency despite featuring sparse and straightforward structures. This underscores the contemporary significance of metagratings as an advanced design paradigm for wavefront manipulation, positioning them as compelling candidates for shaping the future landscape of wavefront manipulation methodologies.

Chapter 2
Electromagnetic characterization and analysis of metagratings

Contents

2.1 Introduction

In Chapter 1, a thorough investigation into metamaterials and metasurfaces is undertaken, with a primary focus on the analysis and design of metagratings tailored for efficient wavefront manipulation. The chapter sets out to delve into the electromagnetic characteristics of metagratings, elucidating the underlying principles fundamental to wavefront manipulation. This encompasses the derivation of reflection and transmission coefficients within multilayer media, an analysis of radiation characteristics, and considerations for optimal wavefront manipulation design.

The initial segment of analysis centers on the reflection and transmission phenomena within a generalized three-layer dielectric substrate. Subsequently, the discussion is structured around specific reflective and transmissive metagrating models. Vital methodologies pertinent to metagrating design are expounded upon, including the derivation of expressions for the radiated field of periodic arrays of line currents, strategies for designing wire load impedance in metagratings to achieve desired wavefront manipulation outcomes, and the selection of metagrating period lengths vis-à-vis the angle of coverage of the diffraction pattern.

This chapter aims to provide a comprehensive exploration of the electromagnetic characteristics and analytical considerations pivotal to metagrating design and analysis. By establishing this foundational understanding, subsequent chapters will delve into detailed device design and implementation, building upon the principles elucidated herein.

2.2 Reflection and transmission analysis

As shown in Figure 2.1, a three-layer medium is considered to analyze the reflection and transmission of an obliquely incident electromagnetic wave. It is specified that medium 1 and medium 3 extend infinitely along the negative and positive directions of the z-axis, respectively. The thickness of medium 2 is denoted as h. The permittivity and permeability of these media are represented by ε_i and μ_i, respectively, where i takes values of 1, 2, or 3. Additionally, the wavenumber and wave impedance of the media are $k_i = \omega\sqrt{\mu_i\varepsilon_i}$ and $\eta_i = \mu_i/\varepsilon_i$. Given that the media under consideration are nonmagnetic, it is stipulated that $\mu_i = \mu_0$ (where μ_0 is the permeability of free space) for all i = 1, 2, or 3.

The incident wave, characterized by an amplitude E_{in}, is obliquely incident from medium 1 into medium 2 at an angle of incidence θ_1. As the wave traverses the interfaces between these

media, it follows a specific propagation path as depicted in Figure 2.1.

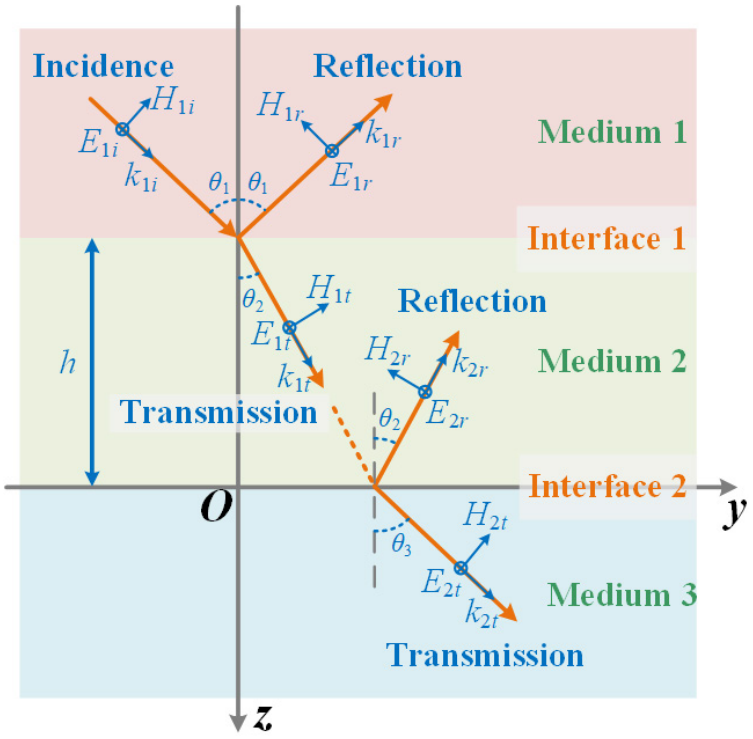

Figure 2.1: Schematic diagram illustrating the reflection and transmission of a plane wave polarized along the *x*-axis and incident obliquely on various media.

In order to comprehensively understand the total field of electromagnetic waves within each medium, a step-by-step analysis is required. This entails individually examining the reflection and transmission of the waves as they encounter and pass through interfaces 1 and 2. By systematically analyzing the behavior of the waves at each interface, one can gain insights into how the incident wave is affected, and how the reflected and transmitted waves contribute to the overall electromagnetic field within each medium. This analytical approach is essential for characterizing the complete interaction of electromagnetic waves with the different materials involved in the configuration.

Firstly, the incident wave in medium 1 can be expressed as

$$\vec{E}_{1i} = \vec{e}_x E_{\text{in}} e^{-jk_1[y\sin\theta_1 + (z+h)\cos\theta_1]} \tag{2.1}$$

The corresponding magnetic field can be obtained from Maxwell-Faraday equation as

$$\begin{aligned}\vec{H}_{1i} &= \frac{1}{\eta_1}\left(\vec{e}_y \sin\theta_1 + \vec{e}_z \cos\theta_1\right) \times \vec{E}_{1i} \\ &= \left(\vec{e}_y \cos\theta_1 - \vec{e}_z \sin\theta_1\right)\frac{E_{\text{in}}}{\eta_1} e^{-jk_1[y\sin\theta_1 + (z+h)\cos\theta_1]}\end{aligned} \tag{2.2}$$

The electric field of the reflected wave in medium 1 is written as

$$\vec{E}_{1r} = \vec{e}_x E_{\text{in}} r_1 e^{-jk_1[y\sin\theta_1 - (z+h)\cos\theta_1]} \tag{2.3}$$

where $r_1 = E_{1r}/E_{1i}$ is the ratio of the amplitude of E_{1r} to E_{1i}. The magnetic field of the reflected wave according to Maxwell-Faraday equation is

$$\vec{H}_{1r} = \frac{1}{\eta_1}\left(\vec{e}_y \sin\theta_1 - \vec{e}_z \cos\theta_1\right) \times \vec{E}_{1r}$$
$$= -\left(\vec{e}_y \cos\theta_1 + \vec{e}_z \sin\theta_1\right) \frac{r_1 E_{\text{in}}}{\eta_1} e^{-jk_1[y\sin\theta_1 - (z+h)\cos\theta_1]} \tag{2.4}$$

Next, let us consider the total field in the medium 1. The total electric field, denoted as $\vec{E}_1 = \vec{E}_{1i} + \vec{E}_{1r}$, is obtained by combining the incident and reflected waves. Utilizing Eqs. (2.1) and (2.3), it can be expressed as

$$\vec{E}_1 = \vec{e}_x E_{\text{in}}\left[e^{-jk_1(z+h)\cos\theta_1} + r_1 e^{jk_1(z+h)\cos\theta_1}\right] e^{-jk_1 y \sin\theta_1} \tag{2.5}$$

The total magnetic field is $\vec{H}_1 = \vec{H}_{1i} + \vec{H}_{1r}$ and is written according to Eqs. (2.2) and (2.4) as

$$\vec{H}_1 = \vec{e}_y \frac{E_{\text{in}}}{\eta_1}\cos\theta_1 \left[e^{-jk_1(z+h)\cos\theta_1} - r_1 e^{jk_1(z+h)\cos\theta_1}\right] e^{-jk_1 y \sin\theta_1} -$$
$$\vec{e}_z \frac{E_{\text{in}}}{\eta_1}\sin\theta_1 \left[e^{-jk_1(z+h)\cos\theta_1} + r_1 e^{jk_1(z+h)\cos\theta_1}\right] e^{-jk_1 y \sin\theta_1} \tag{2.6}$$

Then, considering the transmitted wave in medium 2 originating from medium 1, the electric and magnetic fields of this transmitted wave can be expressed as

$$\vec{E}_{1t} = \vec{e}_x t_1 E_{\text{in}} e^{-jk_2(y\sin\theta_2 + z\cos\theta_2)} \tag{2.7}$$

$$\vec{H}_{1t} = \frac{1}{\eta_2}\left(\vec{e}_y \sin\theta_2 + \vec{e}_z \cos\theta_2\right) \times \vec{E}_{1t}$$
$$= \left(\vec{e}_y \cos\theta_2 - \vec{e}_z \sin\theta_2\right) \frac{t_1 E_{\text{in}}}{\eta_2} e^{-jk_2(y\sin\theta_2 + z\cos\theta_2)} \tag{2.8}$$

where $t_1 = E_{1t}/E_{1i}$ is the ratio of the amplitude of E_{1t} to E_{1i}.

The transmitted wave in medium 2 from medium 1 will propagate towards medium 3 as an incident wave in medium 2. The resulting reflected wave in medium 2 can be characterized by its electric and magnetic fields, which are expressed as

$$\vec{E}_{2r} = \vec{e}_x t_1 r_2 E_{\text{in}} e^{-jk_2(y\sin\theta_2 - z\cos\theta_2)} \tag{2.9}$$

$$\vec{H}_{2r} = \frac{1}{\eta_2}\left(\vec{e}_y \sin\theta_2 - \vec{e}_z \cos\theta_2\right) \times \vec{E}_{2r}$$
$$= -\left(\vec{e}_y \cos\theta_2 + \vec{e}_z \sin\theta_2\right) \frac{t_1 r_2 E_{\text{in}}}{\eta_2} e^{-jk_2(y\sin\theta_2 - z\cos\theta_2)} \tag{2.10}$$

By utilizing Eqs. (2.7) and (2.9), the total electric field $\vec{E}_2 = \vec{E}_{1t} + \vec{E}_{2r}$ in medium 2 can be expressed as

$$\vec{E}_2 = \vec{e}_x t_1 E_{\text{in}} (e^{-jk_2 z\cos\theta_2} + r_2 e^{jk_2 z\cos\theta_2}) e^{-jk_2 y \sin\theta_2} \tag{2.11}$$

where $r_2 = E_{2r}/E_{1t}$ is the ratio of the amplitude of E_{2r} to E_{1t}. Similarly, by employing Eqs. (2.8) and (2.10), the total magnetic field $\vec{H}_2 = \vec{H}_{1t} + \vec{H}_{2r}$ in medium 2 can be expressed as

$$\vec{H}_2 = \vec{e}_y \frac{t_1 E_{\text{in}}}{\eta_2} \cos\theta_2 \left(e^{-jk_2 z\cos\theta_2} - r_2 e^{jk_2 z\cos\theta_2}\right) e^{-jk_2 y\sin\theta_2} - \vec{e}_z \frac{t_1 E_{\text{in}}}{\eta_2} \sin\theta_2 \left(e^{-jk_2 z\cos\theta_2} + r_2 e^{jk_2 z\cos\theta_2}\right) e^{-jk_2 y\sin\theta_2} \quad (2.12)$$

Now, let us consider the transmitted wave in medium 3 originating from medium 2. The associated electric and magnetic fields are expressed as

$$\vec{E}_{2t} = \vec{e}_x t_1 t_2 E_{\text{in}} e^{-jk_3(y\sin\theta_3 + z\cos\theta_3)} \quad (2.13)$$

$$\vec{H}_{2t} = \frac{1}{\eta_3}(\vec{e}_x \sin\theta_3 + \vec{e}_z \cos\theta_3) \times \vec{E}_{2t} = (\vec{e}_y \cos\theta_3 - \vec{e}_z \sin\theta_3) \frac{t_1 t_2 E_{\text{in}}}{\eta_3} e^{-jk_3(y\sin\theta_3 + z\cos\theta_3)} \quad (2.14)$$

where $t_2 = E_{2t}/E_{1t}$ is the ratio of the amplitude of E_{2t} to E_{1t}. Then the total electric field $\vec{E}_3 = \vec{E}_{2t}$ and total magnetic field $\vec{H}_3 = \vec{H}_{2t}$ in medium 3 are given by

$$\vec{E}_3 = \vec{e}_x t_1 t_2 E_{\text{in}} e^{-jk_3(y\sin\theta_3 + z\cos\theta_3)} \quad (2.15)$$

$$\vec{H}_3 = (\vec{e}_y \cos\theta_3 - \vec{e}_z \sin\theta_3) \frac{t_1 t_2 E_{\text{in}}}{\eta_3} e^{-jk_3(y\sin\theta_3 + z\cos\theta_3)} \quad (2.16)$$

2.2.1 Reflection and transmission coefficients

In the previous analysis, expressions for the total electric and magnetic fields in medium *i* (where *i* = 1, 2, 3) is derived. However, the reflection and transmission coefficients (r_1, r_2, t_1, and t_2) included in the expressions were not clarified. In the following, I will further derive expressions for these coefficients using the continuity property of the tangential directions of the electric and magnetic fields at the interfaces of the different media.

First, at the interface 2 (*i.e.*, $z = 0$), the continuity of the tangential electric field components leads to the following relation

$$(1 + r_2) e^{-jk_2 y\sin\theta_2} = t_2 e^{-jk_3 y\sin\theta_3} \quad (2.17)$$

$$\cos\theta_2 \frac{1}{\eta_2}(1 - r_2) e^{-jk_2 y\sin\theta_2} = \cos\theta_3 \frac{1}{\eta_3} t_2 e^{-jk_3 y\sin\theta_3} \quad (2.18)$$

Combining Snell's law $k_2 y\sin\theta_2 = k_3 y\sin\theta_3$ with the above Eqs. (2.17) and (2.18), the coefficients can be solved as

$$r_2 = \frac{\eta_3\cos\theta_2 - \eta_2\cos\theta_3}{\eta_3\cos\theta_2 + \eta_2\cos\theta_3} \quad (2.19)$$

$$t_2 = \frac{2\eta_3\cos\theta_2}{\eta_2\cos\theta_3 + \eta_3\cos\theta_2} \quad (2.20)$$

Then, at the interface 1 (*i.e.*, $z = -h$), the continuity of the tangential electric field components results in

$$(1 + r_1) e^{-jk_1 y\sin\theta_1} = t_1 (e^{jk_2 h\cos\theta_2} + r_2 e^{-jk_2 h\cos\theta_2}) e^{-jk_2 y\sin\theta_2} \quad (2.21)$$

$$\frac{1}{\eta_1}\cos\theta_1\,(1-r_1)e^{-jk_1 y\sin\theta_1}=\frac{t_1}{\eta_2}\cos\theta_2\,(e^{jk_2 h\cos\theta_2}-r_2 e^{-jk_2 h\cos\theta_2})e^{-jk_2 y\sin\theta_2} \quad (2.22)$$

Combining Snell's law $k_1 y\sin\theta_1=k_2 y\sin\theta_2$ with the above Eqs. (2.21) and (2.22), the coefficients can be solved as

$$r_1=\frac{(\eta_2/\cos\theta_2-\eta_1/\cos\theta_1)e^{jk_2 h\cos\theta_2}+(\eta_2/\cos\theta_2+\eta_1/\cos\theta_1)r_2 e^{-jk_2 h\cos\theta_2}}{(\eta_2/\cos\theta_2+\eta_1/\cos\theta_1)e^{jk_2 h\cos\theta_2}+(\eta_2/\cos\theta_2-\eta_1/\cos\theta_1)r_2 e^{-jk_2 h\cos\theta_2}} \quad (2.23)$$

To simplify the expression, let us define $\eta'_i=\eta_i/\cos\theta_i$ for i = 1, 2, 3. Substituting r_2 from Eq. (2.19) into Eq. (2.23), it can be simplified as

$$r_1=\frac{\eta'_2(\eta'_3-\eta'_1)+j(\eta'_2\eta'_2-\eta'_3\eta'_1)\tan(k_2 h\cos\theta_2)}{\eta'_2(\eta'_3+\eta'_1)+j(\eta'_2\eta'_2+\eta'_3\eta'_1)\tan(k_2 h\cos\theta_2)} \quad (2.24)$$

Similarly, the transmission coefficient t_1 can be solved as

$$t_1=\frac{\eta'_2(\eta'_3+\eta'_2)}{\eta'_2(\eta'_3+\eta'_1)\cos(k_2 h\cos\theta_2)+j(\eta'_2\eta'_2+\eta'_3\eta'_1)\sin(k_2 h\cos\theta_2)} \quad (2.25)$$

Up to this point, all reflection and transmission coefficients have been derived. They will be analyzed specifically in the following sections according to the two cases of reflective and transmissive metagratings.

2.2.2 Fresnel reflection coefficient in the reflective metagratings

If the propagation system depicted in Figure 2.1 represents a reflective metagrating, the constituent media are designated as follows: medium 1 corresponds to air, medium 2 corresponds to the dielectric substrate, and medium 3 corresponds to metal, where $\eta_3=0$. The coefficients denoted as r_1, t_1, r_2, and t_2 in Eqs. (2.19), (2.20), (2.24) and (2.25) can be reformulated as follows

$$r_1=\frac{-\rho+j\tan(\beta_2 h)}{\rho+j\tan(\beta_2 h)} \quad (2.26)$$

$$t_1=\frac{1}{\rho\cos(\beta_2 h)+j\sin(\beta_2 h)} \quad (2.27)$$

$$r_2=-1 \quad (2.28)$$

$$t_2=0 \quad (2.29)$$

where $\beta_2=k_2\cos\theta_2$ represents the longitudinal wave number in medium 2, and ρ is the wave impedance ratio defined as

$$\rho=\eta'_1/\eta'_2=\frac{\eta_1\cos\theta_2}{\eta_2\cos\theta_1}=\frac{\sqrt{\mu_0/\varepsilon_1}\cos\theta_2}{\sqrt{\mu_0/\varepsilon_2}\cos\theta_1}=\frac{\omega\sqrt{\mu_0\varepsilon_2}\cos\theta_2}{\omega\sqrt{\mu_0\varepsilon_1}\cos\theta_1}=\frac{k_2\cos\theta_2}{k_1\cos\theta_1}=\beta_2/\beta_1 \quad (2.30)$$

Consequently, for reflective metagratings, the Fresnel reflection coefficient is expressed as

$$\Gamma=r_1=\frac{-\rho+j\tan(\beta_2 h)}{\rho+j\tan(\beta_2 h)} \quad (2.31)$$

2.2.3 Fresnel reflection and transmission coefficients in transmissive metagratings

If the propagation system illustrated in Figure 2.1 is indicative of a transmissive metagrating, it follows that both media 1 and 3 represent air, while medium 2 denotes the dielectric substrate. Consequently, it holds that $\eta_1 = \eta_3$ and $\theta_1 = \theta_3$. The coefficients denoted as r_1, t_1, r_2 and t_2 in Eqs. (2.19), (2.20), (2.24) and (2.25) are rewritten as follows

$$r_1 = \frac{j(1-\rho^2)\tan(\beta_2 h)}{2\rho+j(1+\rho^2)\tan(\beta_2 h)} \tag{2.32}$$

$$t_1 = \frac{1+\rho}{2\rho\cos(\beta_2 h)+j(1+\rho^2)\sin(\beta_2 h)} \tag{2.33}$$

$$r_2 = \frac{\rho-1}{\rho+1} \tag{2.34}$$

$$t_2 = \frac{2\rho}{\rho+1} \tag{2.35}$$

Thus, in the context of transmissive metagratings, the Fresnel reflection and transmission coefficients are expressed as

$$\Gamma = r_1 = \frac{j(1-\rho^2)\tan(\beta_2 h)}{2\rho+j(1+\rho^2)\tan(\beta_2 h)} \tag{2.36}$$

$$T = t_1 t_2 = \frac{2\rho}{2\rho\cos(\beta_2 h)+j(1+\rho^2)\sin(\beta_2 h)} \tag{2.37}$$

2.3 Radiation characteristics of polarization current arrays

2.3.1 Radiation field of uniform periodic metal wire array

Metagratings achieve precise wavefront manipulation by orchestrating incident waves and diffraction waves. The latter emerge from the secondary radiation of polarization currents induced by incident waves in metagrating polarizable elements. Therefore, I delve into the examination of radiated fields originating from single line currents, extending this investigation to characterize the spatial distribution of radiated fields for arrays of periodic uniform and non-uniform line currents.

As illustrated in Figure 2.2, the metal wire array comprises conductor rods of radius r arranged along the y-axis with period Λ_y, extending infinitely in both the x- and y-directions. The condition $r \ll \Lambda_y$ and $rk_0 \ll 1$ holds, where k_0 denotes the wavenumber in air. When a plane wave polarized along the x-axis with amplitude E_{in} is incident obliquely at an angle θ_1 to the array of wires, each wire is stimulated to generate a polarization current. The line current on the the n^{th} wire can be represented as [45]

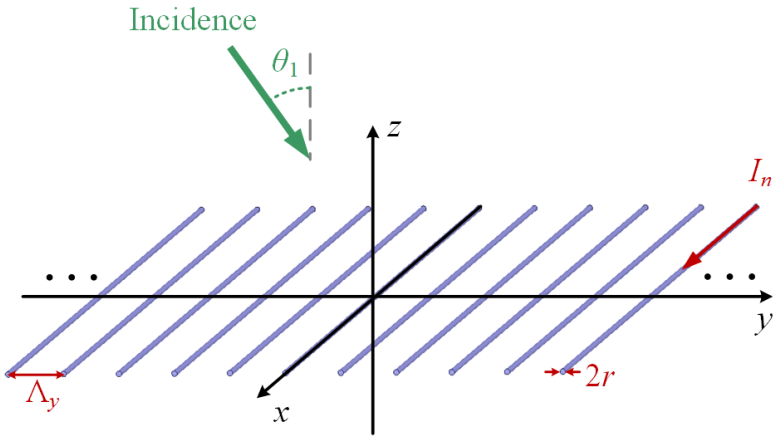

Figure 2.2: Plane wave incident obliquely at angle θ_1 on an infinite array of uniform metal wires.

$$I_n = I_0 e^{-jn\xi_0\Lambda_y} \tag{2.38}$$

where I_0 signifies the polarization current amplitude and $\xi_0 = k_0 \sin\theta_1$ is the transverse wavenumber. Subsequently, the radiation field arising from the line current in free-space can be expressed as [45]

$$E_n^{\text{rad}} = -\frac{\eta_0 k_0}{4} I_n H_0^{(2)}(kd_n) \tag{2.39}$$

where $\eta_0 = \mu_0/\varepsilon_0$ denotes the wave impedance of air, and $H_0^{(2)}(\cdot)$represents the second kind of Hankel function, with $d_n = \sqrt{z^2 + (y - n\Lambda_y)^2}$. Thus, the radiation field of the entire line current array, generated by the polarization currents on each wire, can be expressed as a summation over all the wires. The resultant electric field E^{rad} produced by the radiation field is then given by

$$E^{\text{rad}} = -\frac{\eta_0 k_0}{4} I_0 \sum_{n=-\infty}^{\infty} e^{-jn\xi_0\Lambda_y} H_0^{(2)}(k_0\sqrt{z^2 + (y - n\Lambda_y)^2}) \tag{2.40}$$

Due to the slow convergence of the second kind of Hankel function, Poisson summation and Fourier transforms can be employed to reshape its form and accelerate the convergence. Thus, a segment of Eq. (2.40) can be reformulated as [45]

$$\sum_{n=-\infty}^{\infty} e^{-jn\xi_0\Lambda_y} H_0^{(2)}(k_0\sqrt{z^2 + (y - n\Lambda_y)^2}) = j\frac{2}{\Lambda_y}\sum_{m=-\infty}^{\infty} \frac{e^{-j\xi_m y} e^{-\alpha_m|z|}}{\alpha_m} \tag{2.41}$$

where $\xi_m = \xi_0 + 2\pi m/\Lambda_y$ and $\alpha_m = \sqrt{\xi_m^2 - k_0^2}$. This transformation aids in enhancing the convergence of the Hankel function, thereby rendering the computation more efficient and numerically stable.

Eqs. (2.40) and (2.41) elucidate that the radiation field of the line current array can be represented as a superposition of an infinite number of Floquet modes. For the m^{th} order Floquet mode capable of propagating in space, its transverse wavenumber must satisfy $|\xi_m| \leq k_0$.

When $|\xi_m| > k_0$, the Floquet mode assumes the form of an evanescent wave, impeding propagation. It is noteworthy that for $z = 0$ in Eq. (2.41), the series fails to converge. This implies a singularity in the expression of the electric field at the center of the array of line currents. Consequently, the electric field on the surface of the cylinder wire is utilized to approximate the electric field expression. Thus, Eq. (2.41) necessitates rephrasing as [45]

$$\sum_{n=-\infty}^{\infty} e^{-jn\xi_0\Lambda_y} H_0^{(2)}\left(k_0\sqrt{z^2+\left(y-n\Lambda_y\right)^2}\right) = \begin{cases} j\frac{2}{\Lambda_y}\sum_{m=-\infty}^{\infty}\frac{e^{-j\xi_m y}e^{-\alpha_m|z|}}{\alpha_m}, & z \neq 0 \\ \frac{2}{\Lambda_y\beta_0}+j\frac{1}{\pi}\left[2\ln\left(\frac{\Lambda_y}{2\pi r}\right)+\sum_{\substack{m=-\infty \\ m\neq 0}}^{\infty}\left(\frac{2\pi}{\Lambda_y\alpha_m}-\frac{1}{|m|}\right)\right], & z = 0 \end{cases} \tag{2.42}$$

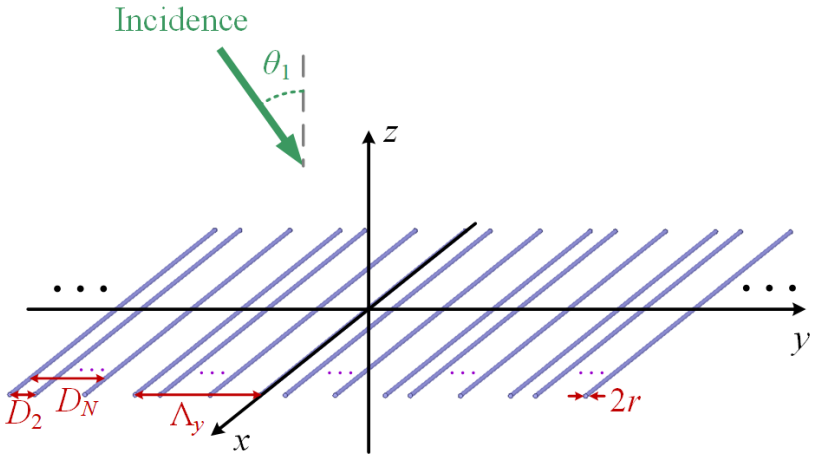

Figure 2.3: Plane wave incident obliquely at angle θ_1 into an infinite array of non-uniform metal wires.

2.3.2 Radiation field of non-uniform periodic metal wire array

In Section 2.3.1, the analysis of the radiation field of a uniform periodic metal wire array is conducted. Subsequently, I proceed to examine the radiation field of a non-uniform periodic metal wire array. Herein, I consider each period comprising N metal wires, whereby the distance of the p^{th} wire from the first wire is denoted as D_p (with $D_1 = 0$), as depicted in Figure 2.3. Subsequent to the methodology outlined in Section 2.3.1, the radiation field of the entire line current array is articulated as

$$E^{\text{rad}} = -\frac{\eta_0 k_0}{4}\sum_{p=1}^{N}\sum_{n=-\infty}^{\infty} I_p e^{-jn\xi_0\Lambda_y} H_0^{(2)}\left(k_0\sqrt{z^2+(y-n\Lambda_y+D_p)^2}\right) \tag{2.43}$$

where I_p denotes the line current on the p^{th} wire within one period. Analogously, the subsequent expansion of the Hankel function in Eq. (2.43) adheres to the principles delineated in Eqs. (2.41)-(2.42).

2.4 Analysis of metagratings

In Sections 2.2 and 2.3, an analysis of the reflection and transmission properties of the dielectric substrate under diverse boundary conditions, alongside the radiation characteristics of the periodic line currents array, has been performed. The metagrating system comprises a dielectric substrate and an array of periodic line currents. Therefore, the subsequent sections will further explore the electromagnetic attributes of the metagrating.

2.4.1 Analysis of reflective metagratings

In a reflective metagrating system, depicted in Figure 2.4, the upper face showcases periodically arranged cylindrical wires. Each period, denoted by Λ_y, comprises N metal wires. The distance of the p^{th} wire form the first wire is denoted as D_p (with $D_1 = 0$). The cylindrical wires have a radius r. The middle layer constitutes a dielectric substrate with permittivity $\varepsilon_s = \varepsilon_r\varepsilon_0$, and the bottom layer is a metal ground plane. Considering a TE-polarized wave of amplitude E_{in} obliquely incident on the surface at an angle θ_1, the incident wave is described as

$$E^{\text{in}} = E_{\text{in}} e^{-jk_0 \cos\theta_1 (z+h)} e^{-jk_0 \sin\theta_1 y} \tag{2.44}$$

The wavenumber and wave impedance in air and dielectric substrate are $k_0 = \omega\sqrt{\mu_0\varepsilon_0}$, $\eta_0 = \sqrt{\mu_0/\varepsilon_0}$, $k_s = \omega\sqrt{\mu_0\varepsilon_s}$ and $\eta_s = \sqrt{\mu_0/\varepsilon_s}$, respectively.

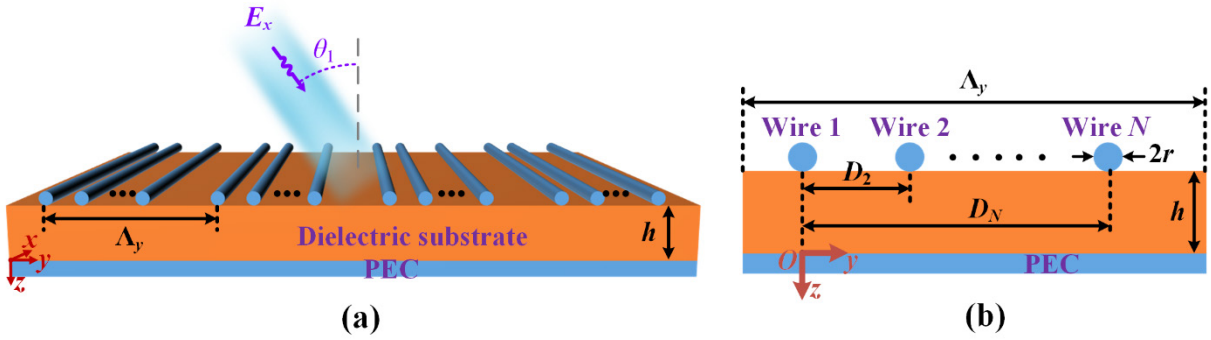

Figure 2.4: (a) Reflective metagratings under TE polarized oblique incidence. (b) Side view of the supercell (periodic cell) of the reflective metagratings.

The external incident field, comprising both the incident and reflected fields, can be expressed as

$$E^{\text{ext}}_{\text{source}} = E_{\text{in}}\left[e^{-jk_0 \cos\theta_1 (z+h)} + \Gamma e^{jk_0 \cos\theta_1 (z+h)}\right] e^{-jk_0 \sin\theta_1 y} \tag{2.45}$$

where Γ is the Fresnel reflection coefficient as given in Eq. (2.31).

Furthermore, based on the analysis in Section 2.3, under an external plane wave excitation, the array of cylindrical wires on the upper face of the reflective metagrating will exhibit a radiation field represented as

$$E^{\text{rad}} = -\frac{\eta_0 k_0}{4}\sum_{p=1}^{N}\sum_{n=-\infty}^{\infty} I_p e^{-jn\xi_0\Lambda_y} H_0^{(2)}\left(k_0\sqrt{(z+h)^2+\left(y+n\Lambda_y-D_p\right)^2}\right)$$
$$= -\frac{\eta_0 k_0}{2\Lambda_y}\sum_{m=-\infty}^{\infty}\left(\sum_{p=1}^{N} I_p e^{j\xi_m D_p}\right)\frac{1}{\beta_m} e^{-j\xi_m y} e^{-j\beta_m|z+h|} \tag{2.46}$$

where I_p is the line current amplitude in the p^{th} wire. Due to the presence of the grounded dielectric substrate, the radiation field will also generate reflections. Thus, the external field of the line currents' radiation (radiated field plus reflected field) is

$$E_{\text{line}}^{\text{ext}} = -\frac{\eta_0 k_0}{2\Lambda_y}\sum_{m=-\infty}^{\infty}\left(\sum_{p=1}^{N} I_p e^{j\xi_m D_p}\right)\frac{1}{\beta_m} e^{-j\xi_m y} e^{-j\beta_m|z+h|} \tag{2.47}$$

where Γ_m and β_m are the Fresnel reflection coefficient and longitudinal wave number in air of the m^{th} diffraction mode, and according to analysis in subsection 2.2.3, they are represented as

$$\Gamma_m = \frac{-\rho_m + j\tan(\beta_{sm}h)}{\rho_m + j\tan(\beta_{sm}h)} \tag{2.48}$$

$$\beta_m = \sqrt{k_0^2 - \xi_m^2} \tag{2.49}$$

with $\beta_{sm} = \sqrt{\varepsilon_r k_0^2 - \xi_m^2}$ being the longitudinal wave number in the substrate and $\rho_m = \beta_{sm}/\beta_m$.

The amplitude of the m^{th} order diffraction mode, as per Eqs. (2.45) and (2.47), is given by

$$E_m = -\frac{\eta_0 k_0}{2\Lambda_y}\frac{1+\Gamma_m}{\beta_m}\left(\sum_{p=1}^{N} I_p e^{j\xi_m D_p}\right) + \delta_{m,0} E_{\text{in}}\Gamma \tag{2.50}$$

where $\delta_{m,0}$ is the Dirac function. Furthermore, according to Poynting vector ratios, the power ratio P_m for the m^{th} order diffraction mode is expressed as [50]

$$P_m = \frac{|E_m|^2\beta_m}{|E_{\text{in}}|^2\beta_0}, \quad \sum P_m = 1 \tag{2.51}$$

Equation (2.50) provides insights into the influence of the N line currents in each period on the m^{th} order diffraction mode. Here, the current I_p acts as a variable affecting the amplitude of the propagating diffraction mode. By orchestrating the energy distribution of each diffraction mode in the metagratings, the required polarization current I_p can be determined, as elaborated in Eq. (2.51).

To induce the desired line currents for a given plane wave excitation, it's imperative to structure the cylindrical wires on the metagrating surface to impart a specific load impedance. This aspect is addressed in the subsequent analysis based on the near-field characteristics of the

metagrating surface. At the surface of the metagrating (z = -h), the total field is the sum of the external field from the excitation source and the external field from the line currents' radiation, expressed as $E^{\text{total}} = E^{\text{ext}}_{\text{source}} + E^{\text{ext}}_{\text{line}}$. Simultaneously, the total field can be represented as the product of the line current amplitude and the load impedance of the wire at the corresponding position, denoted as $E_p^{\text{total}} = I_p Z_p$. Consequently, the following relationship can be established:

$$\begin{bmatrix} Z_1 I_1 \\ Z_2 I_2 \\ \vdots \\ Z_N I_N \end{bmatrix} = \begin{bmatrix} E^{\text{ext}}_{\text{source}}(D_1, -h) \\ E^{\text{ext}}_{\text{source}}(D_2, -h) \\ \vdots \\ E^{\text{ext}}_{\text{source}}(D_N, -h) \end{bmatrix} - Q_{N\times N} \begin{bmatrix} I_1 \\ I_2 \\ \vdots \\ I_N \end{bmatrix} \tag{2.52}$$

with

$$Q_{N\times N} = \begin{bmatrix} Z(0,0) & Z(\Delta D_{2,1}, 0) \cdots Z(\Delta D_{N,1}, 0) \\ Z(\Delta D_{1,2}, 0) & Z(0,0) & \cdots Z(\Delta D_{N,2}, 0) \\ \vdots & \vdots & \ddots & \vdots \\ Z(\Delta D_{1,N}, 0) Z(\Delta D_{2,N}, 0) \cdots & Z(0,0) \end{bmatrix} \tag{2.53}$$

where $\Delta D_{p,q} = \left| D_p - D_q \right|$ and $Z(y,z)$ follows the defined function as per Eq. (2.42), expressed as

$$Z(y,z) = \begin{cases} \frac{\eta_0}{2\Lambda_y} T + j\frac{\eta_0}{\lambda_0}\left[\ln\left(\frac{\Lambda_y}{2\pi r}\right) + \sum_{m=1}^{\infty}\left(\frac{2\pi T_m}{\Lambda_y \alpha_m} - \frac{1}{m}\right)\right], & y = 0 \text{ and } z = 0 \\ \frac{\eta_0 k_0}{2\Lambda_y}\sum_{m=-\infty}^{\infty}\frac{1+\Gamma_m}{\beta_m} e^{-j\xi_m y} e^{-j\beta_m |z|}, & \text{else} \end{cases} \tag{2.54}$$

To maximize the efficiency of the metagrating, it is crucial to ensure that the resulting load impedance is passive and lossless. This requirement is expressed as an additional constraint equation

$$\Re(Z_p) = 0 \tag{2.55}$$

In conclusion, by combining Eqs. (2.50) - (2.55), the location and load impedance density of the reflective metagrating meta-atoms, capable of achieving the desired beam manipulations, can be calculated.

2.4.2 Analysis of transmissive metagratings

The analysis of transmissive metagratings follows a similar approach to that of reflective ones. In a transmissive metagrating, both the upper and lower faces feature periodically arranged cylindrical wires, as depicted in Figure 2.5. Each period length Λ_y contains N metal wires, with the distance of the p^{th} wire from the first wire in the upper and lower layers denoted as D_{pu} and D_{pl}, respectively (with $D_{1u} = D_{1l} = 0$). The radius of the cylindrical wire is r, and the middle layer is a dielectric substrate with permittivity $\varepsilon_s = \varepsilon_r \varepsilon_0$.

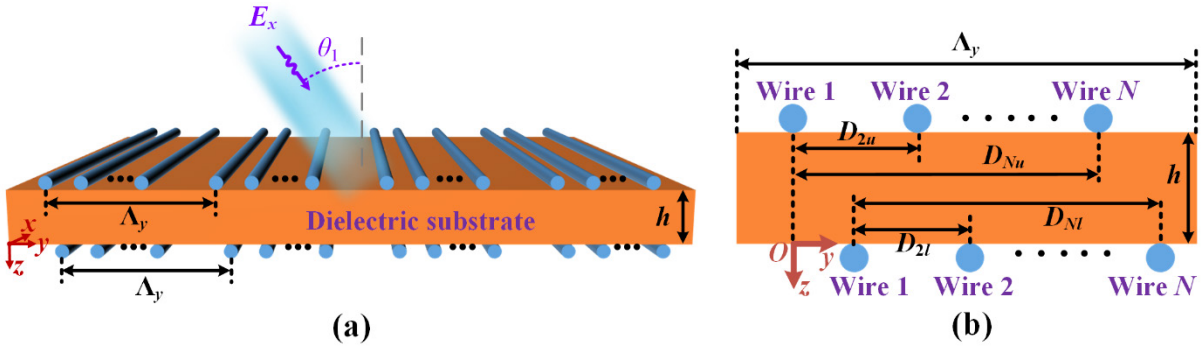

Figure 2.5: (a) Transmissive metagratings under TE polarized oblique incidence. (b) Side view of the supercell of the transmissive metagratings.

Considering a TE-polarized wave incident on the surface at an angle θ_1 with amplitude E_{in}, the incident wave is given by

$$E^{\text{in}} = E_{\text{in}} e^{-jk_0 \cos\theta_1 (z+h)} e^{-jk_0 \sin\theta_1 y} \tag{2.56}$$

The wavenumber and wave impedance in the air and dielectric substrate are $k_0 = \omega\sqrt{\mu_0\varepsilon_0}$, $\eta_0 = \sqrt{\mu_0/\varepsilon_0}$, $k_s = \omega\sqrt{\mu_0\varepsilon_s}$ and $\eta_s = \sqrt{\mu_0/\varepsilon_s}$, respectively.

The external incident field (incident field plus the reflected field) in upper space ($z \leq -h$) is given by

$$E^{\text{extu}}_{\text{source}} = E_{\text{in}}\left[e^{-jk_0 \cos\theta_1 (z+h)} + \Gamma e^{jk_0 \cos\theta_1 (z+h)}\right] e^{-jk_0 \sin\theta_1 y} \tag{2.57}$$

and in the lower space ($z \geq 0$) is

$$E^{\text{extl}}_{\text{source}} = E_{\text{in}} T e^{-jk_0 \cos\theta_1 z} e^{-jk_0 \sin\theta_1 y} \tag{2.58}$$

where Γ and T are the Fresnel reflection and transmission coefficients given in Eqs. (2.36) and (2.37). As expounded in Section 2.3, under the influence of external plane wave excitation, the collective arrangement of cylindrical wires positioned on the upper surface (free-space) of the transmissive metagrating demonstrates a radiation field denoted as

$$\begin{aligned} E^{\text{rad}}_u &= -\frac{\eta_0 k_0}{4} \sum_{p=1}^{N} \sum_{n=-\infty}^{\infty} I^u_p e^{-jn\xi_0 \Lambda_y} H_0^{(2)}\left(k_0 \sqrt{(z+h)^2 + \left(y + n\Lambda_y - D_{pu}\right)^2}\right) \\ &= -\frac{\eta_0 k_0}{2\Lambda_y} \sum_{m=-\infty}^{\infty} \left(\sum_{p=1}^{N} I^u_p e^{j\xi_m D_{pu}}\right) \frac{1}{\beta_m} e^{-j\xi_m y} e^{-j\beta_m |z+h|} \end{aligned} \tag{2.59}$$

Similarly, the radiation field associated with the array of cylindrical wires on the lower surface (free-space) can be expressed as

$$E^{\text{rad}}_l = -\frac{\eta_0 k_0}{4} \sum_{p=1}^{N} \sum_{n=-\infty}^{\infty} I^l_p e^{-jn\xi_0 \Lambda_y} H_0^{(2)}\left(k_0 \sqrt{z^2 + \left(y + n\Lambda_y - D_{pl}\right)^2}\right)$$

$$= -\frac{\eta_0 k_0}{2\Lambda_y}\sum_{m=-\infty}^{\infty}\left(\sum_{p=1}^{N} I_p^l e^{j\xi_m D_{pl}}\right)\frac{1}{\beta_m} e^{-j\xi_m y} e^{-j\beta_m |z|} \tag{2.60}$$

where I_p^u and I_p^l denote the amplitudes of line currents in the p^{th} wire on the upper and lower surfaces. Introduction of a dielectric substrate in the intermediate layer induces reflections and transmissions. Consequently, the external field of the line currents' radiation, encompassing both the radiation field and the reflected field, within the upper spatial domain ($z \le -h$), can be expressed as

$$E_{\text{line}}^{\text{ext}u} = -\frac{\eta_0 k_0}{2\Lambda_y}\sum_{m=-\infty}^{\infty}\left[\left(\sum_{p=1}^{N} I_p^u e^{j\xi_m D_{pu}}\right)\frac{1+\Gamma_m}{\beta_m} + \left(\sum_{p=1}^{N} I_p^l e^{j\xi_m D_{pl}}\right)\frac{T_m}{\beta_m}\right] e^{-j\xi_m y} e^{-j\beta_m |z+h|} \tag{2.61}$$

Furthermore, the external field associated with the radiation from the line currents within the lower spatial region ($z \ge 0$) is given by

$$E_{\text{line}}^{\text{ext}l} = -\frac{\eta_0 k_0}{2\Lambda_y}\sum_{m=-\infty}^{\infty}\left[\left(\sum_{p=1}^{N} I_p^l e^{j\xi_m D_{pl}}\right)\frac{1+\Gamma_m}{\beta_m} + \left(\sum_{p=1}^{N} I_p^u e^{j\xi_m D_{pu}}\right)\frac{T_m}{\beta_m}\right] e^{-j\xi_m y} e^{-j\beta_m z} \tag{2.62}$$

where Γ_m and T_m represent the Fresnel reflection and transmission coefficients in air of the m^{th} diffraction mode, as derived in Section 2.2.3, with their formulations provided as

$$\Gamma_m = \frac{j(1-{\rho_m}^2)\tan(\beta_{sm}h)}{2\rho_m + j(1+{\rho_m}^2)\tan(\beta_{sm}h)} \tag{2.63}$$

$$T_m = \frac{2\rho_m}{2\rho_m \cos(\beta_{sm}h) + j(1+{\rho_m}^2)\sin(\beta_{sm}h)} \tag{2.64}$$

Subsequently, in accordance with Eqs. (2.57) and (2.61), the amplitude of the m^{th} order reflection diffraction mode within the upper spatial domain ($z \le -h$) is represented as

$$E_m^u = -\frac{\eta_0 k_0}{2\Lambda_y}\left[\frac{1+\Gamma_m}{\beta_m}\left(\sum_{p=1}^{N} I_p^u e^{j\xi_m D_{pu}}\right) + \frac{T_m}{\beta_m}\left(\sum_{p=1}^{N} I_p^l e^{j\xi_m D_{pl}}\right)\right] + \delta_{m,0} E_{\text{in}} \Gamma \tag{2.65}$$

Similarly, in line with Eqs. (2.58) and (2.62), the amplitude of the m^{th} order transmission diffraction mode within the lower spatial domain ($z \ge 0$) is formulated as

$$E_m^l = -\frac{\eta_0 k_0}{2\Lambda_y}\left[\frac{1+\Gamma_m}{\beta_m}\left(\sum_{p=1}^{N} I_p^l e^{j\xi_m D_{pl}}\right) + \frac{T_m}{\beta_m}\left(\sum_{p=1}^{N} I_p^u e^{j\xi_m D_{pu}}\right)\right] + \delta_{m,0} E_{\text{in}} T \tag{2.66}$$

where $\delta_{m,0}$ is the Dirac function. Furthermore, the power ratios P_m^u and P_m^l associated with the m^{th} order reflection and transmission diffraction modes are expressed as [50]

$$P_m^u = \frac{|E_m^u|^2 \beta_m}{|E_{\text{in}}|^2 \beta_0}, \quad P_m^l = \frac{|E_m^l|^2 \beta_m}{|E_{\text{in}}|^2 \beta_0}, \quad \sum P_m^u + P_m^l = 1 \tag{2.67}$$

In line with reflective metagratings, Eqs. (2.65) and (2.66) delineate the collective

influence of N line currents on both upper and lower surfaces within each period on the m^{th} order reflection and transmission diffraction modes in transmissive metagratings. The parameters I_p^u and I_p^l serve as the variables governing the amplitudes of the propagating reflection and transmission diffraction modes. The determination of these polarization currents, I_p^u and I_p^l, is achieved through a design process aimed at establishing the energy distribution of each diffraction mode in the metagratings, as per Eq. (2.67).

To generate the desired line currents under a given plane wave excitation, it is crucial to engineer these cylindrical wires on both the upper and lower surfaces of the metagrating to possess specific load impedances. Subsequently, the analysis delves into the near-field characteristics of the metagrating surfaces. Analogous to reflective metagratings, at the upper surface (z = -h) of the transmissive metagrating, the following near-field relationship holds

$$\begin{bmatrix} Z_1^u I_1^u \\ Z_2^u I_2^u \\ \vdots \\ Z_N^u I_N^u \end{bmatrix} = \begin{bmatrix} E_{\text{source}}^{\text{ext}u}(D_{1u}, -h) \\ E_{\text{source}}^{\text{ext}u}(D_{2u}, -h) \\ \vdots \\ E_{\text{source}}^{\text{ext}u}(D_{Nu}, -h) \end{bmatrix} - Q_{N\times N}^{u(r)} \begin{bmatrix} I_1^u \\ I_2^u \\ \vdots \\ I_N^u \end{bmatrix} - Q_{N\times N}^{l(t)} \begin{bmatrix} I_1^l \\ I_2^l \\ \vdots \\ I_N^l \end{bmatrix} \tag{2.68}$$

with

$$Q_{N\times N}^{u(r)} = \begin{bmatrix} Z^r(0,0) & Z^r(\Delta D_{2,1}^u, 0) & \cdots & Z^r(\Delta D_{N,1}^u, 0) \\ Z^r(\Delta D_{1,2}^u, 0) & Z^r(0,0) & \cdots & Z^r(\Delta D_{N,2}^u, 0) \\ \vdots & \vdots & \ddots & \vdots \\ Z^r(\Delta D_{1,N}^u, 0) & Z^r(\Delta D_{2,N}^u, 0) & \cdots & Z^r(0,0) \end{bmatrix} \tag{2.69}$$

$$Q_{N\times N}^{l(t)} = \begin{bmatrix} Z^t(\Delta D_{1,1}, 0) & Z^t(\Delta D_{1,2}, 0) & \cdots & Z^t(\Delta D_{1,N}, 0) \\ Z^t(\Delta D_{2,1}, 0) & Z^t(\Delta D_{2,2}, 0) & \cdots & Z^t(\Delta D_{2,N}, 0) \\ \vdots & \vdots & \ddots & \vdots \\ Z^t(\Delta D_{N,1}, 0) & Z^t(\Delta D_{N,2}, 0) & \cdots & Z^t(\Delta D_{N,N}, 0) \end{bmatrix} \tag{2.70}$$

where $\Delta D_{p,q}^u = \left|D_{pu} - D_{qu}\right|$, $\Delta D_{p,q} = \left|D_{pl} - D_{qu}\right|$ and $Z^r(y,z)$ and $Z^t(y,z)$ are defined functions in accordance with Eq. (2.42), expressed as

$$Z^r(y,z) = \begin{cases} \frac{\eta_0}{2\Lambda_y}(1+\Gamma) + j\frac{\eta_0}{\lambda_0}\left[\ln\left(\frac{\Lambda_y}{2\pi r}\right) + \sum_{m=1}^{\infty}\left(\frac{2\pi(1+\Gamma_m)}{\Lambda_y \alpha_m} - \frac{1}{m}\right)\right], & y = 0, z = 0 \\ \frac{\eta_0 k_0}{2\Lambda_y}\sum_{m=-\infty}^{\infty}\frac{1+\Gamma_m}{\beta_m} e^{-j\xi_m y} e^{-j\beta_m|z|}, & \text{else} \end{cases} \tag{2.71}$$

$$Z^t(y,z) = \frac{\eta_0 k_0}{2\Lambda_y}\sum_{m=-\infty}^{\infty}\frac{T_m}{\beta_m} e^{-j\xi_m y} e^{-j\beta_m|z|} \tag{2.72}$$

For the lower surface of the transmissive metagrating at z = 0, the corresponding near-field relationship is given by

$$\begin{bmatrix} Z_1^l I_1^l \\ Z_2^l I_2^l \\ \vdots \\ Z_N^l I_N^l \end{bmatrix} = \begin{bmatrix} E_{\text{source}}^{\text{ext}l}(D_{1l}, 0) \\ E_{\text{source}}^{\text{ext}l}(D_{2l}, 0) \\ \vdots \\ E_{\text{source}}^{\text{ext}l}(D_{Nl}, 0) \end{bmatrix} - Q_{N\times N}^{l(r)} \begin{bmatrix} I_1^l \\ I_2^l \\ \vdots \\ I_N^l \end{bmatrix} - Q_{N\times N}^{u(t)} \begin{bmatrix} I_1^u \\ I_2^u \\ \vdots \\ I_N^u \end{bmatrix} \tag{2.73}$$

with

$$Q_{N\times N}^{l(r)} = \begin{bmatrix} Z^r(0,0) & Z^r(\Delta D_{2,1}^l, 0) \ldots Z^r(\Delta D_{N,1}^l, 0) \\ Z^r(\Delta D_{1,2}^l, 0) & Z^r(0,0) \quad \cdots Z^r(\Delta D_{N,2}^l, 0) \\ \vdots & \vdots \quad \ddots \quad \vdots \\ Z^r(\Delta D_{1,N}^l, 0) Z^r(\Delta D_{2,N}^l, 0) \cdots & Z^r(0,0) \end{bmatrix} \tag{2.74}$$

$$Q_{N\times N}^{u(t)} = \left[Q_{N\times N}^{l(t)}\right]^T \tag{2.75}$$

where $\Delta D_{p,q}^l = \left|D_{pl} - D_{ql}\right|$.

In the formulation of transmissive metagratings, the passive and lossess necessitates also adherence to the constraint defined in Eq. (2.55). Therefore, by integrating Eqs. (2.65)-(2.75) along with Eq. (2.55), it becomes feasible to determine the exact location and load impedance density of the meta-atoms within the transmissive metagrating. This process enables the achievement of the desired beam manipulations while maintaining passive and lossless behavior.

2.5 Period length selection in metagratings

The number of propagating diffraction modes in metagratings, as well as the angles corresponding to these modes, are directly influenced by the period length Λ_y. Therefore, selecting an appropriate period length is crucial in the design of wavefront manipulation using superlattice-based structures. In the following sections, I will analyze the selection of period length for both reflective and transmissive superlattices, respectively.

2.5.1 Period length selection in reflective metagratings

For simplicity, normal incidence is considered in the analysis, and the period length of the reflective metagratings is considered as Λ_y shown in Figure 2.4(b). Under this configuration, the number of diffraction modes will be odd, specifically $2|m|+1 = 3, 5, 7\ldots$ (m denotes the m^{th} diffraction order).

If $\lambda_0 < \Lambda_y < 2\lambda_0$, only three propagating diffraction modes are present, *i.e.*, $m = 1$, and the diffraction angle of the $+1^{\text{st}}$ order is given by $\theta_1 = \sin^{-1}(\frac{\xi_{+1}}{k_0})$, as depicted in Figure 2.6(a). Consequently, if the $+1^{\text{st}}$ order is chosen as the anomalous reflection beam, the beam manipulation range corresponds to the range of θ_1, which is $30° < \theta_1 < 90°$.

As illustrated in Figure 2.6(b), when the period Λ_y falls within $m\lambda_0 < \Lambda_y < (m+1)\lambda_0$, the metagrating exhibits additional propagating diffraction modes, *i.e.*, $2m+1$ diffraction modes. In this scenario, the range of anomalous reflection on the right side encompasses all ranges from

θ_1 to θ_m, where θ_m represents the diffraction angle of $+m^{th}$ order. The maximum angle of anomalous reflection is $\theta_{max} = 90°$, and the minimum angle of anomalous reflection is $\theta_{min} = \sin^{-1}(\frac{1}{m+1})$. The relationship of θ_{min} with m is depicted in Figure 2.6(c).

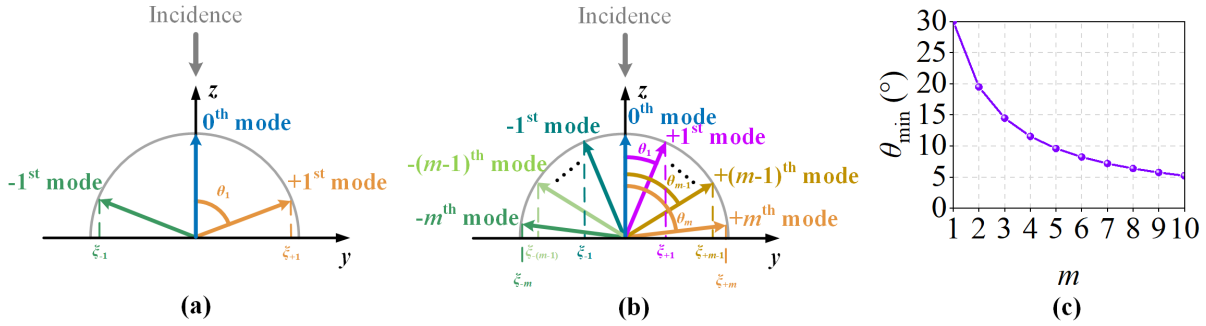

Figure 2.6: Wave vector diagram illustrating different diffraction Floquet modes of the reflective metagratings: (a) 3 modes, (b) 2|*m*|+1 modes. (c) θ_{min} under different maximum diffraction order *m*.

From the analysis above, it's evident that as the number of diffraction modes increases, the maximum angle of anomalous reflection remains constant at 90°, while the minimum angle changes from 30° toward to 5°, and the change trend gradually decelerates. Therefore, the choice of the period of reflective metagratings can be determined based on the range of diffraction patterns to be covered. In general, selecting 2|*m*|+1 = 3, *i.e.*, $\lambda_0 < \Lambda_y < 2\lambda_0$, is usually sufficient to fulfill most wavefront manipulation requirements.

2.5.2 Period length selection in transmissive metagratings

In the analysis of period length selection for transmissive metagratings, I also consider normally incident electromagnetic waves, with the period length denoted as Λ_y as depicted in Figure 2.5(b). In transmissive metagratings, there are twice as many diffraction modes compared to reflective metagratings for the same period length. Specifically, there are not only 2|*m*|+1 reflection diffraction modes (where *m* denotes the m^{th} diffraction order) but also 2|*m*|+1 transmission diffraction modes.

If $\lambda_0 < \Lambda_y < 2\lambda_0$, it results in *m* = 1, leading to six diffraction modes, as shown in Figure 2.7. Upon comparing Figure 2.7 with Figure 2.6(a), it becomes evident that although the number of diffraction modes in transmissive metagratings is doubled compared to reflective metagratings of the same period, the transmission diffraction modes are completely symmetric with the reflection diffraction modes.

Therefore, the selection strategy for the period length in reflective superlattices is also applicable in transmissive superlattices. This means that choosing $\lambda_0 < \Lambda_y < 2\lambda_0$ is generally

sufficient to fulfill most wavefront manipulation requirements.

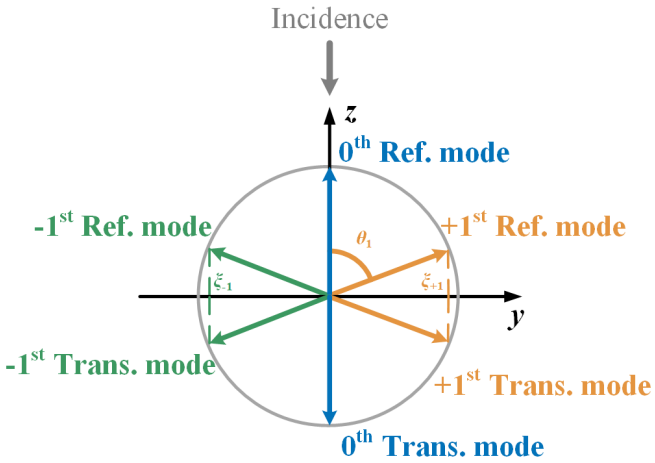

Figure 2.7: Wave vector diagram illustrating different diffraction Floquet modes of the transmissive metagratings when $2|m|+1 = 3$.

2.6 Conclusion

In this chapter, I delve into the analysis of four key aspects. Firstly, I scrutinize the reflection and transmission behaviors of electromagnetic waves within metagratings. Secondly, I explore the radiation characteristics of line current arrays in metagratings. Thirdly, my attention shifts towards comprehending the relationship between the energy distribution of metagrating diffraction modes and the spatial positioning, as well as the load impedance, of the meta-atoms comprising the metagratings. Finally, I undertake an analysis of the selection of the metagrating period length.

The primary focus of this chapter lies within the realm of physical modeling and the derivation of mathematical formulations. These formulations aim to establish a robust theoretical framework that will, in turn, facilitate the subsequent design of specific metagrating devices.

Chapter 3
Reflective metagratings for wavefront manipulation

Contents

3.1 Introduction

In Chapter 2, I delve into the analysis of electromagnetic characteristics in metagratings, elucidating the fundamental principles underlying wavefront manipulation. This includes the derivation of reflection and transmission coefficients in multilayer media, analysis of radiation characteristics, and design considerations for optimal wavefront manipulation. In this chapter, I will specifically focus on wavefront manipulation design based on reflective metagratings.

Researchers have conducted various wavefront manipulation designs based on reflective metagratings, encompassing two main types: anomalous reflection and beam splitting [27–33,46]. These wavefront manipulation by means of reflective metagratings offer several advantages, including the maintenance of high efficiency in deflected beams even at extreme angles, flexible and precise control over power ratio between split beams, and inherent simplicity in realizing metagrating structures.

In this chapter, I will undertake the design of anomalous reflection and beam splitting utilizing reflective metagratings. Unlike previous approaches, these designs will rely on fully analytical methods, thereby enhancing intuitive understanding and avoiding the need for numerical optimization processes. Additionally, I will introduce the concept of zero load impedance metagratings for anomalous reflection and beam splitting. Unlike conventional metagratings, zero load impedance metagratings can be designed solely with microstrip lines, rendering them more suitable for high-frequency applications. Finally, I will present the pioneering design of wave absorption based on reflective metagratings, detailing how different meta-atoms can be engineered to achieve diverse absorption bandwidths.

3.2 Reflective metagrating for efficient anomalous reflection and beam splitting

3.2.1 Theoretical analysis and calculations

In the design of reflective metagratings for anomalous reflection and beam splitting, simplifying the analyses and calculations by excluding the consideration of a dielectric substrate can enhance clarity and simplicity. A fully analytical design approach for reflective metagratings capable of anomalous reflection and beam splitting has been validated in existing literature [47]. However, dielectric substrates are inevitable components in practical implementations. Therefore, in this context, a more realistic model will be established to guide

the design of reflective metagratings for anomalous reflection and beam splitting, accounting for the presence of dielectric substrates.

The schematic of the considered reflective metagrating for highly efficient wavefront manipulation is depicted in Figure 3.1(a). It is illuminated by a TE-polarized $(E_y = E_z = H_x = 0)$ electromagnetic wave. The metagrating under consideration is a two-dimensional structure, invariant along the x-direction, and exhibits periodic alignment in the y-direction. The distance between the upper and lower surfaces along the z-direction is denoted as h. The side view of the supercell (period with length Λ_y) composing the metagrating with the established coordinate system is shown in Figure 3.1(b). The supercell contains two wires, both with radius r, separated by a distance d, and located on the upper layer of the dielectric substrate. The dielectric substrate is characterized by a permittivity $\varepsilon_2 = \varepsilon_r\varepsilon_0$ (where ε_0 is the permittivity of vacuum) and thickness h, backed by a continuous metallic sheet at $z = 0$. In the upper space of the metagrating ($z < -h$), the medium is free-space with permittivity $\varepsilon_1 = \varepsilon_0$.

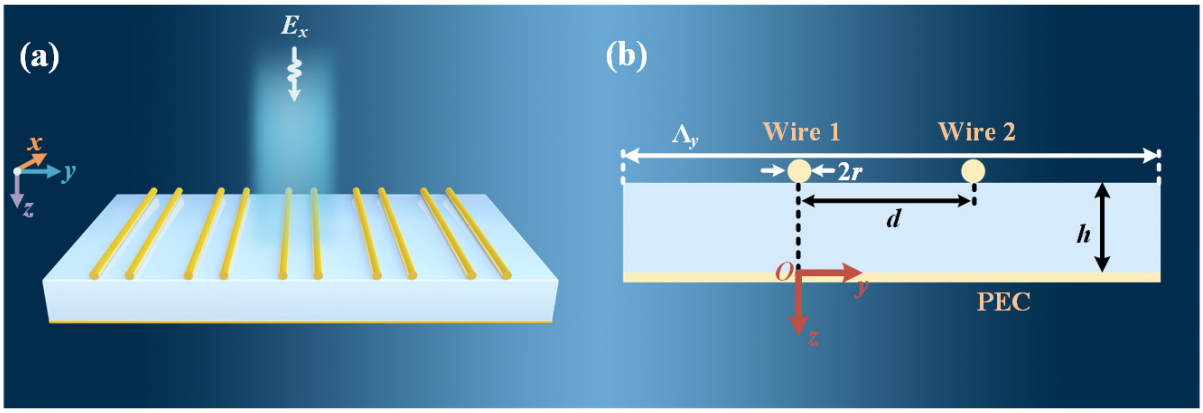

Figure 3.1: (a) Considered dual-wire reflective metagrating and excitation source. (b) Side view of the supercell (one period) composing the metagrating and its coordinate system for analysis.

Referring to Figure 3.1(b), the electric field of the exciting TE-polarized plane wave is represented as $E^{\text{in}} = E_{\text{in}}e^{-jk_0(z+h)}$ $(E_z = E_y = H_x = 0)$. The wavenumber and wave impedance of air are denoted as $k_0 = \omega\sqrt{\mu_0\varepsilon_0}$ and $\eta_0 = \sqrt{\mu_0/\varepsilon_0}$, respectively, while those of the dielectric substrate are $k_s = \omega\sqrt{\mu_0\varepsilon_s}$ and $\eta_s = \sqrt{\mu_0/\varepsilon_s}$, respectively, where $\varepsilon_s = \varepsilon_r\varepsilon_0$ is the permittivity of the substrate . The time harmonic dependence $e^{j\omega t}$ is assumed. Then, the field amplitude of the m^{th} diffraction mode E_m can be written following Eq. (2.50) as

$$E_m = -\frac{k\eta}{2\Lambda_y}\left(\frac{1+\Gamma_m}{\beta_m}\right)\left(I_1 + I_2 e^{j\xi_m d}\right) + \delta_{m0}E_{\text{in}}\Gamma = 0 \tag{3.1}$$

where Γ, Γ_m, and β_m are given in Eqs. (2.31), (2.48) and (2.49), respectively.

Based on the analysis in subsection 2.5.1, the period length of the metagrating is chosen

as $\lambda_0 < \Lambda_y < 2\lambda_0$, resulting in three diffraction modes. For wavefront manipulation, let's first consider single-beam manipulation, *i.e.*, anomalous reflection. Here, the +1st diffraction mode is chosen as the outgoing beam, while the -1st and 0th modes are considered to be suppressed. Thus, according to Eq. (3.1) it can be obtained that

$$\frac{k\eta}{2\Lambda_y}\left(\frac{1+\Gamma}{\beta_0}\right)\left(I_1 + I_2\right) - E_{\text{in}}\Gamma = 0 \tag{3.2}$$

$$\left(I_1 + I_2 e^{j\xi_{-1}d}\right) = 0 \tag{3.3}$$

To achieve multi-beam manipulation, the above equations are extended by introducing two auxiliary parameters (controllable variables) denoted as φ_1 and φ_2. Then, the expressions presented in Eqs. (3.2) and (3.3) can be reformulated in the following manner

$$\frac{k\eta}{2\Lambda_y}\left(\frac{1+\Gamma}{\beta_0}\right)\left(I_1 + I_2\right) - E_{\text{in}}\Gamma e^{j\varphi_1} = 0 \tag{3.4}$$

$$\left(I_1 + I_2 e^{j\varphi_2 d}\right) = 0 \tag{3.5}$$

Observing that when $\varphi_1 = 0$, Eq. (3.4) aligns with Eq. (3.2), signifying that the electric field amplitude of the 0th diffraction mode is zero. Similarly, when $\varphi_2 = \xi_{-1}$, Eq. (3.5) is identical to Eq. (3.3), indicating that the electric field amplitude of the -1st diffraction mode is zero. Analogously, when $\varphi_2 = \xi_1$, the electric field amplitude of the +1st diffraction mode is zero. Consequently, for values of φ_1 and φ_2 other than these specific cases, the electric field amplitudes of the three modes yield distinct results, suggesting the presence of multiple reflected beams.

By solving Eqs. (3.4) and (3.5), the expressions for the two line currents within one period can be derived as

$$I_1 = \frac{2\Lambda_y E_{\text{in}}\Gamma e^{j\varphi_1}}{\eta(1+\Gamma)\left(1-e^{-j\varphi_2 d}\right)} \tag{3.6}$$

$$I_2 = \frac{2\Lambda_y E_{\text{in}}\Gamma e^{j\varphi_1}}{\eta(1+\Gamma)\left(1-e^{j\varphi_2 d}\right)} \tag{3.7}$$

Furthermore, building upon the analysis in subsection 2.4.1, the total field at the surface of the metagrating (z = -h) is given by

$$E^{\text{tot}} = E_{\text{in}}(1+\Gamma) - I_1 Z(y, z+h) - I_2 Z(d-y, z+h) \tag{3.8}$$

where the defined function $Z(y,z)$ is expressed as per Eq. (2.54). By combining Ohm's law $Z_i = E^{\text{tot}}/I_i$, and following some algebraic simplification operations, the closed-form load impedance density Z_i (i = 1, 2) can be derived as

$$Z_i = -\frac{\eta}{2\Lambda_y}T_0 - j\frac{k\eta}{2\pi}\ln\left(\frac{\Lambda_y}{2\pi r}\right) + \frac{\eta}{2\Lambda_y}|T_0|^2\left(1 - e^{(-1)^i j\varphi_2 d}\right)e^{-j\varphi_1}$$

$$-j\frac{k\eta}{2\pi}\sum_{m=1}^{\infty}\left(\frac{2\pi T_m}{\Lambda_y\alpha_m}-\frac{1}{m}\right)+je^{(-1)^i j\varphi_2 d}\frac{k\eta}{2\Lambda_y}\sum_{m=-\infty}^{\infty}\frac{T_m}{\alpha_m}\cos(m\xi_1 d) \tag{3.9}$$

where T_m is m^{th} diffraction mode Fresnel transmission coefficient in air, which is represented as

$$T_m = 1+\Gamma_m = \frac{2j\tan(\beta_{sm}h)}{\rho_m + j\tan(\beta_{sm}h)} \tag{3.10}$$

To design passive and lossless metagratings, it is essential to pinpoint impedance densities where the real part is zero. By analyzing the composition of the real and imaginary parts of T_m and T_m/α_m for various values of m, specific expressions for the real and imaginary parts of the impedance densities (denoted as $\Re(Z_i)$ and $\Im(Z_i)$ for i = 1 or 2) can be derived as

$$\begin{aligned}\Re(Z_i) = {}& \frac{\eta}{4\Lambda_y}|T_0|^2\{[1-\cos(\varphi_2 d)](2\cos\varphi_1-1)+(-1)^i 2\sin(\varphi_2 d)\sin\varphi_1\}\\ & -(-1)^i\frac{\eta}{4\Lambda_y}\sin(\varphi_2 d)\left[\frac{\sqrt{\varepsilon_r}}{\tan(k_s h)}|T_0|^2+2\frac{\cos(\xi_1 d)}{\cos\theta_1}\frac{\beta_{s1}/\beta_1}{\tan(\beta_{s1}h)}|T_1|^2\right]\\ & -\frac{k\eta}{2\Lambda_y\beta_1}|T_1|^2[1-\cos(\varphi_2 d)\cos(\xi_1 d)]-(-1)^i\frac{k\eta}{\Lambda_y}\sin(\varphi_2 d)\sum_{m=2}^{\infty}\frac{T_m}{\alpha_m}\cos(m\xi_1 d)\end{aligned} \tag{3.11}$$

$$\begin{aligned}\Im(Z_i) = {}& G(d,h)-\frac{k\eta}{2\pi}\left[\ln\left(\frac{\Lambda_y}{2\pi r}\right)-1\right]+(-1)^i\frac{\eta}{2\Lambda_y}|T_1|^2\frac{\sin(\varphi_2 d)\cos(\xi_1 d)}{\cos\theta_1}\\ & -(-1)^i\frac{\eta}{4\Lambda_y}|T_0|^2[2\sin(\varphi_2 d+\varphi_1)-\sin(\varphi_2 d)]\end{aligned} \tag{3.12}$$

with

$$\begin{aligned}G(d,h) = {}& -\frac{\eta|T_0|^2}{4\Lambda_y}\left[2\sin\varphi_1+\frac{[1-\cos(\varphi_2 d)]\sqrt{\varepsilon_r}}{\tan(k_s h)}\right]-\frac{\eta(\beta_{s1}/\beta_1)|T_1|^2}{2\Lambda_y\cos\theta_1}\times\\ & \frac{1-\cos(\varphi_2 d)\cos(\xi_1 d)}{\tan(\beta_{s1}h)}-\frac{k\eta}{\Lambda_y}\sum_{m=2}^{\infty}\left(\frac{T_m}{\alpha_m}-\frac{\Lambda_y}{2\pi m}\right)+\frac{k\eta}{\Lambda_y}\cos(\varphi_2 d)\sum_{m=2}^{\infty}\frac{T_m}{\alpha_m}\cos(m\xi_1 d)\end{aligned} \tag{3.13}$$

where θ_1 is the reflection angle of $+1^{\text{st}}$ diffraction mode, $\beta_{sm}=\sqrt{\varepsilon_r k^2-\xi_m^2}$ is the longitudinal wave number of m^{th} mode in substrate, and $|T_m|^2$ is calculated as.

$$|T_m|^2 = \frac{4\tan^2(\beta_{sm}h)}{\tan^2(\beta_{sm}h)+(\beta_{sm}/\beta_m)^2} \tag{3.14}$$

Through mathematical manipulation, the conditions $\Re(Z_1)=0$ and $\Re(Z_2)=0$ can be converted into the equivalent conditions $\Re(Z_1)+\Re(Z_2)=0$ and $\Re(Z_1)-\Re(Z_2)=0$. Consequently, the conditions ensuring the real part of the impedance densities to be zero can be expressed as

$$(2\cos\varphi_1-1)\frac{|T_0|^2}{|T_1|^2}-\frac{2}{\cos\theta_1}\frac{1-\cos(\varphi_2 d)\cos(\xi_1 d)}{1-\cos(\varphi_2 d)}=0 \tag{3.15}$$

$$\sin(\varphi_2 d)\left[\begin{array}{l}(\sin\varphi_1+\frac{\sqrt{\varepsilon_r}}{2\tan(k_s h)})|T_0|^2+\frac{\cos(\xi_1 d)(\beta_{s1}/\beta_1)}{\cos\theta_1\tan(\beta_{s1}h)}|T_1|^2\\ \quad +2k\sum_{m=2}^{\infty}\frac{T_m}{\alpha_m}\cos(m\xi_1 d)\end{array}\right]=0 \tag{3.16}$$

At this juncture, the analytical expressions for the impedance densities of the metagrating, along with their corresponding passive and lossless conditions, have been derived. Moving forward, how to manipulate the power distribution of each diffraction mode in accordance with the introduced auxiliary parameters φ_1 and φ_2 will be discussed. The power ratio of the m^{th} diffraction mode P_m in the metagrating is governed by the following Eq. (2.51). Subsequently, for the propagating three diffraction modes, it can be obtained that

$$P_0=\frac{|E_0|^2\beta_0}{|E_{\text{in}}|^2\beta_0}=2-2\cos\varphi_1 \tag{3.17}$$

$$P_{-1}=\frac{|E_{-1}|^2\beta_{-1}}{|E_{\text{in}}|^2\beta_0}=\left(\cos\varphi_1-\frac{1}{2}\right)\left[\frac{1-\cos(\varphi_2+\xi_1)d}{1-\cos(\varphi_2 d)\cos(\xi_1 d)}\right] \tag{3.18}$$

$$P_1=\frac{|E_1|^2\beta_1}{|E_{\text{in}}|^2\beta_0}=\left(\cos\varphi_1-\frac{1}{2}\right)\left[\frac{1-\cos(\varphi_2-\xi_1)d}{1-\cos(\varphi_2 d)\cos(\xi_1 d)}\right] \tag{3.19}$$

Based on the chosen values of P_0, P_{-1}, and P_1, and incorporating Eqs.(3.15) and (3.16), the corresponding parameters φ_1, φ_2, d and h can be analytically calculated. Subsequently, substituting these calculated parameters back into Eq.(3.9), we can calculate the required reactive impedance densities Z_1 and Z_2 of the metagrating to achieve the desired beam manipulation. It is important to note that we must exclude values of the parameter h that render the denominator of the line currents zero in Eqs. (3.6) and (3.7), *i.e.*, $1+R_0\neq 0$, leading to $h\neq n\lambda_0/2\sqrt{\varepsilon_r}, (n=0,1,2\cdots)$.

3.2.2 Design of the supercell

To validate our proposed methodology, a proof-of-study study is conducted, which is numerically and experimentally reported for beam manipulation schemes. The operational frequency of the metagrating is set to 10 GHz. The dielectric substrate is selected as F4BM300 with a relative permittivity $\varepsilon_s = 3\varepsilon_0$ and loss tangent $\tan\delta = 0.0007$, possessing a thickness denoted by h. Based on the analysis in subsection 3.2.1, for different beam manipulations, the corresponding required impedance densities can be calculated using Eqs.(3.15)-(3.19). Upon calculation, it is observed that the impedance densities are predominantly negative imaginary numbers. Considering the practical feasibility of the model, the wires are substituted by meta-atoms featuring microstrip capacitor structures to achieve the requisite impedance density of the wires, as illustrated in Figure 3.2(a). The material of the meta-atom is copper, with the microstrip wire characterized by a thickness denoted as $t = 0.018$ mm and a width denoted as w

= $4r$ = 0.2 mm (where r represents the radius of the cylindrical wire), as outlined in previous research [48]. The gap of the capacitor is designated as g = 0.2 mm, and the width is denoted by L, which is determined by the required load impedance density Z, as given by Equation [48]

$$L = jK\frac{\eta\lambda}{4Z\varepsilon_{\text{eff}}\Lambda_x \ln\left(\sin\frac{\pi w}{2\Lambda_x}\right)} \tag{3.20}$$

where K represents the correction factor, accounting for minor differences between the actual copper microstrip line used and the ideal perfect conductor for calculation. To evaluate K, the configuration corresponding to the desired beam manipulation (chosen arbitrarily) is considered, and the capacitor width is swept around the value predicted by Eq.(3.20) without correction (K = 1) to determine the actual optimal L value, maximizing power coupling to the desired diffraction modes. The ratio between the uncorrected and the optimal L values yields the required correction factor, found to be K = 0.963 in this study. Furthermore, $\varepsilon_{\text{eff}} = (\varepsilon_1+\varepsilon_2)/2$ denotes the effective permittivity at the interface between air and the substrate.

The dimensions of the metagrating supercell in the x- and y-directions are designated as $\Lambda_x = \lambda_0/10$ (this value can be taken arbitrarily, but typically tends to be a relatively small sub-wavelength value in order to ensure uniformity of impedance density) and $\Lambda_y = \lambda_0/\sin\theta_1$ (θ_1 is the angle of the +1st diffraction mode), respectively, as depicted in Figure 3.2(b).

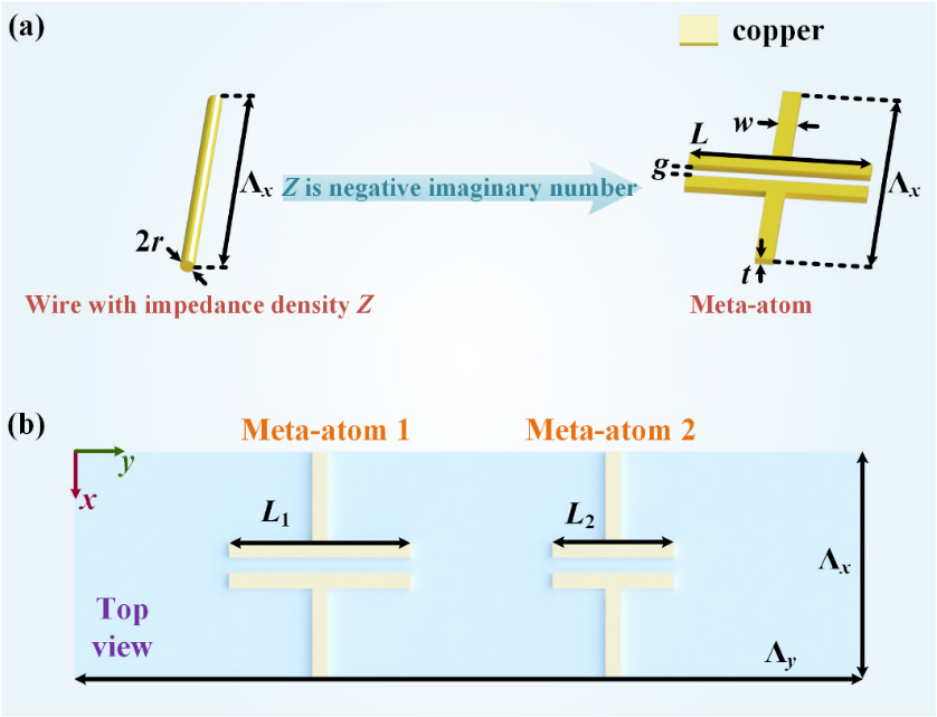

Figure 3.2: (a) Realization of meta-atoms with reactive load impedance density using microstrip line capacitor. (b) Top view of the metagrating supercell.

3.2.3 Single-beam manipulation

For single-beam manipulation, designs targeting a 60° reflection are considered, as depicted in Figure 3.3. Once the angle and power ratio of each diffraction order are determined, the constellation and the load impedance density of each meta-atom in the supercell are calculated using Eqs.(3.15)-(3.19). Subsequently, the dimensions of the meta-atoms can be ascertained, and the final parameters of the metagrating supercell are provided in Table 3.1.

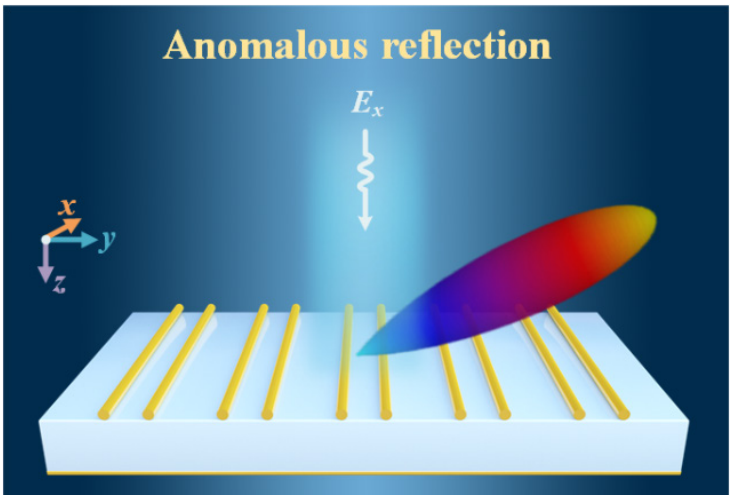

Figure 3.3: Conceptual diagram illustrating single-beam manipulation.

Table 3.1. Parameters of the metagratings with 60° anomalous reflection

Parameters \ Supercell type	Anomalous reflection
Λ_x (mm)	3
Λ_y (mm)	34.64
h (mm)	2.48
d (mm)	9.30
Z_1 (η/λ)	$-j5.5596$
Z_2 (η/λ)	$-j4.8862$
L_1 (mm)	2.87
L_5 (mm)	3.26

To validate the proposed design methodology, the supercell of the metagrating is simulated in ANSYS HFSS, incorporating periodic boundary conditions in the x- and y-directions. The anomalous reflection diagram of the metagratings is depicted in Figure 3.4(a), and the simulated performance of the corresponding supercell is illustrated in Figure 3.4(b). The results demonstrate that the energy of the incidence is almost fully coupled to the desired $+1^{st}$ mode, with less than 0.05% of the power radiated in the direction of undesired diffraction modes (-1^{st}

and 0th modes). The inevitable dielectric losses and Joule losses amount to approximately 1.71% and 2.53%.

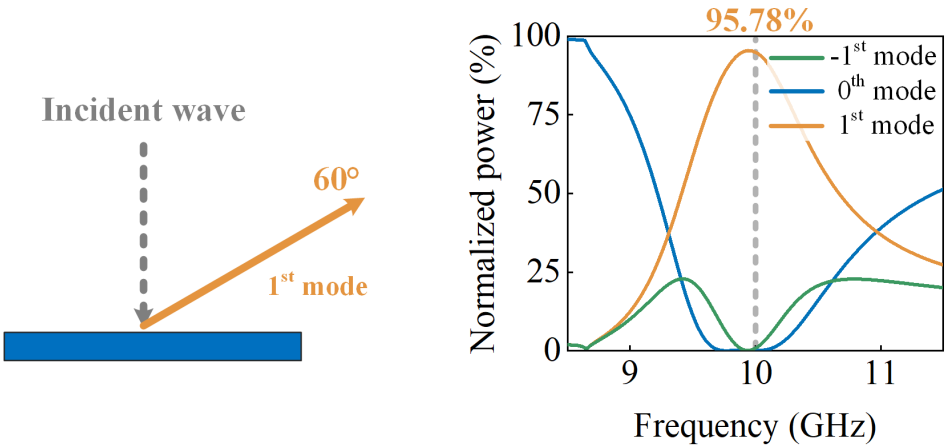

Figure 3.4: Beam manipulation scheme and simulation results of the supercells for anomalous reflection.

3.2.4 Multi-beam manipulation

For multi-beam manipulation, the study explores dual- and three-beam splitting configurations, as illustrated in Figure 3.5. In the case of dual-beam splitting, it considers beams directed towards 50°-reflection/-50°-reflection angles with a power ratio of 1:2 for the -1st mode to the +1st mode, denoted as $P_{-1} = 1/3$ and $P_1 = 2/3$ respectively. For three-beam splitting, beams pointing at -35°-reflection/0°-reflection/35°-reflection with a power ratio of 2:1:3 for the -1st mode to the 0th mode to the 1st mode are considered, expressed as $P_{-1} = 1/3$, $P_0 = 1/6$ and $P_1 = 1/2$.

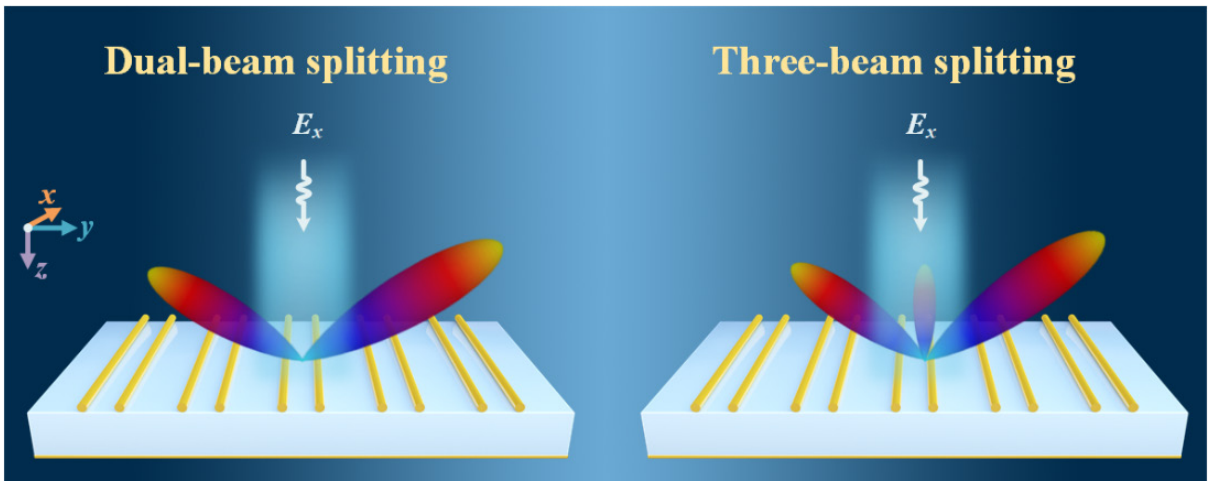

Figure 3.5: Conceptual diagram illustrating multi-beam manipulation: (a) dual-beam splitting, (b) three-beam splitting.

Subsequently, employing Eqs.(3.15)-(3.19), the constellation and the load impedance

density of each meta-atom within the supercell are computed. This computation facilitates the determination of meta-atom dimensions, leading to the final parameters of the metagrating supercells provided in Table 3.2.

Table 3.2. Parameters of the metagratings with dual- and three-beam splitting

Parameters \ Supercell type	**Dual-beam splitting**	**Three-beam splitting**
Λ_x (mm)	3	3
Λ_y (mm)	39.16	52.30
***h* (mm)**	3.30	3.64
***d* (mm)**	8.78	14.58
Z_1 (η/λ)	*-j*5.7229	*-j*5.9759
Z_2 (η/λ)	*-j*5.4250	*-j*5.7843
L_1 (mm)	2.81	2.70
L_5 (mm)	2.97	2.78

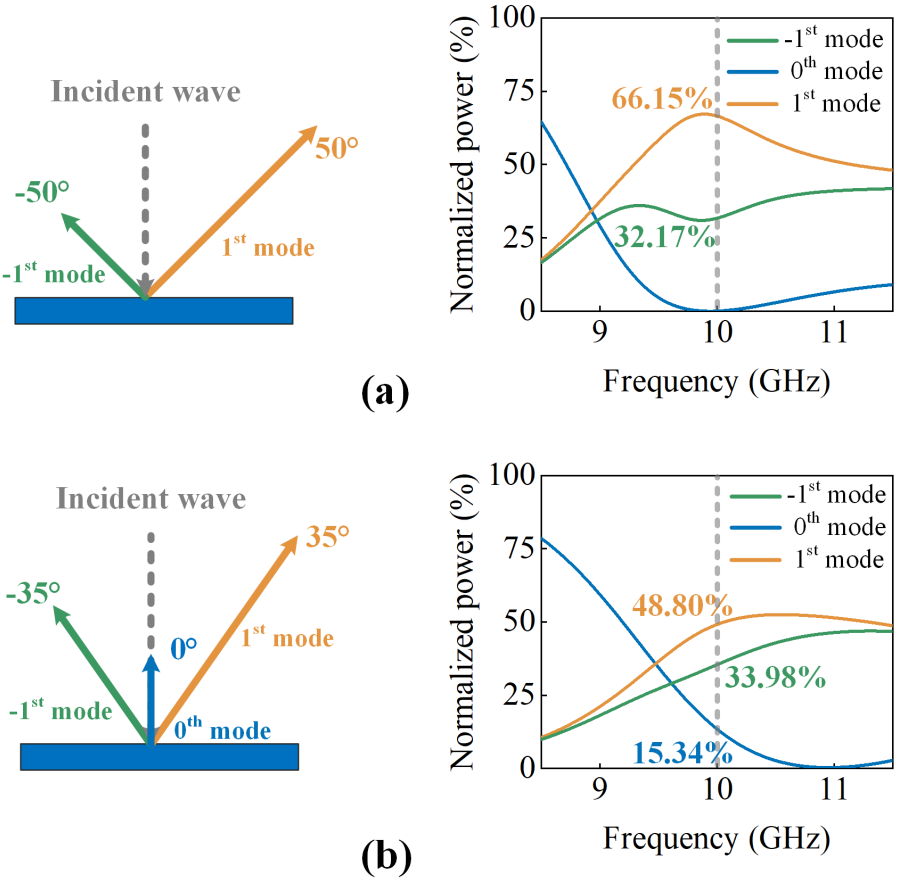

Figure 3.6: Beam-splitting scenarios and simulation results of the supercells: (a) Dual-beam beam splitting, (b) three-beam beam splitting.

The schematics illustrating dual-beam and three-beam splitting are presented in Figure

3.6(a) and Figure 3.6(b) respectively, while the simulated performances of the corresponding supercells are depicted in the right side of Figure 3.6(a) and Figure 3.6(b). Analysis of the simulation results indicates that the power ratios among the split beams closely match the theoretical predictions. In both designs, the presence of unavoidable dielectric and Joule losses is noted. Specifically, for dual-beam splitting, dielectric losses account for 0.8% of the total loss, while Joule losses contribute 0.87%. Similarly, for three-beam splitting, dielectric losses constitute 0.8% of the total loss, while Joule losses contribute 0.98%. Notably, less than 1% of the power is observed to be radiated in the direction of undesired diffraction modes for both designs, with values of 0.01% for dual-beam splitting and 0.8% for three-beam splitting. The relatively lower total loss compared to single-beam manipulation is primarily attributed to the thickness h of the dielectric substrate used, resulting in a reduced polarization current amplitude as defined in Eqs. (3.6) and (3.7).

3.2.5 Experimental validation

To validate the proposed design methodology through experimental means, the parameters detailed in Tables 3.1 and 3.2 are employed for fabricating three metagrating boards utilizing classical PCB technology. Photographic representations of the resulting samples are provided in Figure 3.7(a)-(c). These proof-of-concept prototypes consist of 67 × 12 supercells in both the x- and y-directions for the first and second boards, and 67 × 9 supercells in the x- and y-directions for the third board. Consequently, their dimensions are 201 mm × 415.68 mm, 201 mm × 469.92 mm, and 201 mm × 470.70 mm, respectively.

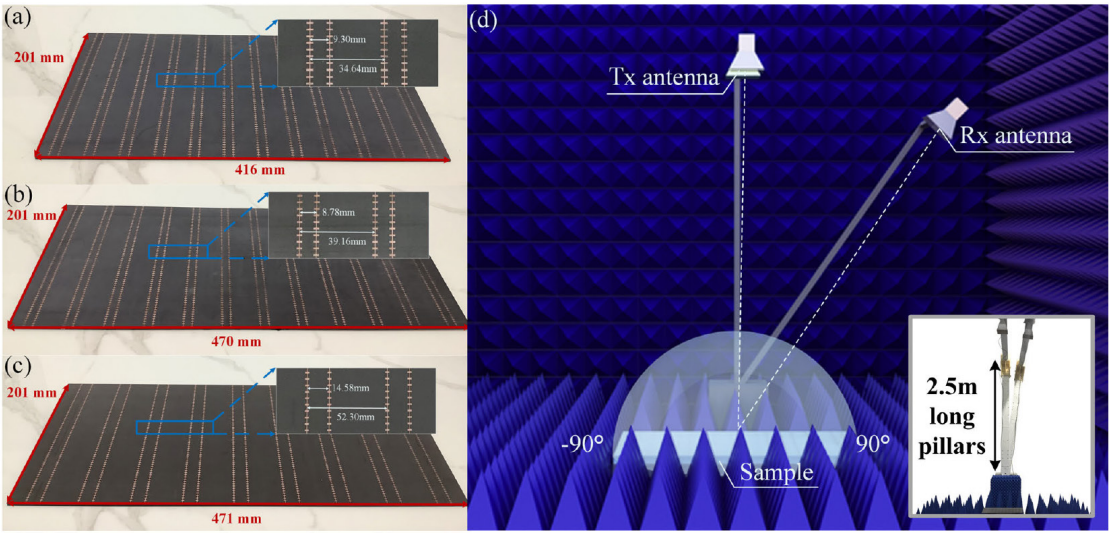

Figure 3.7: Prototypes of the fabricated metagratings: (a) Anomalous reflection, (b) Dual-beam beam splitting, (c) Three-beam beam splitting. (d) Schematic diagram of the measurement setup.

Experimental measurements are conducted utilizing the setup depicted in Figure 3.7(d). This setup features two horn antennas covering the 10 GHz operation, each connected to a port of a network analyzer to serve as transmitting and receiving antennas. Positioned on a rotatable arm, these antennas are situated at a distance of 2.5 m from the metagrating. This arrangement aims to achieve a quasi-plane wave illumination configuration as closely as possible.

In metagrating board simulations, the metagrating is situated within an air box with radiation boundary conditions applied on its faces, while a Gaussian beam excitation serves as the illumination source. The normalized power of the far field results is obtained by recording the scattered wave from the metagrating plate in measurements, as depicted in Figure 3.8(a)-(c). In these figures, the dashed line represents simulation results, while the solid line represents experimental results.

Concurrently, the efficiency of the various scattered beams is presented, showcasing good agreement with predefined objectives. The normalized power η_{sca} scattered in a desired diffraction order m is calculated using the equation [31]

$$\eta_{\text{sca}} = \frac{\int_{\theta_m^1}^{\theta_m^2} P(\theta)d\theta}{\sum_m \int_{\theta_m^1}^{\theta_m^2} P(\theta)d\theta} \tag{3.21}$$

where $P(\theta)$ represents the power scattered at angle θ, and θ_m^1 and θ_m^2 denote the angles where the scattered power is 3 dB less than the peak value in the direction of the m^{th} diffraction order.

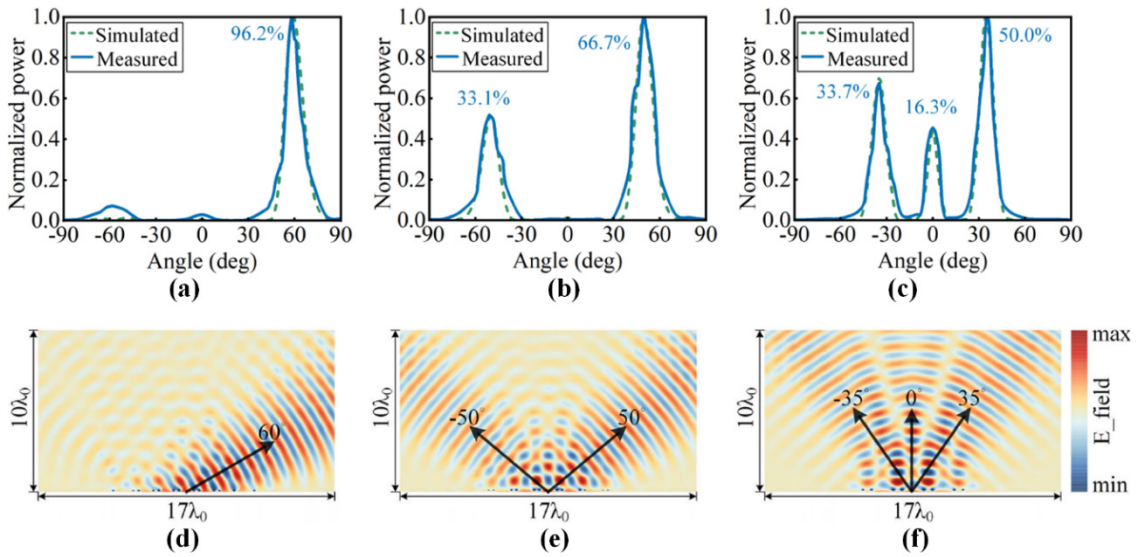

Figure 3.8: (a) Far-field simulation and measurement results of the fabricated metagrating board for anomalous reflection, (b) dual-beam beam splitting, (c) three-beam beam splitting. Near-field simulation results of the fabricated metagrating board for (d) anomalous reflection, (e) dual-beam beam splitting, (f) three-beam beam splitting.

The values depicted in Figure 3.8(a) indicate that less than 4% of the scattered power is directed into undesired 0^{th} and -1^{st} diffraction orders. Conversely, in the supercell simulation result (without considering losses), only 0.02% of the power is coupled to unwanted diffraction modes. The discrepancy between array results and supercell results is attributed to the finite plate size, suggesting the need for larger plate dimensions to minimize such deviations.

Regarding the dual-beam splitting simulation result illustrated in Figure 3.8(b), 0.2% of the scattered power is lost in the specular reflection. Similarly, for three-beam splitting depicted in Figure 3.8(c), the power ratios of the beams closely match expectations.

Lastly, the near-field distribution extracted from full-wave simulations, as shown in Figure 3.8(d)-(f), clearly indicates that the angles of the reflected beams align with the different diffraction orders previously depicted in Figure 3.4 and Figure 3.6.

3.3 Zero load-impedance metagratings

3.3.1 Synthesis and analysis

In Subsection 3.2, a comprehensive analytical design methodology was introduced for achieving efficient anomalous reflection and beam splitting using reflective metagratings, with execution at 10 GHz and validation through simulations and experiments. While the design constrained the real part of the load impedance density to zero to ensure passivity and losslessness, implementing the imaginary part of the load impedance density necessitated microstrip capacitor structures of varying sizes, which may pose challenges with increasing operating frequencies due to precision limitations in PCB fabrication technology.

In this subsection, I will discuss the design concept of zero load-impedance metagratings. In this approach, meta-atoms no longer require designs as capacitive or inductive structures with tailored reactive values. Instead, focus is solely on the width of the microstrip lines, composed of a periodic arrangement of simple planar metal wires, significantly reducing design complexity and potentially facilitating implementation at higher frequencies.

The analysis and design continue based on the established metagrating system depicted in Figure 3.1(a). However, unlike the design discussed previously, the difference lies in the supercell configuration shown in Figure 3.1(b). Specifically, in the supercell under consideration here, wire 1 and wire 2 have different radii denoted as r_1 and r_2, respectively, as illustrated in Figure 3.9 (a). This change aims to increase the degree of freedom in the design process with the goal of achieving zero load impedance metagratings.

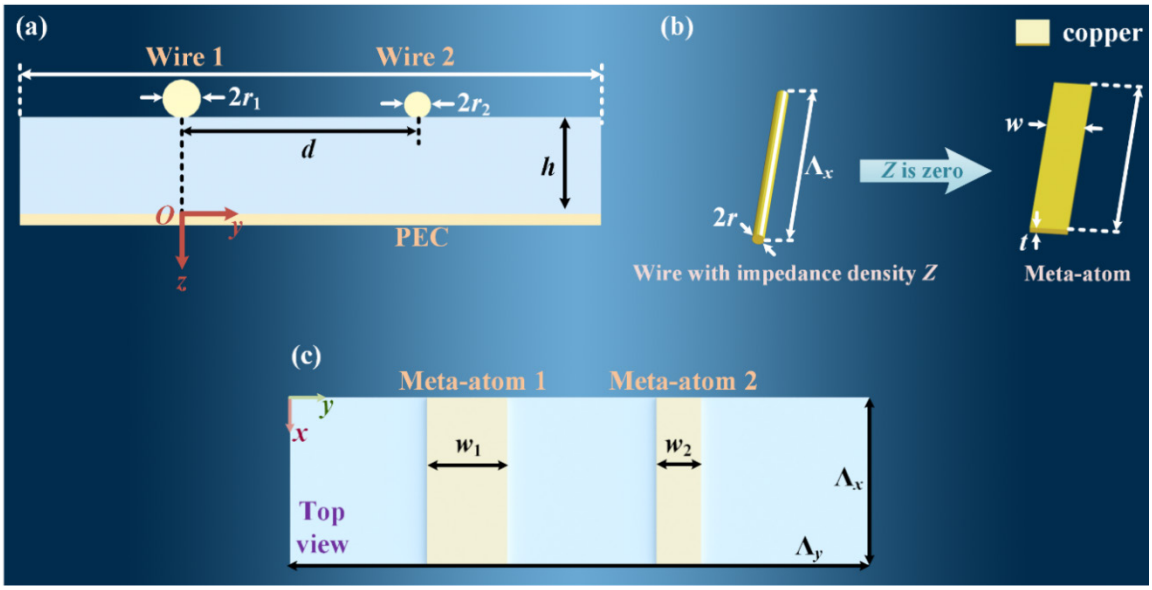

Figure 3.9: (a) Side view of the supercell composing the zero load impedance metagratings. (b) Realization of meta-atoms with zero load impedance density directly using microstrip lines. (c) Top view of the zero load-impedance metagratings supercell

Zero load impedance necessitates both the real and imaginary parts of the impedance of the metagrating wires to be zero. For the condition where the real part is zero, it continues to adhere to Eqs.(3.15) - (3.19). Furthermore, since the specific expression for the imaginary part of the impedance density $\Im(Z)$ has been obtained in Eqs.(3.12) and (3.13), here, setting $\Im(Z) = 0$ determines the values of r_1 and r_2 for realizing the zero load-impedance metagrating. Based on the analysis in Subsection 3.2.2, in the actual PCB implementation, it is necessary to transform the cylindrical wire equivalent into a microstrip line, as shown in Figure 3.9 (b), with the width of the microstrip line w related to the radius of the cylindrical wire r as $w = 4r$ [48]. Therefore, the values of the parameters w_1 and w_2 in the supercell can be obtained as

$$w_i = \frac{2\Lambda_y}{\pi e}\exp\left[-\frac{\lambda}{\Lambda_y}G(d,h) + (-1)^i \frac{\lambda}{2\Lambda_y}\frac{|T_1|^2}{\cos\theta_1}\frac{1-\cos(\xi_1 d)}{1-\cos(\varphi_2 d)}\sin(\varphi_2 d)\right] \tag{3.22}$$

where e represents the natural logarithm base (e = 2.718281828), and $G(d, h)$ is expressed as per Eq. (3.13).

Finally, the supercell of the zero load impedance metagrating can be constructed as shown in Figure 3.9 (c) with dimensions in the x-direction and y-direction considered as $\Lambda_x = \lambda/10$ and $\Lambda_y = \lambda/\sin\theta_1$ (θ_1 is the angle of the +1st diffraction mode), respectively.

3.3.2 Single-beam manipulation

For single-beam manipulation, designs involving 45° reflection are considered, with the

$+1^{st}$ mode designated as the outgoing beam, as depicted in Figure 3.3. Once the angle and power ratio of each diffraction order are determined, the constellation and the width of each meta-atom in the supercell can be calculated using Eqs.(3.15)-(3.19) and (3.22). Subsequently, the dimensions of the meta-atoms can be ascertained, leading to the final parameters of the metagrating supercell.

It is essential to note that since the copper microstrip line used in this design inherently contains a portion of the real part of the load impedance (a small resistance) as well as the imaginary part of the impedance (a small inductance), the calculated parameters (h, d, w_1, w_2) of the zero load-impedance metagrating require further optimization through simulations. The entire design flow is depicted in Figure 3.10. The overall design process can be summarized as follows: the geometrical parameters of the supercell under ideal conditions are initially calculated, and subsequent parameter optimization based on the calculated values is carried out using full-wave simulations to obtain the final parameters of the supercell. Finally, all the parameters of the zero load-impedance metagrating supercell are calculated and optimized, and are listed in Table 3.3, where ICV represents the initial calculated value and FOV represents the final optimized value.

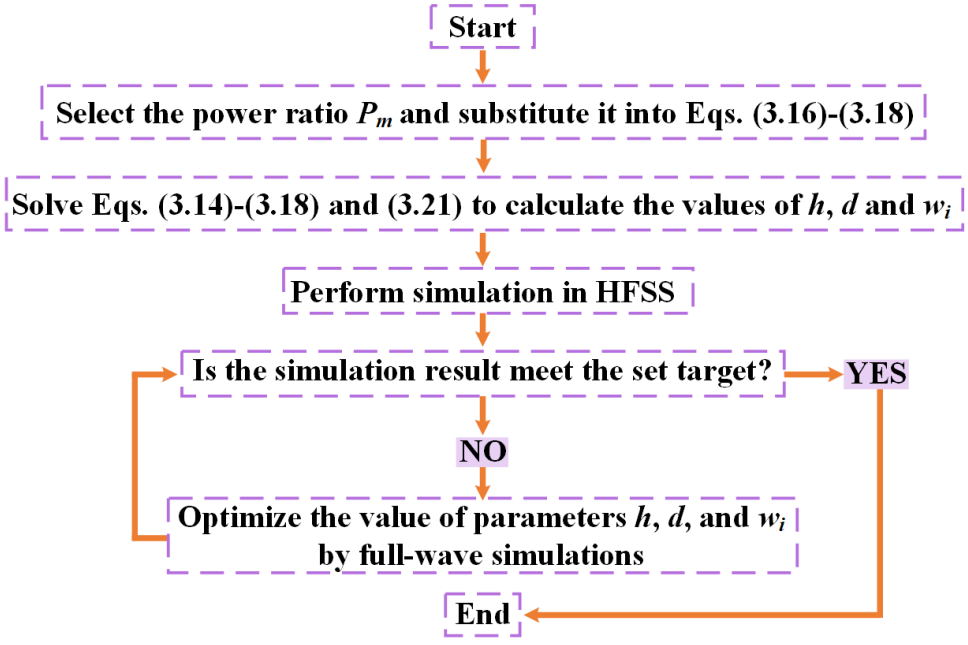

Figure 3.10: Flowchart of the supercell design procedure.

To validate the proposed design methodology, the supercell of the metagrating is simulated in ANSYS HFSS at an operating frequency of 30 GHz. The dielectric substrate chosen is F4BM300 ($\varepsilon_s = 3\varepsilon_0$ and $\tan\delta = 0.0007$) with a thickness h. The corresponding simulation result for the supercell is presented in Figure 3.11.

From the simulation result, it is observed that initially, the initial calculated values (ICVs) lead to only 79.36% of the power coupled to the desired +1st mode. However, after optimization, the power coupled to the +1st mode rises to 89.30%. Approximately 5.86% of the incident power is coupled to the unwanted 0th and -1st diffraction orders, with an additional 4.84% of power consumed due to dielectric losses as well as ohmic losses (dielectric losses: 4.46%, ohmic losses: 0.38%).

Table 3.3. Parameters of the supercell of the zero metagratings for single-beam manipulation

Data types \ Parameters		Λ_y (mm)	h (mm)	d (mm)	w_1 (mm)	w_2 (mm)
Anomalous reflecton	ICV	14.14	4.86	8.39	0.33	2.64
	FOV	**14.14**	**4.96**	**8.43**	**0.46**	**2.49**

ICV: initial calculated value, FOV: final optimized value.

Comparing with the results in Figure 3.4, it can be inferred that although the zero impedance metagrating is structurally simpler, there is a higher amount of power coupling to the unwanted diffraction modes. Therefore, the conventional structural metagrating remains a preferable choice for low-frequency bands, whereas zero impedance metagratings cater more to the needs of high-frequency band applications.

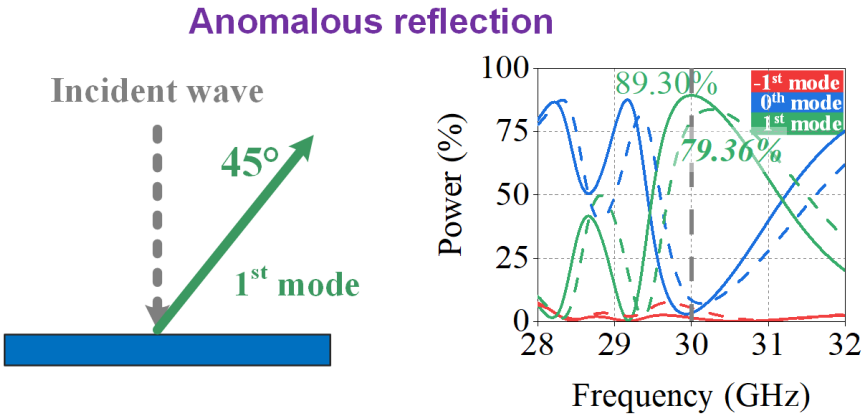

Figure 3.11: Beam manipulation scheme and simulation results of the supercells for anomalous reflection. (The dashed lines indicate the simulation results using the initial calculated values, while the solid lines indicate the simulation results using the final optimized values).

3.3.3 Multi-beam manipulation

For multi-beam manipulation, dual-beam splitting with various outgoing angles and power ratios are considered, as depicted in Figure 3.5(a). In this scenario, the -1st mode and the +1st

mode are designated as the outgoing beams. Three distinct beam manipulation designs are analyzed: beam splitting I, with reflection angles at -50° and 50° with a power ratio of 1:2; beam splitting II, with reflection angles at -70° and 70° with a power ratio of 1:2; and beam splitting III, with reflection angles at -50° and 50° with a power ratio of 1:4.

Similarly, the constellation and the load impedance density of each meta-atom in the supercell can be initially calculated using Eqs.(3.15)-(3.19) and (3.22) based on the determined angle and power ratio of each diffraction order. Subsequently, optimization procedures as outlined in Figure 3.10 are followed, resulting in the final parameters of these metagrating supercells provided in Table 3.4.

Table 3.4. Parameters of the supercell of the zero metagratings for multi-beam manipulation

Data types \ Parameters		A (mm)	h (mm)	d (mm)	w_1 (mm)	w_2 (mm)
Beam splitting I	FOV	13.05	1.88	4.36	1.54	0.94
Beam splitting II	FOV	10.64	1.99	4.51	1.96	0.60
Beam splitting III	FOV	13.05	2.12	4.60	1.77	0.72

FOV: final optimized value.

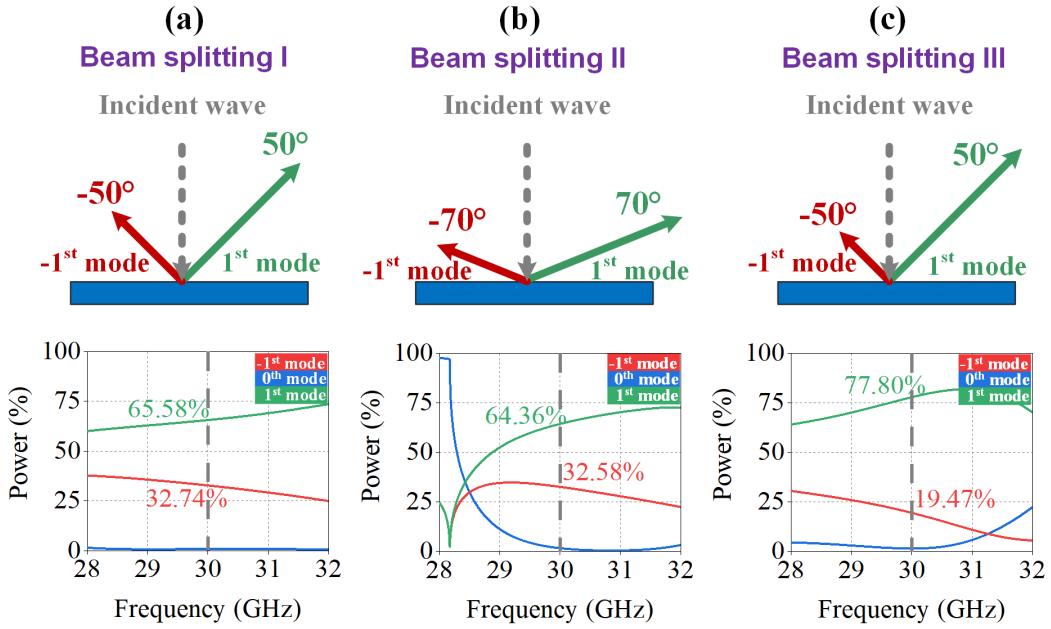

Figure 3.12: Beam manipulation scheme and simulation results of the supercell for different dual-beam splitting: (a) Beam splitting I, (b) Beam splitting II, (c) Beam splitting III.

The simulated performances of the corresponding supercells are illustrated in Figure 3.12(a)-(c). Analysis of the simulation results reveals alignment between the power ratios of the split beams and theoretical predictions. For all designs, apart from inevitable dielectric and

Joule losses (beam splitting I: 0.82% due to dielectric losses and 0.14% due to Joule losses, beam splitting II: 1.42% due to dielectric losses and 0.24% due to Joule losses, beam splitting III: 1.27% due to dielectric losses and 0.24% due to Joule losses), less than 2% of the power is radiated in the direction of undesired diffraction modes (beam splitting I: 0.87%, beam splitting II: 1.66%, beam splitting III: 1.49%).

Compared with the results in Figure 3.6(a), it is observed that there is a slightly higher amount of power coupled into the unwanted specular reflection 0^{th} mode.

3.3.4 Experimental validation

To further validate the proposed designs, different prototypes have been fabricated using classical PCB techniques, as depicted in the photographs in Figure 3.13(a). The physical dimensions of the samples are as follows: Beam splitter I and Beam splitter III share dimensions of $20\Lambda_y$ = 261 mm (y direction) by 260 mm (x direction), while Beam splitter II measures $25\Lambda_y$ = 266 mm (y direction) by 260 mm (x direction).

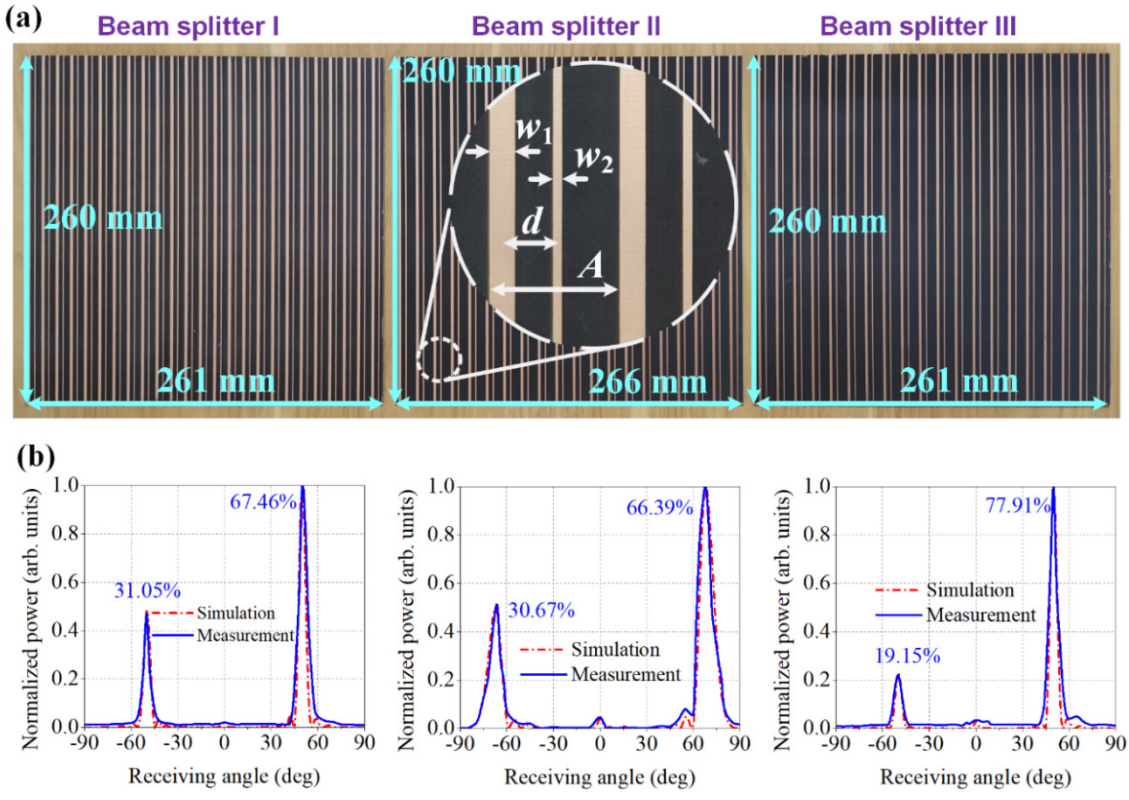

Figure 3.13: (a) Fabricated prototypes of beam splitters. (b) Normalized scattering power of the beam splitters (red dashed line is simulation result and blue solid line is measurement result)

The measurement setup, as illustrated in Figure 3.7(d) , is employed to assess the performance of the fabricated prototypes. Subsequently, the normalized scattered power is

calculated following Eq.(3.21) and presented in Figure 3.13(b). These plots demonstrate that the reflection angles of the beams align well with the predefined settings. Furthermore, a good correspondence of the power ratio is obtained with regard to the supercell simulation results.

The measured performances suggest that less than 5% of the scattered power is coupled to the specular reflection, thereby confirming the validity of the proposed metagrating beam splitters.

3.4 Perfect absorber based on metagratings

3.4.1 Analysis of metagrating for achieving perfect absorption

In Subsections 3.2 and 3.3, diverse wavefront manipulations have been effectively executed, encompassing anomalous reflection and beam splitting, through the orchestrated modulation of distinct diffraction orders within the metagrating structure. It is a rational conjecture that if the propagation of all diffraction orders can be suppressed, the functionality of wave absorption can be realized. Therefore, this subsection is dedicated to the formulation of electromagnetic wave absorption utilizing a reflective metagrating.

The schematic of electromagnetic metagratings for designing wave absorption is depicted in Figure 3.14(a), and the supercell composing the metagrating is shown in Figure 3.14(b). In this scenario, the metagrating system (comprising the metagrating structure and the permittivity of the dielectric substrate) and the characteristics of the external excitation source remain consistent with those detailed in Subsection 3.2. However, a singular wire is present within each supercell, and the period length (Λ_y) is constrained to be less than one wavelength to ensure the existence of solely the zeroth-order propagating diffraction mode.

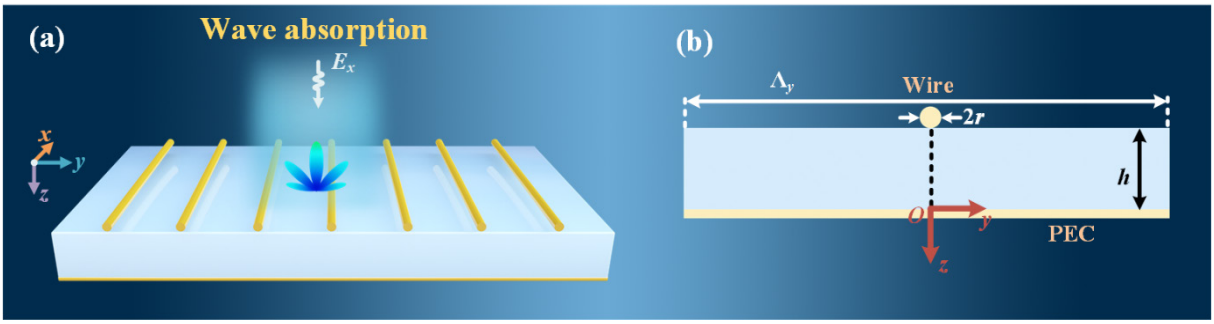

Figure 3.14: (a) Considered reflective metagrating and excitation source for realizing absorption. (b) Side view of the supercell composing the metagrating and its coordinate system for analysis.

Within such a metagrating system, the field amplitude of the mth diffraction mode E_m is formulated as follows

$$E_m = -\frac{k\eta}{2\Lambda_y}\left(\frac{1+\Gamma_m}{\beta_m}\right) I + \delta_{m0} E_{\text{in}} \Gamma = 0 \tag{3.23}$$

where Γ, Γ_m, and β_m are elucidated in Eqs. (2.31), (2.48) and (2.49), respectively.

Given that solely the 0th propagating diffraction mode exists herein, achieving wave absorption necessitates rendering $E_0 = 0$. We can then solve for the current I as

$$I = \frac{2\Lambda_y}{\eta} E_{\text{in}} \left(\frac{\Gamma}{1+\Gamma}\right) \tag{3.24}$$

Furthermore, the total field at the surface of the metagrating ($z = -h$) is expressed as

$$E^{\text{tot}} = E_{\text{in}}(1+\Gamma) - IZ(y, z+h) \tag{3.25}$$

where the defined function $Z(y,z)$ is defined in Eq. (2.54). By integrating Ohm's law $Z = E^{\text{tot}}/I$, the closed-form load impedance density Z required for achieving optimal wave absorption can be derived as

$$Z = -\frac{\eta}{2\Lambda_y} T_0 + \frac{\eta}{2\Lambda_y} |T_0|^2 - j\frac{k\eta}{2\pi}\left[\ln\left(\frac{\Lambda_y}{2\pi r}\right) + \sum_{m=1}^{\infty}\left(\frac{2\pi T_m}{\Lambda_y \alpha_m} - \frac{1}{m}\right)\right] \tag{3.26}$$

where T_0 can be obtained from Eq.(3.10).

Upon further analysis and a series of algebraic simplifications, the real and imaginary parts of the load impedance density Z are expressed as

$$\Re(Z) = \frac{\eta}{\Lambda_y}\frac{\tan^2(k_s h)}{\tan^2(k_s h)+\varepsilon_r} \tag{3.27}$$

$$\Im(Z) = -\frac{\eta}{\Lambda_y}\left[\frac{\sqrt{\varepsilon_r}\tan(k_s h)}{\tan^2(k_s h)+\varepsilon_r} + \frac{\Lambda_y}{\lambda}\ln\left(\frac{\Lambda_y}{2\pi r}\right) + \sum_{m=1}^{\infty}\left(\frac{kT_m}{\alpha_m} - \frac{1}{m}\right)\right] \tag{3.28}$$

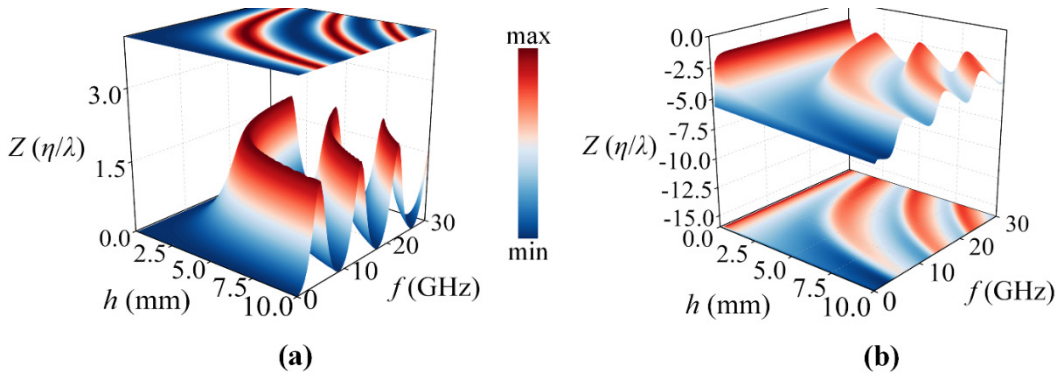

Figure 3.15: Metagrating load impedance density for realizing absorption under different frequency f and substrate height h with wire radius $r = 0.05$ mm: (a) Real part, (b) Imaginary part.

By employing Eqs.(3.27) and (3.28), the variations in the real and imaginary components of the impedance density for the metagrating across different frequencies (f) and substrate heights (h) can be graphically represented, as illustrated in Figure 3.15. Here, the radius of the wire is arbitrarily set to $r = 0.05$ mm. Analysis of Figure 3.15 reveals that the real part of the impedance

density can be effectively nullified by adjusting the substrate's height at specific frequencies. However, achieving a zero imaginary part of the impedance density proves to be challenging with a wire radius of r = 0.05 mm. The attainment of a zero imaginary part is only feasible for certain wire radii, a topic that will be elaborated upon in subsequent discussions.

3.4.2 Design of the Supercell

To validate the proposed methodology for designing the metagrating perfect absorber, I constructed the supercell of the metagrating and simulated it using HFSS simulation software. The selected operating frequency is f = 20 GHz, and the substrate material is F_4BM300 (ε_s = $3\varepsilon_0$ and tan δ = 0.0007). Before proceeding, the meta-atom needs to be designed based on the required load impedance density values obtained from Eqs.(3.27) and (3.28). Here, the meta-atom is categorized into four types based on their load impedance characteristics: A) $\Re(Z) \neq 0$ and $\Im(Z) \neq 0$; B) $\Re(Z) = 0$ and $\Im(Z) \neq 0$; C) $\Re(Z) \neq 0$ and $\Im(Z) = 0$; D) $\Re(Z) = 0$ and $\Im(Z) = 0$. The period length of the meta-atom along the x-axis direction is set to Λ_x = $\lambda/10$ = 1.5 mm to ensure load impedance distribution uniformity. Subsequently, the design of one meta-atom-based supercell for each type will be presented.

For the supercell with $\Re(Z) \neq 0$ and $\Im(Z) \neq 0$, there is no specific constraint on the choice of parameters based on Eqs. (3.27) and (3.28). The primary consideration is to avoid negative values for $\Re(Z)$. To design low-profile and sparse metagratings, the substrate thickness of $h = \lambda/15$ = 1 mm and the period length along y-axis direction of $\Lambda_y = 2\lambda/3$ = 10 mm are chosen, respectively. The calculated real part of the impedance density is $\Re(Z)$ = $0.3116\eta/\lambda$, and the imaginary part is $\Im(Z)$ = $-3.9744\eta/\lambda$. To achieve such a load impedance density, we consider a chip resistor in series with a microstrip capacitor. The meta-atom structure is depicted in Figure 3.16(a), where the width of the microstrip line for the capacitor is $w = 4r$ = 0.2 mm for the PCB fabrication [48], and the thickness of the copper trace is t = 0.018 mm.

Next, the supercell is constructed, and its top view is depicted in Figure 3.16(b). The length (L) of the microstrip capacitor is determined to achieve the required imaginary part of the impedance density $\Im(Z)$ using Eq.(3.20). The resistance value R is obtained based on the real part of the impedance density $\Re(Z)$ as

$$R = \Re(Z)\Lambda_x \tag{3.29}$$

Finally, the calculated values for the required resistance of the chip resistor and the length of the microstrip capacitor are R = 11.75 Ω and L = 3.00 mm.

For the supercell with $\Re(Z) = 0$ and $\Im(Z) \neq 0$, the substrate thickness h should satisfy Eq.(3.27) to ensure $\Re(Z) = 0$. The value of h is given by

$$h = \frac{n\pi}{k_s} = \frac{n\lambda}{2\sqrt{\varepsilon_r}}, (n = 1, 2, 3 \ldots) \tag{3.30}$$

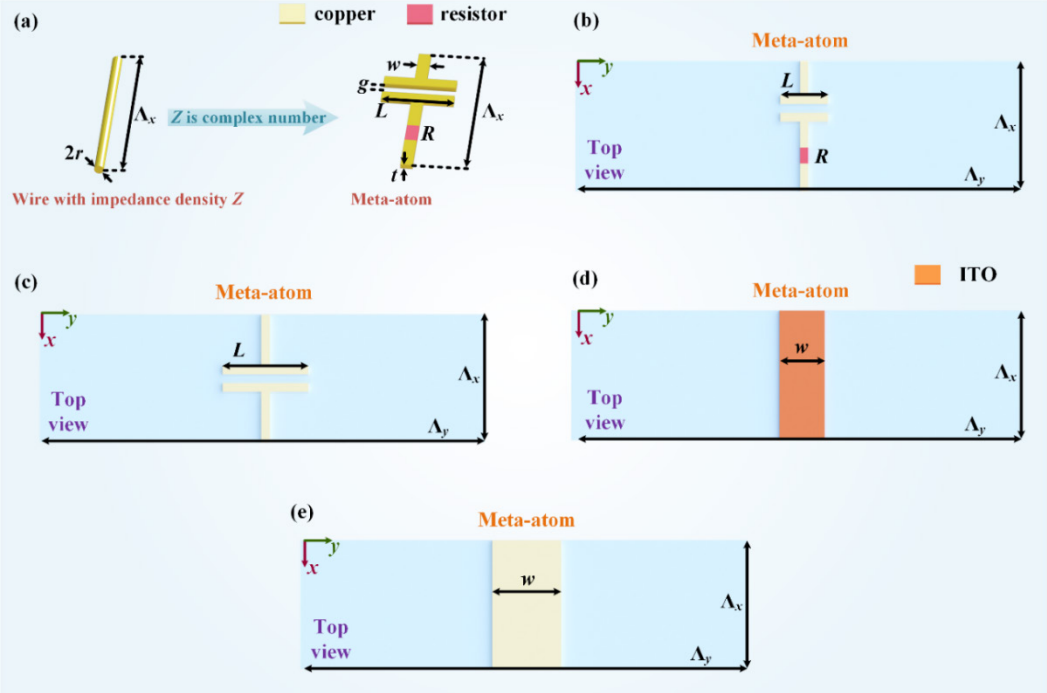

Figure 3.16: (a) Realization of a meta-atom with complex number load impedance density using a microstrip capacitor in series with a chip resistor. (b) Top view of the metagrating absorber supercell with $\Re(Z) \neq 0$ and $\Im(Z) \neq 0$. (c) Top view of the metagrating absorber supercell with $\Re(Z) = 0$ and $\Im(Z) \neq 0$. (d) Top view of the metagrating perfect absorber supercell with $\Re(Z) \neq 0$ and $\Im(Z) = 0$. (e) Top view of the metagrating perfect absorber supercell with $\Re(Z) = 0$ and $\Im(Z) = 0$.

To maintain a low profile, a value of $n = 1$ is chosen in Eq.(3.30), resulting in a substrate's thickness h = 4.33 mm. Simultaneously, for sparsity considerations, the period length Λ_y is selected as $\Lambda_y = 2\lambda/3 = 10$ mm. Subsequently, the imaginary impedance density can be computed as $\Im(Z) = -3.9744\eta/\lambda$. The meta-atom model incorporating a microstrip capacitor, as depicted in Figure 3.2(a), is employed to achieve the specified load impedance density. The top view of the supercell is presented in Figure 3.16(c). The required length of the capacitor can then be determined as L = 2.28 mm using Eq.(3.20).

For the supercell with $\Re(Z) \neq 0$ and $\Im(Z) = 0$, as per Eq.(3.28), to ensure $\Im(Z) = 0$, the wire radius r should satisfy

$$r = \frac{\Lambda_y}{2\pi} \exp\left[\frac{\lambda}{\Lambda_y} \frac{\sqrt{\varepsilon_r}\tan(kh\sqrt{\varepsilon_r})}{\tan^2(kh\sqrt{\varepsilon_r}) + \varepsilon_r} + \sum_{m=1}^{\infty}\left(\frac{2\pi T_m}{\Lambda_y \alpha_m} - \frac{1}{m}\right)\right] \tag{3.31}$$

Considering practical implementation, the ITO (indium-tin-oxide) film is employed to achieve the required load impedance density. The thickness of the ITO film is denoted as t =

0.175 mm, and the width of the ITO film is denoted as $w = 4r$ [48], which is written as

$$w = \frac{2\Lambda_y}{\pi} \exp\left[\frac{\lambda}{\Lambda_y} \frac{\sqrt{\varepsilon_r}\tan(kh\sqrt{\varepsilon_r})}{\tan^2(kh\sqrt{\varepsilon_r})+\varepsilon_r} + \sum_{m=1}^{\infty}\left(\frac{2\pi T_m}{\Lambda_y \alpha_m} - \frac{1}{m}\right)\right] \tag{3.32}$$

Subsequently, the top view of the constructed supercell is illustrated in Figure 3.16(d). It is crucial to note that while there is no restriction on the choice of the substrate thickness (h) and the period length (Λ_y), it can be observed from Eq.(3.32) that these values will determine the value of w. Improper values of h and Λ_y may lead to w being greater than Λ_y, rendering it impractical. Finally, after careful consideration, the substrate thickness and period length are set as $h = \lambda/8 = 2.5$ mm and $\Lambda_y = \lambda/3 = 5$ mm. Subsequently, the width of the meta-atom is calculated as $w = 1.25$ mm and the corresponding real part of the load impedance density is given as $\Re(Z) = 2.5330\ \eta/\lambda$. To realize such a load impedance density, the unit sheet resistance (Z_s) of the ITO film should follow

$$Z_s = \Re(Z)w \tag{3.33}$$

Finally, the calculated ITO film unit sheet resistance is $Z_s = 79.64\ \Omega$/sq.

For the supercell with $\Re(Z) = 0$ and $\Im(Z) = 0$, the meta-atom model with microstrip line depicted in Figure 3.2(a) is utilized to realize zero load impedance. The resulting top view of the built supercell is illustrated in Figure 3.16(e).

In the supercell, the substrate's thickness h, is determined through the condition $\Re(Z) = 0$ as per Eq.(3.27), while the strip width, denoted by w, of the meta-atom is calculated under the condition $\Im(Z) = 0$ using Eq.(3.28). A thoughtful selection of the period length Λ_y is also essential to ensure that the width w of the meta-atom remains less than Λ_y. Consequently, we opt for $\Lambda_y = \lambda/3 = 5$ mm. The calculated values for substrate thickness and meta-atom width are $h = 4.33$ mm and $w = 3.74$ mm, respectively.

3.4.3 Simulations and experiments

To validate the accuracy and reliability of the proposed theoretical analysis and design, the four types of supercells from Subsection 3.4.2 are arranged periodically in HFSS to simulate a finite-size structure, with dimensions of 300 mm along the x-direction and 300 mm along the y-direction.

Given that the designs are based on a rigorous analytical solution, the final correction involves multiplying the calculated parameters by a correction factor K, obtained by sweeping the corresponding parameters in the simulation to find the optimal absorption, as detailed in Table 3.5. This adjustment is necessary because the theoretical analysis relies on an ideal model, leading to slight deviations between the full-wave simulated performances and the theoretical

predictions. Several factors contribute to these discrepancies. The inherent resistance of copper parts in the meta-atom influences the real part of the load impedance density, and gaps at component connections in the microstrip lines impact the imaginary part of the impedance density. Consequently, some necessary parameter corrections are applied to the supercells.

Table 3.5. Parameters of the four types of metagrating supercell

Parameters \ Data types		Calculated value	**Optimal value**	Correction factor K
Type A	L (mm)	3.0	**2.46**	0.820
	R (Ω)	11.75	**7.00**	0.596
Type B	L (mm)	2.28	**2.09**	0.916
	h (mm)	4.33	**4.02**	0.927
Type C	w (mm)	1.25	**1.25**	1
	Z_s (Ω/sq)	79.64	**79.64**	1
Type D	w (mm)	3.74	**3.51**	0.940
	h (mm)	4.33	**4.24**	0.978

Type A: $\Re(Z) \neq 0$, $\Im(Z) \neq 0$; Type B: $\Re(Z) = 0$, $\Im(Z) \neq 0$;
Type C: $\Re(Z) \neq 0$, $\Im(Z) = 0$; Type D: $\Re(Z) = 0$, $\Im(Z) = 0$.

Furthermore, experimental validation of the aforementioned designs is conducted. Prototypes for all four types of absorbers are fabricated using PCB techniques, and sample photographs are presented in Figure 3.17 (a), (c), (e) and (g). The simulation and measurement results are presented in Figure 3.17 (b), (d), (f) and (h). The absorbance $A(\omega)$ is defined as $A(\omega) = 1 - \Gamma(\omega) - T(\omega)$, where $\Gamma(\omega) = |S_{11}|^2$ and $T(\omega) = |S_{21}|^2$ represent the reflection coefficient and transmission coefficient, respectively. Given that the backplane of the metagrating absorbers is fully copper-cladded, electromagnetic waves cannot be transmitted, *i.e.*, $T(\omega) = 0$. Consequently, the absorbance expression is simplified as

$$A(\omega) = 1 - \Gamma(\omega) = 1 - |S_{11}|^2 \tag{3.34}$$

The simulation and measurement results exhibit good agreement, revealing distinct absorbing bandwidths for the metagrating perfect absorber, characterized by three different outcomes. The first type demonstrates a narrowband absorption bandwidth, observed in cases where the real part of the load impedance is zero, with the imaginary parts being either zero or non-zero. The second type encompasses a conventional absorbing bandwidth, where neither the real part nor the imaginary part of the metagrating load impedance is zero. The third type represents a broadband absorption bandwidth, with a non-zero real part and a zero imaginary part of the metagrating load impedance. The fractional bandwidths (absorption rate greater than 90%) for these types are 4.9%, 0.1%, 42.9%, and 0.1%, corresponding to supercells Type A,

Type B, Type C, and Type D, respectively. Consequently, we can deduce that the absorbing bandwidth of a metagrating absorber is primarily influenced by the real part of its load impedance density. Moreover, the metagrating with a bigger load impedance density will result in a broader absorption bandwidth.

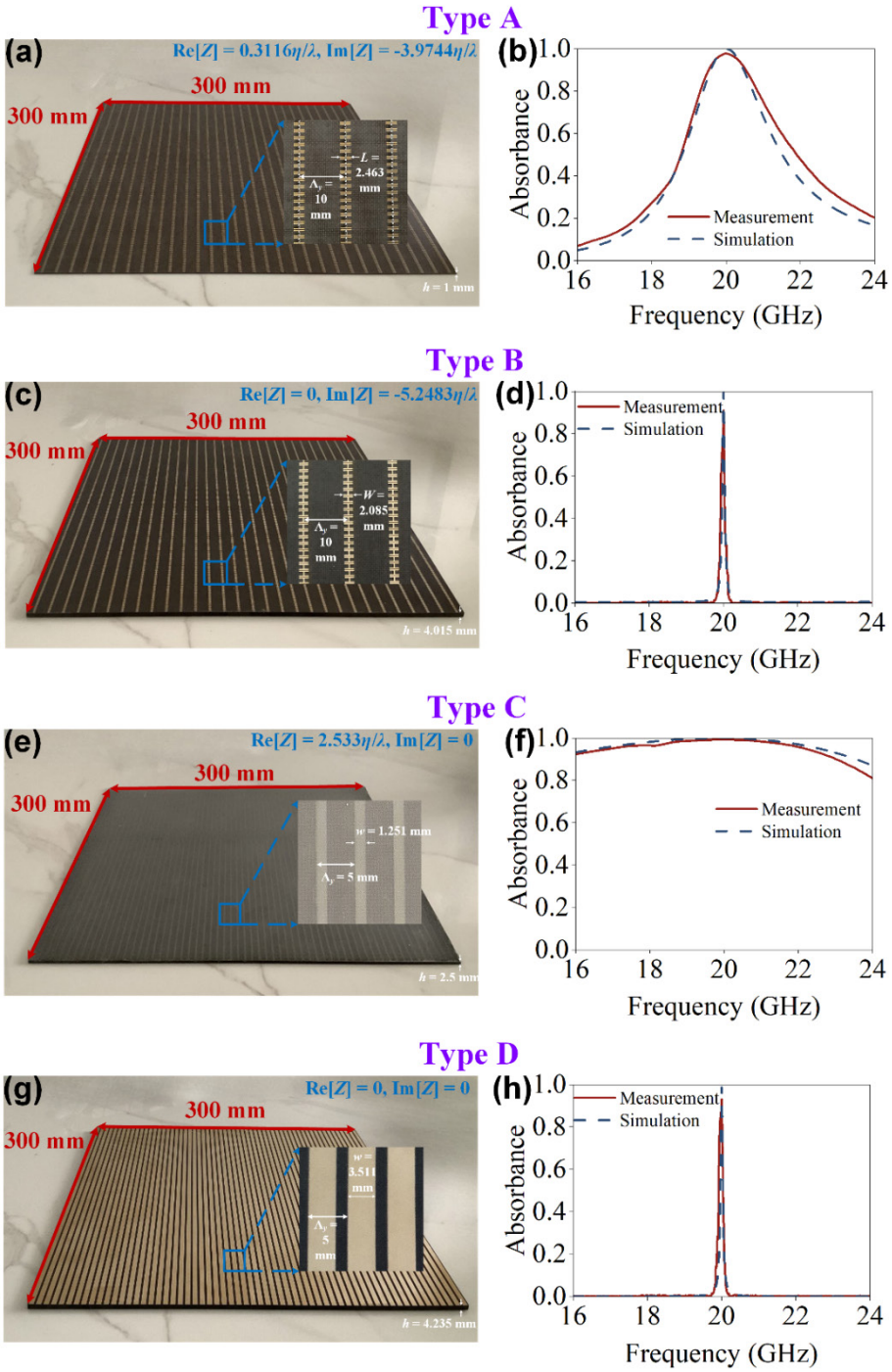

Figure 3.17: Fabricated metagrating prototypes and their simulation and measurement results. (a) and (b) Type A with $\Re(Z) = 0.3116\eta/\lambda$ and $\Im(Z) = -3.9744\eta/\lambda$. (c) and (d) Type B with $\Re(Z) = 0$ and $\Im(Z) = -5.2483\eta/\lambda$. (e) and (f) Type C with $\Re(Z) = 2.533\eta/\lambda$ and $\Im(Z) = 0$. (g) and (h) Type D with $\Re(Z) = 0$ and $\Im(Z) = 0$.

Hence, an investigation of the maximum absorption bandwidth is proposed. According to Eq.(3.29), the real part of the impedance density is solely determined by Λ_y, h and ε_r. Thus when the parameters Λ_y and ε_r are determined at the beginning, only the height h has an influence on the impedance density, as shown in Figure 3.18(a). Notably, for $k_s h = (n + 1/2)\pi$ ($n = 0, 1, 2, 3\ldots$), the real part of the impedance density reaches its maximum value. By selecting $n = 0$, substrate's thickness $h = 2.17$ mm can be calculated, and the corresponding meta-atom parameters can be calculated using Eqs.(3.32) and (3.33) as $w = 3.69$ mm and $Z_s = 278.17$ Ω/sq (the parameter values are given in Table 3.6). The corresponding simulation result is presented in Figure 3.18(b), showcasing a fractional bandwidth of 47.8%. Given the initially chosen Λ_y value of 5 mm, a further exploration is conducted to investigate how the fractional bandwidth changes with different Λ_y values. The parameters for each meta-atom are calculated for Λ_y = 7.5 mm and Λ_y = 3.75 mm, as detailed in Table 3.6, and the corresponding supercell structures are simulated. The results, presented in Figure 3.18(c), demonstrate minimal impact on the final absorption bandwidth when Λ_y takes different values, with fractional bandwidths of 47.7% and 47.3%, respectively. In conclusion, the minimum and maximum absorption bandwidths of the metagrating absorber around the center frequency of 20 GHz are 0.1% and 47.8%, respectively. According to a study conducted in [49], a broader bandwidth might be achievable by incorporating multiple meta-atoms with slightly different operating frequencies within a single supercell. Further evaluation of the device's performance is conducted through the determination of a figure of merit (FOM) at -10 dB, defined as the ratio of Rozanov's thickness to the thickness of the metagrating [49]:

$$\mathrm{FOM} = \frac{\ln(10)}{40\pi^2}\frac{|(1-A)_{\mathrm{dB}}|\Delta\lambda}{h} \tag{3.35}$$

where $\Delta\lambda$ represents the difference between the minimum and maximum wavelengths for which $(1 - A)_{\mathrm{dB}}$ is less than -10 dB.

The FOM extracted from experimental data of these metagrating absorbers are calculated as Type A: 0.091, Type B: 0.001, Type C: 0.371, and Type D: 0.001, respectively. The meta-atom structure used for the metagrating absorber in [49] is of Type A here, and the FOM value of Type A metagrating absorber here is larger for the presence of only one meta-atom per supercell in [49], but smaller than the FOM value [49] for the presence of two meta-atoms per supercell. Interestingly, the FOM value of the Type C metagrating absorber here is as high as 0.371, which could not be achieved even by increasing the number of meta-atoms per supercell in [49], and this further indicates that the Type C metagrating absorber has a wide range of applications in broadband wave absorption.

Table 3.6. Values of each supercell parameters when the real part of the impedance density reaches its maximum value

	h (mm)	Λ_x (mm)	w (mm)	Z_s (Ω/sq)
Λ_y = 7.5mm	2.165	1.5	6.677	335.628
Λ_y = 5mm	2.165	1.5	3.689	278.173
Λ_y = 3.75mm	2.165	1.5	2.589	260.274

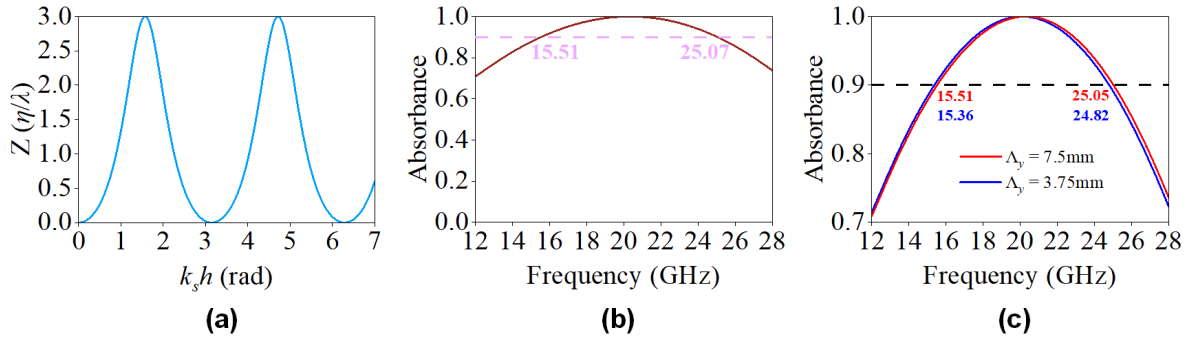

Figure 3.18: (a) Trend of the real part of the impedance with a change of $k_s h$ for Λ_y = 5 mm and frequency f = 20 GHz. (b) Simulation result of the metagrating absorber for Λ_y = 5 mm and h = 2.17 mm. (c) Simulation results of the widest bandwidth when Λ_y = 7.5 mm and Λ_y = 3.75 mm.

Additionally, the angular independence of the metagrating absorber is further discussed. Prior to studying absorption performance under oblique incidence, designing metagrating absorbers for non-normal incidence is assumed in the theoretical considerations. Assuming the oblique incidence angle as θ_{in}, the period Λ_y must satisfy the condition $\Lambda_y < \lambda/(1 + \sin|\theta_{\text{in}}|)$. Consequently, the previously designed Type A and Type B supercells should operate in the angular range of -30° to 30°, ensuring only the 0^{th} diffraction mode. For Type C and Type D supercells, the operating angular range spans from -90° to 90°.

Although the required load impedance density of the meta-atoms varies with different incidence angles, for the purpose of investigating incidence sensitivity, the supercells with impedance density designed for 0° incidence are employed to perform simulations under oblique incidence. Simulation results indicate that the Type C structure exhibits the best angular insensitivity performance, attaining more than 90% absorption over the range of -50° to +50°, as presented in Figure 3.19(c) (Note: to enhance clarity, the vertical coordinate of Figure 3.19(c) ranges from 0.6 to 1). The second-best angular insensitivity performance is observed for the Type A structure, sustaining more than 90% absorption for the incidence range from -30° to 30°, as shown in Figure 3.19(a). In contrast, both Type B and Type D structures display angle

sensitivity. For Type B, the absorption frequency decreases as the incidence angle increases, accompanied by a decrease in absorption level and an undesired absorption peak at higher frequencies near 23 GHz, as depicted in Figure 3.19(b). Meanwhile, for Type D structure, the absorption frequency increases as the angle of incidence rises, while the absorption level remains almost constant, as shown in Figure 3.19(d).

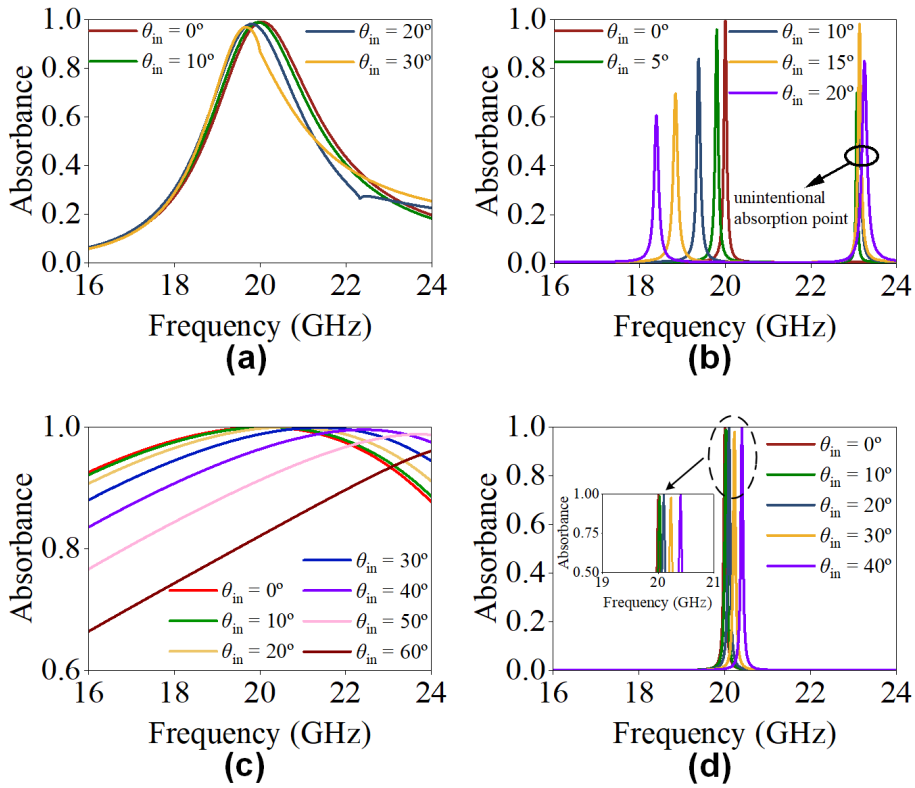

Figure 3.19: Absorbance of metagrating perfect absorber with different supercells under different incident angles: (a) Type A, (b) Type B, (c) Type C, and (d) Type D.

Finally, it is worth noting that the design methodology of metagrating absorbers is applicable to any frequency. This study randomly selects a design frequency of 20 GHz. It is important to emphasize that although the thickness *h* of supercells Type A and Type C can be freely chosen, a careful tradeoff must be made between this thickness and the absorption level. When *h* takes on very small values, the real part of the impedance is also relatively small, potentially hindering the metagrating from achieving the desired wave absorption effect. Furthermore, at the selected design frequency, the absorption bandwidth coverage, ranging from narrowband to wideband, can be achieved by selecting different types of supercell. Therefore, whether considering the absorption frequency or absorption bandwidth, the metagrating absorber demonstrates a high degree of flexibility.

3.5 Conclusion

In this chapter, I have undertaken various wavefront manipulation designs utilizing reflective metagratings. These designs encompass anomalous reflection, beam splitting, and wave absorption. All methodologies proposed herein are firmly grounded in fully analytical design frameworks, rendering them applicable across microwave, millimeter-wave, and terahertz frequency bands. These analytically derived formulations establish a robust theoretical framework for realizing diverse wavefront manipulations using reflective metagratings.

Furthermore, this chapter introduces the innovative concept of zero load-impedance metagratings. Unlike conventional metagratings, zero load-impedance metagratings can be constructed using simple microstrip line structures, substantially easing the precision requirements in PCB processing at high-frequency bands. This advancement extends the feasible frequency range for metagratings.

Moreover, the study presented in this chapter not only investigates and implements wave absorption using reflective metagratings but also delves into the design of meta-atom structures with varying load impedance densities. This exploration yields insights into the correlation between absorption bandwidth and meta-atom structure, thereby offering flexibility in design options tailored to specific narrowband or broadband wave absorption requirements.

In comparison to existing literature on wavefront manipulation employing reflective metagratings, the designs for anomalous reflection and beam splitting presented herein utilize a more intuitive, fully analytical design approach. Additionally, the realization of wave absorption and zero load-impedance metagratings for wavefront manipulation marks a pioneering contribution in this chapter.

Most designs elucidated in this chapter undergo rigorous experimental validation to ascertain their efficacy and accuracy. The close agreement observed between experimental results and theoretical predictions underscores the significant potential of wavefront manipulation designs based on reflective metagratings for applications in future wireless communications, radar detection, electromagnetic stealth, and other communication-related functionalities.

Chapter 4
Transmissive metagratings for wavefront manipulation

Contents

4.1 Introduction

Chapter 3 presented a thorough investigation and application of reflective metagratings for wavefront manipulation. While reflective metagratings exhibit robust capabilities in manipulating wavefronts, the presence of the bottom ground plane restricts diffraction in the lower half-space, thereby limiting the potential for extensive wavefront manipulation. In this chapter, a specific wavefront manipulation design based on transmissive metagratings will be conducted.

To date, researchers have conducted various wavefront manipulation designs using transmissive metagratings, encompassing anomalous refraction under oblique incidence, beam focusing [35], retro reflection [36], anomalous refraction, anomalous reflection and beam splitting [34]. These wavefront manipulation techniques using transmissive metagratings offer similar advantages in high efficiency of extreme-angle beam manipulation and feature sparse and simple structures, akin to reflective metagratings.

This chapter will also entail the design of anomalous refraction, anomalous reflection, and beam splitting based on transmissive metagratings. Unlike prior works, these designs will be rooted in fully analytical methodologies, rendering the design process more intuitive and obviating the need for numerical optimization. Additionally, an investigation into uni- and bi-directional wave absorption based on transmissive metagratings will be conducted. Lastly, an exploration of metagratings will reveal distinct wavefront manipulation functions for different directions of incidence, suggesting the feasibility of designing Janus metagratings.

4.2 Highly efficient anomalous refraction, anomalous reflection and beam splitting

4.2.1 Theoretical analysis and calculations

The schematic representation of the transmissive metagrating under consideration for achieving highly efficient wavefront manipulation is illustrated in Figure 4.1(a). It is illuminated by a TE-polarized $(E_y = E_z = H_x = 0)$ electromagnetic wave. The considered metagrating is a two-dimensional structure, which is invariant along the x-direction and exhibits a periodic alignment in the y-direction. The distance between the upper and lower surfaces along the z-direction is h. The side view of the supercell (period with length Λ_y) composing the metagrating with the established coordinate system is shown in Figure 4.1(b). The supercell

contains five wires with radius r, three of which are located on the upper layer of the dielectric substrate and two on the lower layer, and their constellation are $(y_1, z_1) = (-d_1, h)$, $(y_2, z_2) = (0, h)$, $(y_3, z_3) = (d_2, h)$, $(y_4, z_4) = (-d_3, 0)$ and $(y_5, z_5) = (d_4, 0)$, respectively. The structure is considered as a groundless metagrating with air occupying the space above ($z < -h$) and below ($z > 0$). The permittivity values of air and dielectric substrate are denoted by ε_0 (ε_0 is the permittivity of vacuum) and $\varepsilon_s = \varepsilon_r\varepsilon_0$ (ε_r is the relative permittivity of the substrate), respectively. Given that both air and dielectric substrate are non-magnetic media, the wave numbers and wave impedances in these media are expressed as $k_0 = \omega\sqrt{\mu_0\varepsilon_0}$, $\eta_0 = \sqrt{\mu_0/\varepsilon_0}$, $k_s = \omega\sqrt{\mu_0\varepsilon_s}$, and $\eta_s = \sqrt{\mu_0/\varepsilon_s}$, respectively , where μ_0 denotes the permeability of vacuum.

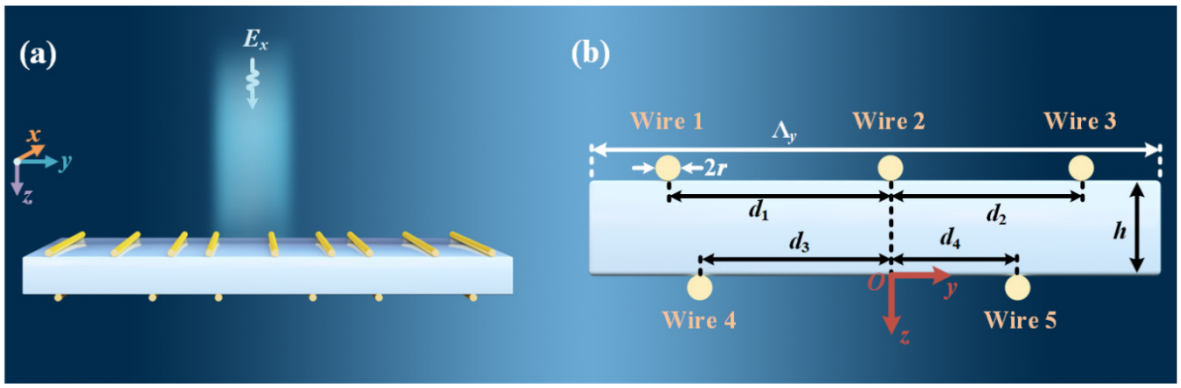

Figure 4.1: (a) Considered transmissive metagrating and excitation source. (b) Side view of the supercell composing the metagrating.

Referring to Figure 4.1(a), the electric field of the incident TE-polarized plane wave is represented as $E^{\text{in}} = E_{\text{in}}e^{-jk_0(z+h)}$ ($E_z = E_y = H_x = 0$). Subsequently, the amplitudes of the m^{th} order diffraction modes of reflection E_m^u and transmission E_m^l, respectively, can be denoted as

$$E_m^u = -k_0\left(\frac{1+\Gamma_m}{\beta_m}\zeta_m^u + \frac{T_m}{\beta_m}\zeta_m^l\right) + \delta_{m0}E_{\text{in}}\Gamma \tag{4.1}$$

$$E_m^l = -k_0\left(\frac{1+\Gamma_m}{\beta_m}\zeta_m^l + \frac{T_m}{\beta_m}\zeta_m^u\right) + \delta_{m0}E_{\text{in}}T \tag{4.2}$$

with

$$\zeta_m^u = \frac{\eta_0}{2\Lambda_y}\left(I_1^u e^{-j\xi_m d_1} + I_2^u + I_3^u e^{j\xi_m d_2}\right) \tag{4.3}$$

$$\zeta_m^l = \frac{\eta_0}{2\Lambda_y}\left(I_1^l e^{-j\xi_m d_3} + I_2^l e^{j\xi_m d_4}\right) \tag{4.4}$$

where $\alpha_m = \frac{2\pi m}{\Lambda_y}$ and $\beta_m = \sqrt{k_0^2 - \xi_m^2}$ represent the transverse and longitudinal wave numbers of the m^{th} order Floquet mode in air, respectively. Here, I_1^u, I_2^u and I_3^u denote the line currents on the upper wires, while I_1^l and I_2^l represent the currents on the lower wires of

the supercell. Additionally, Γ, T, Γ_m and T_m are expressed in Eqs. (2.36), (2.37), (2.63) and (2.64) respectively.

Based on the analysis in subsection 2.5.2, the period length of the metagrating is selected as $\lambda_0 < \Lambda_y < 2\lambda_0$, resulting in the emergence of six diffraction modes by the transmissive metagratings, comprising three reflection modes and three transmission modes. In the case of these propagating diffraction modes, adherence to Eq. (2.67) is crucial to maintain the power ratio for each diffraction mode. In accordance with Eq. (2.67), the amplitude of the m^{th} order propagating diffraction modes can also be expressed as

$$E_m^u = e^{j\varphi_m^u} E_{\text{in}} \sqrt{P_m^u \beta_0/\beta_m} = a_m(\beta_0/\beta_m) \tag{4.5}$$

$$E_m^l = e^{j\varphi_m^l} E_{\text{in}} \sqrt{P_m^l \beta_0/\beta_m} = b_m(\beta_0/\beta_m) \tag{4.6}$$

where

$$a_m = e^{j\varphi_m^u} \sqrt{P_m^u \beta_m/\beta_0} \tag{4.7}$$

$$b_m = e^{j\varphi_m^l} \sqrt{P_m^l \beta_m/\beta_0} \tag{4.8}$$

Thus, by combining Eqs.(4.1), (4.2), (4.5) and (4.6), the following expression can be derived

$$-\frac{\eta_0}{2\Lambda_y}\left[(1+\Gamma_m)\left(I_1^u e^{-j\xi_m d_1} + I_2^u + I_3^u e^{j\xi_m d_2}\right) + T_m\left(I_1^l e^{-j\xi_m d_3} + I_2^l e^{j\xi_m d_4}\right)\right] + \delta_{m0} E_{\text{in}} \Gamma = E_{\text{in}} a_m \tag{4.9}$$

$$-\frac{\eta_0}{2\Lambda_y}\left[(1+\Gamma_m)\left(I_1^l e^{-j\xi_m d_3} + I_2^l e^{j\xi_m d_4}\right) + T_m\left(I_1^u e^{-j\xi_m d_1} + I_2^u + I_3^u e^{j\xi_m d_2}\right)\right] + \delta_{m0} E_{\text{in}} T = E_{\text{in}} b_m \tag{4.10}$$

When m takes values of -1, 0 and 1, the Eqs. (4.9) and (4.10) above can be expanded into six equations. These equations incorporate only five current parameters (I_1^u, I_2^u, I_3^u, I_1^l and I_2^l). Hence, when addressing the power ratio of each propagating diffraction mode and solving these equations, it is sufficient to arbitrarily choose only five of them for the solution. The practicality of this method underscores an inherent property of metagratings, wherein the control of five diffraction modes is equivalent to controlling the entirety of six diffraction modes.

Hence, in this context, the decision is made to select the -1$^{\text{st}}$, 0$^{\text{th}}$, and 1$^{\text{st}}$ reflection modes along with the -1$^{\text{st}}$ and 0$^{\text{th}}$ transmission modes, as the targeted modes for control. Therefore, the five equations encompassing Eq. (4.9) with m = -1, 0, 1 and Eq. (4.10) with m = -1, 0 are resolved to obtain the values of the five currents. Consequently, the currents on the upper face of the metagrating can be determined as

$$I_s^u = \frac{\Lambda_y}{\eta_0} E_{\text{in}} q_s \ (s = 1, 2, 3) \tag{4.11}$$

with

$$q_1 = \frac{2}{\left(e^{j\xi_1 d_1}-1\right)\left(e^{j\xi_1 d_2}-e^{-j\xi_1 d_1}\right)} \times \begin{Bmatrix} \frac{-(1+\Gamma_1)a_{-1}+T_1 b_{-1}}{(1+\Gamma_1)^2-T_1^2} e^{j\xi_1 d_2} - \left[1 - \frac{(1+\Gamma)(a_0+1)-Tb_0}{(1+\Gamma)^2-T^2}\right]\left(1+e^{j\xi_1 d_2}\right) - \frac{a_1}{1+\Gamma_1} \\ -\frac{T_1}{1+\Gamma_1}\left[\frac{(1+\Gamma_1)b_{-1}-T_1 a_{-1}}{(1+\Gamma_1)^2-T_1^2} e^{j\xi_1(d_4-d_3)} - \frac{(1+\Gamma)-Tb_0(a_0+1)}{(1+\Gamma)^2-T^2}\left(e^{-j\xi_1 d_3}+e^{j\xi_1 d_4}\right)\right] \end{Bmatrix} \tag{4-12}$$

$$q_2 = \frac{2}{\left(e^{j\xi_1 d_1}-1\right)\left(e^{j\xi_1 d_2}-1\right)} \times \begin{Bmatrix} \frac{(1+\Gamma_1)a_{-1}-T_1 b_{-1}}{(1+\Gamma_1)^2-T_1^2} e^{j\xi_1 d_2} + \left[1 - \frac{(1+\Gamma)(a_0+1)-Tb_0}{(1+\Gamma)^2-T^2}\right]\left(1+e^{j\xi_1(d_1+d_2)}\right) - \frac{a_1 e^{j\xi_1 d_1}}{1+\Gamma_1} \\ -\frac{T_1 e^{j\xi_1 d_1}}{1+\Gamma_1}\left[\frac{(1+\Gamma_1)b_{-1}-T_1 a_{-1}}{(1+\Gamma_1)^2-T_1^2} e^{j\xi_1(d_4-d_3)} - \frac{(1+\Gamma)b_0-T(a_0+1)}{(1+\Gamma)^2-T^2}\left(e^{-j\xi_1 d_3}+e^{j\xi_1 d_4}\right)\right] \end{Bmatrix} \tag{4-13}$$

$$q_3 = \frac{2}{\left(e^{j\xi_1 d_2}-1\right)\left(e^{j\xi_1 d_1}-e^{-j\xi_1 d_2}\right)} \times \begin{Bmatrix} \frac{-(1+\Gamma_1)a_{-1}+T_1 b_{-1}}{(1+\Gamma_1)^2-T_1^2} - \left[1 - \frac{(1+\Gamma)(a_0+1)-Tb_0}{(1+\Gamma)^2-T^2}\right]\left(1+e^{j\xi_1 d_1}\right) - \frac{a_1 e^{j\xi_1 d_1}}{1+\Gamma_1} \\ -\frac{T_1 e^{j\xi_1 d_1}}{1+\Gamma_1}\left[\frac{(1+\Gamma_1)b_{-1}-T_1 a_{-1}}{(1+\Gamma_1)^2-T_1^2} e^{j\xi_1(d_4-d_3)} - \frac{(1+\Gamma)b_0-T(a_0+1)}{(1+\Gamma)^2-T^2}\left(e^{-j\xi_1 d_3}+e^{j\xi_1 d_4}\right)\right] \end{Bmatrix} \tag{4-14}$$

The currents on the lower face of the metagrating are deduced as follows

$$I_s^l = \frac{\Lambda_y}{\eta_0} E_{\text{in}} p_s \ (s = 1, 2) \tag{4.15}$$

with

$$p_1 = \frac{2}{e^{j\xi_1 d_3}-e^{-j\xi_1 d_4}}\left[\frac{-(1+\Gamma_1)b_{-1}+T_1 a_{-1}}{(1+\Gamma_1)^2-T_1^2} + \frac{(1+\Gamma)b_0-T(a_0+1)}{(1+\Gamma)^2-T^2} e^{-j\xi_1 d_4}\right] \tag{4.16}$$

$$p_2 = \frac{2}{e^{j\xi_1 d_3}-e^{-j\xi_1 d_4}}\left[\frac{(1+\Gamma_1)b_{-1}-T_1 a_{-1}}{(1+\Gamma_1)^2-T_1^2} - \frac{(1+\Gamma)b_0-T(a_0+1)}{(1+\Gamma)^2-T^2} e^{j\xi_1 d_3}\right] \tag{4.17}$$

Moreover, drawing upon the analysis in subsection 2.4.2, the total field in the upper half-space ($z \leq -h$) of the metagrating is expressed as

$$E^{\text{tot}} = E_{\text{in}} e^{-j\beta_0(z+h)} e^{-j\xi_0 y} + \sum_{m=-\infty}^{\infty} E_m^u e^{-j\xi_m y} e^{j\beta_m(z+h)} \tag{4.18}$$

The expression for the total field in the lower region ($z \geq 0$) of the metagrating is given by

$$E^{\text{tot}} = \sum_{m=-\infty}^{\infty} E_m^l e^{-j\xi_m y} e^{-j\beta_m z} \tag{4.19}$$

Subsequently, by combining Ohm's law $E^{\text{tot}} = ZI$, relational equations concerning the near field on both the upper and lower surfaces of the metagrating can be formulated. Specifically, on the upper face of the metagrating ($z = -h$), we have

$$\begin{bmatrix} Z_1^u I_1^u \\ Z_2^u I_2^u \\ Z_3^u I_3^u \end{bmatrix} = \begin{bmatrix} E_{\text{in}}(1+\Gamma) \\ E_{\text{in}}(1+\Gamma) \\ E_{\text{in}}(1+\Gamma) \end{bmatrix} - Q_{3\times 3}^{u(r)} \begin{bmatrix} I_1^u \\ I_2^u \\ I_3^u \end{bmatrix} - Q_{3\times 2}^{l(t)} \begin{bmatrix} I_1^l \\ I_2^l \end{bmatrix} \tag{4.20}$$

with

$$Q_{3\times 3}^{u(r)} = \begin{bmatrix} Z^r(0,0) & Z^r(d_1,0) & Z^r(d_1+d_2,0) \\ Z^r(d_1,0) & Z^r(0,0) & Z^r(d_2,0) \\ Z^r(d_1+d_2,0) & Z^r(d_2,0) & Z^r(0,0) \end{bmatrix} \tag{4.21}$$

$$Q_{3\times2}^{l(t)}=\begin{bmatrix}Z^t(d_1-d_3,0) & Z^t(d_1+d_4,0)\\ Z^t(d_3,0) & Z^t(d_4,0)\\ Z^t(d_2+d_3,0) & Z^t(d_2-d_4,0)\end{bmatrix} \tag{4.22}$$

where the two radiative impedance density functions, $Z^r(y,z)$ and $Z^t(y,z)$, are described in Eqs. (2.71) and (2.72), respectively.

Similarly, on the lower face of the metagrating ($z = 0$), we have

$$\begin{bmatrix}Z_1^l I_1^l\\ Z_2^l I_2^l\end{bmatrix}=\begin{bmatrix}E_{\text{in}}T\\ E_{\text{in}}T\end{bmatrix}-Q_{2\times2}^{l(r)}\begin{bmatrix}I_1^l\\ I_2^l\end{bmatrix}-Q_{2\times3}^{u(t)}\begin{bmatrix}I_1^u\\ I_2^u\\ I_3^u\end{bmatrix} \tag{4.23}$$

with

$$Q_{2\times2}^{l(r)}=\begin{bmatrix}Z^r(0,0) & Z^r(d_3+d_4,0)\\ Z^r(d_3+d_4,0) & Z^r(0,0)\end{bmatrix} \tag{4.24}$$

$$Q_{3\times3}^{u(r)}=\begin{bmatrix}Z^t(d_1-d_3,0) & Z^t(d_3,0) & Z^t(d_2+d_3,0)\\ Z^t(d_1+d_4,0) & Z^t(d_4,0) & Z^t(d_2-d_4,0)\end{bmatrix} \tag{4.25}$$

where Z_1^u, Z_2^u, Z_3^u, Z_1^l and Z_2^l represent the load impedance density of the five wires on the upper and lower faces of the metagrating.

Finally, by substituting the obtained analytical expressions of the polarization currents from Eqs.(4.11) and (4.15) into Eqs. (4.20) and (4.23) respectively, the closed-form analytical solutions of the wire load impedance density can be derived as

$$Z_1^u=\frac{\eta_0}{\Lambda_y}\frac{1+\Gamma}{q_1}-Z^r(0,0)-j\frac{k_0\eta_0}{2\Lambda_y}\sum_{m=-\infty}^{\infty}\left[\begin{matrix}\frac{1+\Gamma_m}{\alpha_m}\left(\frac{q_2}{q_1}+\frac{q_3}{q_1}e^{-j\xi_m d_2}\right)\\ +\frac{T_m}{\alpha_m}\left(\frac{p_1}{q_1}e^{j\xi_m d_3}+\frac{p_2}{q_1}e^{-j\xi_m d_4}\right)\end{matrix}\right]e^{-j\xi_m d_1} \tag{4-26}$$

$$Z_2^u=\frac{\eta_0}{\Lambda_y}\frac{1+\Gamma}{q_2}-Z^r(0,0)-j\frac{k_0\eta_0}{2\Lambda_y}\sum_{m=-\infty}^{\infty}\left[\begin{matrix}\frac{1+\Gamma_m}{\alpha_m}\left(\frac{q_1}{q_2}e^{-j\xi_m d_1}+\frac{q_3}{q_2}e^{-j\xi_m d_2}\right)\\ +\frac{T_m}{\alpha_m}\left(\frac{p_1}{q_2}e^{-j\xi_m d_3}+\frac{p_2}{q_2}e^{-j\xi_m d_4}\right)\end{matrix}\right] \tag{4-27}$$

$$Z_3^u=\frac{\eta_0}{\Lambda_y}\frac{1+\Gamma}{q_3}-Z^r(0,0)-j\frac{k_0\eta_0}{2\Lambda_y}\sum_{m=-\infty}^{\infty}\left[\begin{matrix}\frac{1+\Gamma_m}{\alpha_m}\left(\frac{q_1}{q_3}e^{-j\xi_m d_1}+\frac{q_2}{q_3}\right)+\\ \frac{T_m}{\alpha_m}\left(\frac{p_1}{q_3}e^{-j\xi_m d_3}+\frac{p_2}{q_3}e^{j\xi_m d_4}\right)\end{matrix}\right]e^{-j\xi_m d_2} \tag{4-28}$$

$$Z_1^l=\frac{\eta_0}{\Lambda_y}\frac{T}{p_1}-Z^r(0,0)-j\frac{k_0\eta_0}{2\Lambda_y}\sum_{m=-\infty}^{\infty}\left[\begin{matrix}\frac{1+\Gamma_m}{\alpha_m}\frac{p_2}{p_1}e^{-j\xi_m d_4}+\\ \frac{T_m}{\alpha_m}\left(\frac{q_1}{p_1}e^{j\xi_m d_1}+\frac{q_2}{p_1}+\frac{q_3}{p_1}e^{-j\xi_m d_2}\right)\end{matrix}\right]e^{-j\xi_m d_3} \tag{4-29}$$

$$Z_2^l=\frac{\eta_0}{\Lambda_y}\frac{T}{p_2}-Z^r(0,0)-j\frac{k_0\eta_0}{2\Lambda_y}\sum_{m=-\infty}^{\infty}\left[\begin{matrix}\frac{1+\Gamma_m}{\alpha_m}\frac{p_1}{p_2}e^{-j\xi_m d_3}+\\ \frac{T_m}{\alpha_m}\left(\frac{q_1}{p_2}e^{-j\xi_m d_1}+\frac{q_2}{p_2}+\frac{q_3}{p_2}e^{j\xi_m d_2}\right)\end{matrix}\right]e^{-j\xi_m d_4} \tag{4-30}$$

To account for passive and lossless metagratings, ensuring maximum efficiency, an additional constraint on the load impedance density is required, given by

$$\Re(Z_1^u)=0,\ \Re(Z_2^u)=0,\ \Re(Z_3^u)=0,\ \Re\left(Z_1^l\right)=0,\ \Re(Z_2^l)=0 \tag{4.31}$$

Finally, the design of various types of beam manipulation can be finalized by assigning values to parameters a_{-1}, a_0, a_1, b_{-1} and b_0. As evident from Eqs.(4.7) and (4.8), upon determining the distinct a_m and b_m, the corresponding diffraction powers P_m^u and P_m^l are established. Subsequently, four different wavefront manipulation scenarios are considered, namely, single-beam (anomalous reflection and anomalous refraction) as well as multibeam (same-side transmissive beam splitting and opposite-side beam splitting) wavefront manipulation.

For the anomalous refraction, the +1st transmission diffraction mode is designated as the radiated beam to achieve the desired effect. This implies that we have

$$a_{-1} = a_0 = a_1 = b_{-1} = b_0 = 0 \tag{4.32}$$

By solving the system of Eqs. (4.31) and (4.32), the constellation parameters of the meta-atoms, namely d_1, d_2, d_3, d_4 and h, can be computed. Subsequently, by substituting these parameters into the expressions for load impedance density of Eqs.(4.26)-(4.30), the corresponding impedance density values required for each meta-atom can be determined.

In the anomalous reflection design, the +1st reflection diffraction mode is chosen as the radiated beam. Consequently, it can be deduced that

$$a_{-1} = a_0 = b_{-1} = b_0 = 0, a_1 = e^{j\varphi_1^u}\sqrt{\beta_1/\beta_0} \tag{4.33}$$

Given the introduction of an additional unknown φ_1^u in Eq. (4.33), an extra equation $\left|e^{j\varphi_1^u}\right| - 1 = 0$ must be included when solving the system of Eqs. (4.31) and (4.33). This ensures that the number of unknowns d_1, d_2, d_3, d_4, h and φ_1^u matches the number of equations, thereby facilitating the successful resolution of the equation system. Similarly, the required impedance densities are computed by substituting these solved parameters into the expressions for impedance density.

In the same-side transmissive beam splitting scenario, the -1st and +1st transmission modes are regarded as the two transmission split beams. Thus, we have

$$a_{-1} = a_0 = a_1 = b_0 = 0, b_{-1} = e^{j\varphi_{-1}^l}\sqrt{P_{-1}^l\beta_1/\beta_0} \tag{4.34}$$

Equation (4.34) signifies that all reflection modes and the transmission 0th mode power are suppressed, while the transmission -1st mode power is denoted as P_{-1}^l. In this scenario, no additional consideration is required for the transmission +1st mode, and its power will be determined as $P_1^l = 1 - P_{-1}^l$. Similarly, an additional equation $\left|e^{j\varphi_{-1}^l}\right| - 1 = 0$ should be incorporated when solving the system of equations for the unknowns d_1, d_2, d_3, d_4, h and φ_{-1}^l. Following this, the required load impedance densities can be computed.

In the opposite-side beam splitting scenario, the +1st reflection mode and +1st transmission

mode are regarded as the two split beams. Consequently, it results in

$$a_{-1} = a_0 = b_{-1} = b_0 = 0, a_1 = e^{j\varphi_1^u}\sqrt{P_1^u \beta_1/\beta_0} \tag{4.35}$$

Equation (4.35) signifies that all diffraction modes are suppressed except for the +1st reflection mode and +1st transmission mode. The power of the +1st reflection mode is denoted as P_1^u, and the power of the +1st transmission mode is $P_1^l = 1 - P_1^u$. Consequently, the parameters of the metagrating can be determined by following the calculation steps outlined for the same-side beam splitting scenario above.

Furthermore, it is crucial to acknowledge that when designing metagratings, Joule losses typically constitute an unavoidable factor affecting efficiency. Particularly, large-amplitude polarization currents can induce significant losses, even if the real part of the load impedance density of the meta-atom is minimal. Analyzing Eqs.(4.11) and (4.15) reveals that the amplitude of the currents is influenced by the substrate thickness h. When the denominators in Eqs. (4.11) and (4.15) become zero, the current amplitudes will tend towards infinity. In such cases, the corresponding thickness can be derived as

$$h = \frac{n}{2\sqrt{\varepsilon_r}}\lambda_0, (n = 0, 1, 2 \ldots) \tag{4.36}$$

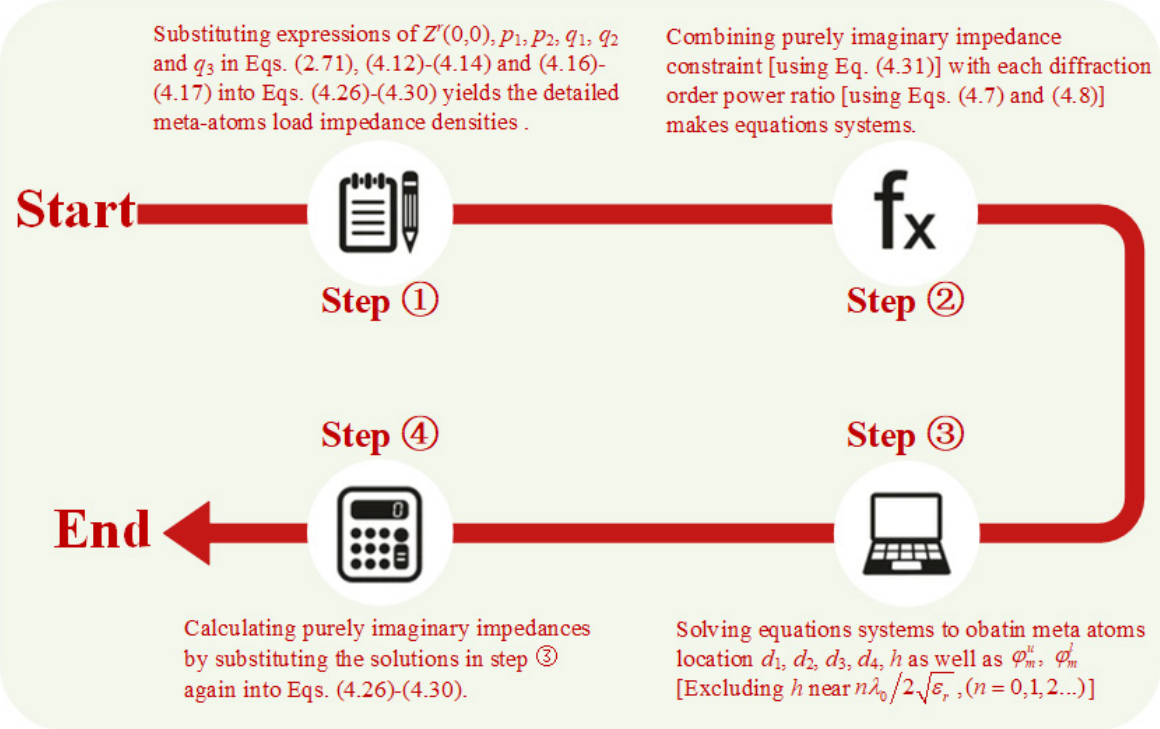

Figure 4.2: Computational flowchart for fully analytical design of transmissive metagratings.

It is crucial to emphasize that not only should the thickness of the substrate as calculated in Eq. (4.36) be avoided, but also the values in its proximity. Interestingly, this finding aligns

with the previous results outlined in subsection 3.2.1, particularly when a supercell comprises two meta-atoms. Consequently, it can be inferred that for a metagrating supercell encompassing arbitrary multiple meta-atoms, the neighboring values of the substrate thickness as indicated in Eq.(4.36) must be circumvented. This corollary serves as a practical and direct guideline in metagrating design endeavors, aiming to mitigate losses attributable to Joule heating as much as possible.

In order to provide a more intuitive understanding of the analytical formulas proposed in this paper for the design of metagratings, the calculation steps are summarized in the flowchart depicted in Figure 4.2.

4.2.2 Design of the supercell

To validate our proposed methodology, a proof-of-study experiment is conducted, which is reported numerically and experimentally for beam manipulation schemes. The operational frequency of the metagrating is fixed at 10 GHz. Since the calculated reactance densities are all negative, and considering the practical feasibility of the model, the wires are replaced by meta-atoms with microstrip capacitor structures to achieve the required impedance density of the wires in the supercell, as depicted in Figure 4.3.

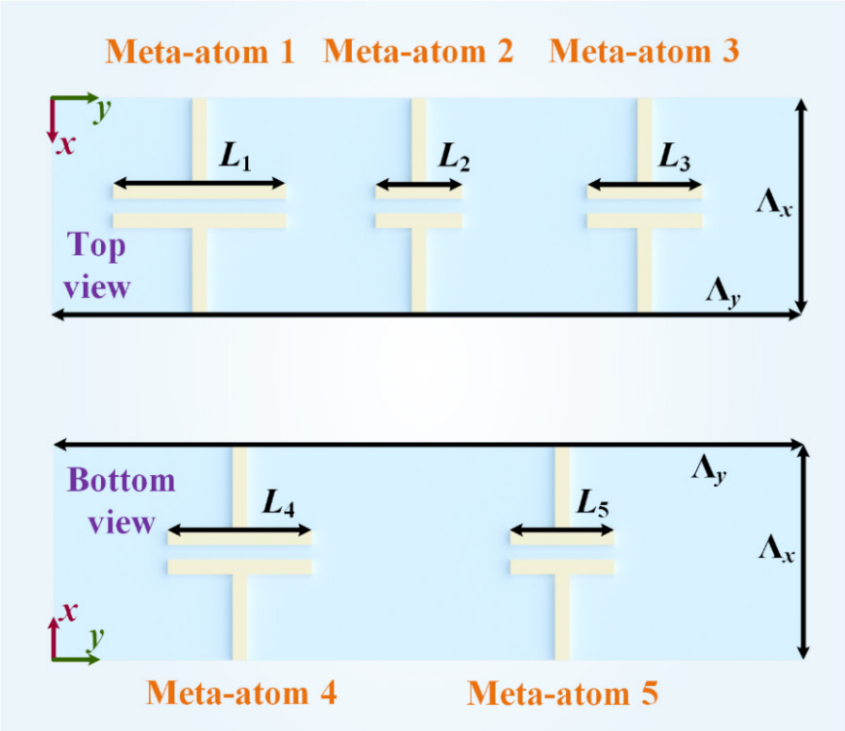

Figure 4.3: Top and bottom views of the transmissive metagrating supercell

The material of the meta-atom is copper, with the thickness and width of the microstrip wire set to t = 0.018 mm and $w = 4r$ = 0.2 mm [48] (where r is the radius of wires in Figure 4.1(b)), respectively. The gap of the capacitor is g = 0.2 mm, and the width is denoted by L, which is determined using Eq.(3.20). The dimensions of the metagrating supercell in the x- and y-directions are considered as $\Lambda_x = \lambda_0/10$ and $\Lambda_y = \lambda_0/\sin\theta_1$ (where θ_1 is the angle of the $+1^{st}$ diffraction mode), respectively, as illustrated in Figure 4.3. The dielectric substrate is selected as F_4BM300 ($\varepsilon_s = 3\varepsilon_0$ and $\tan\delta = 0.0007$) with a thickness h.

4.2.3 Single-beam manipulation

For single-beam manipulation, designs with 75° refraction and 70° reflection are considered, as illustrated in Figure 4.4. Once the angle and power ratio of each diffraction order are determined, the constellation and the load impedance density of each meta-atom in the supercell are calculated using Eqs. (4.31)-(4.33). Subsequently, the dimensions of the meta-atoms can be ascertained, and the final parameters of the metagrating supercells are provided in Table 4.1.

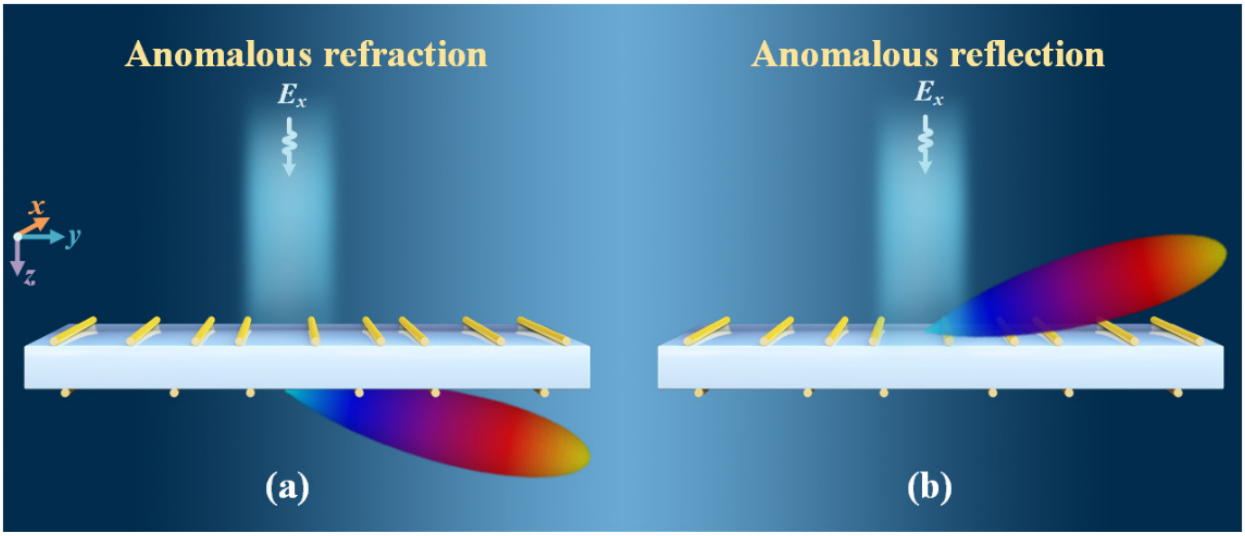

Figure 4.4: Single-beam manipulation conceptual diagram: (a) anomalous refraction, (b) anomalous reflection.

The anomalous refraction and reflection diagrams of the metagratings are depicted in Figure 4.5(a) and (c), respectively, while the simulated performances of the corresponding supercells are illustrated in Figure 4.5(b) and (d). It is evident from the results that for both designs, the energy is almost entirely transformed from the incident wave to the desired outgoing wave at 10 GHz, with less than 0.4% of the power radiated in the direction of undesired diffraction modes. The inevitable dielectric and Joule losses amount to approximately

3.54% and 2.7% for the anomalous refraction and 6.2% and 4.75% for the anomalous reflection, respectively. The higher power absorption in the anomalous reflection design can be attributed to the substrate thickness being closer to the value of h in Eq.(4.36), resulting in larger amplitude polarization currents and subsequently more Joule heat losses together with thicker substrate resulting in higher dielectric loss.

Table 4.1. Parameters of the metagratings with 75° anomalous refraction and 70° anomalous reflection

Parameters \ Supercell type	Anomalous refraction	Anomalous reflection
Λ_x (mm)	3	3
Λ_y (mm)	31.06	31.93
h (mm)	2.37	7.42
d_1 (mm)	10.90	11.30
d_2 (mm)	13.14	10.94
d_3 (mm)	11.19	9.74
d_4 (mm)	12.33	10.48
Z_1^u (η/λ)	-j3.7060	-j2.2093
Z_2^u (η/λ)	-j1.5637	-j4.1663
Z_3^u (η/λ)	-j4.0354	-j2.7461
Z_1^l (η/λ)	-j4.4263	-j4.1104
Z_2^l (η/λ)	-j4.3434	-j4.1231
L_1 (mm)	4.22	5.89
L_2 (mm)	6.92	3.85
L_3 (mm)	3.96	5.19
L_4 (mm)	3.67	3.89
L_5 (mm)	3.72	3.88

It should be noted that although the transmissive metagratings presented here can also achieve anomalous reflection, there are differences compared to the anomalous reflection design based on reflective metagratings discussed in Subsection 3.2.2. In the transmissive design, the substrate thickness is higher, resulting in higher losses, and structurally, five meta-atoms are required compared to two meta-atoms in the reflective metagrating with a ground plane. Therefore, when considering an anomalous reflection design based on metagratings, one needs to choose between reflective or transmissive types based on their specific requirements and constraints.

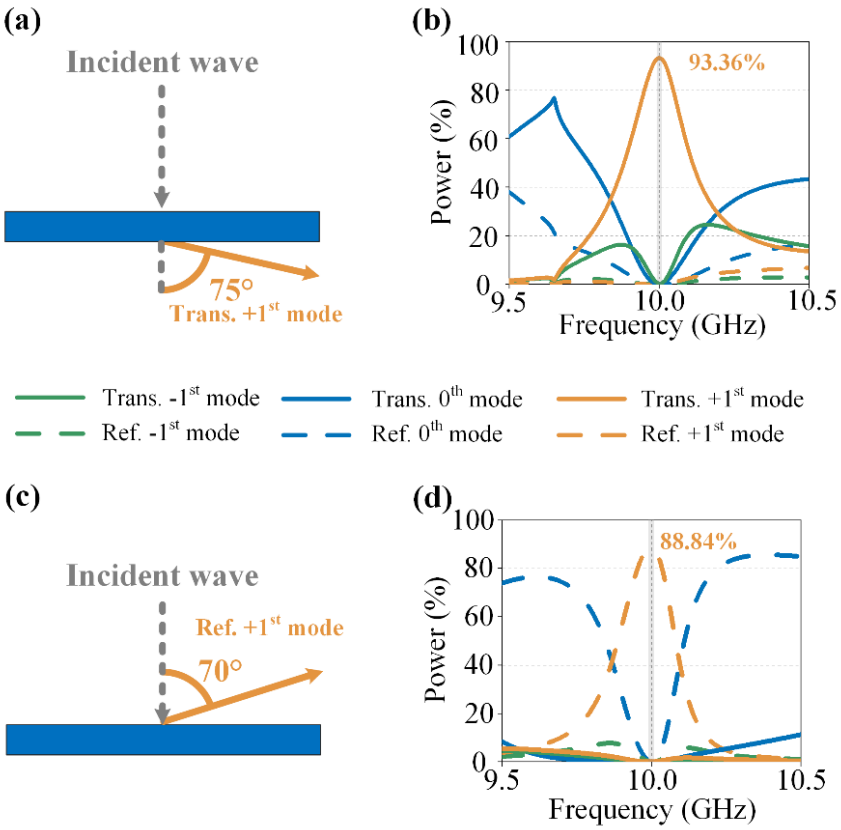

Figure 4.5: Beam manipulation scenarios: (a) anomalous refraction, (c) anomalous reflection. Simulation results of the supercells: (b) anomalous refraction, (d) anomalous reflection.

4.2.4 Multi-beam manipulation

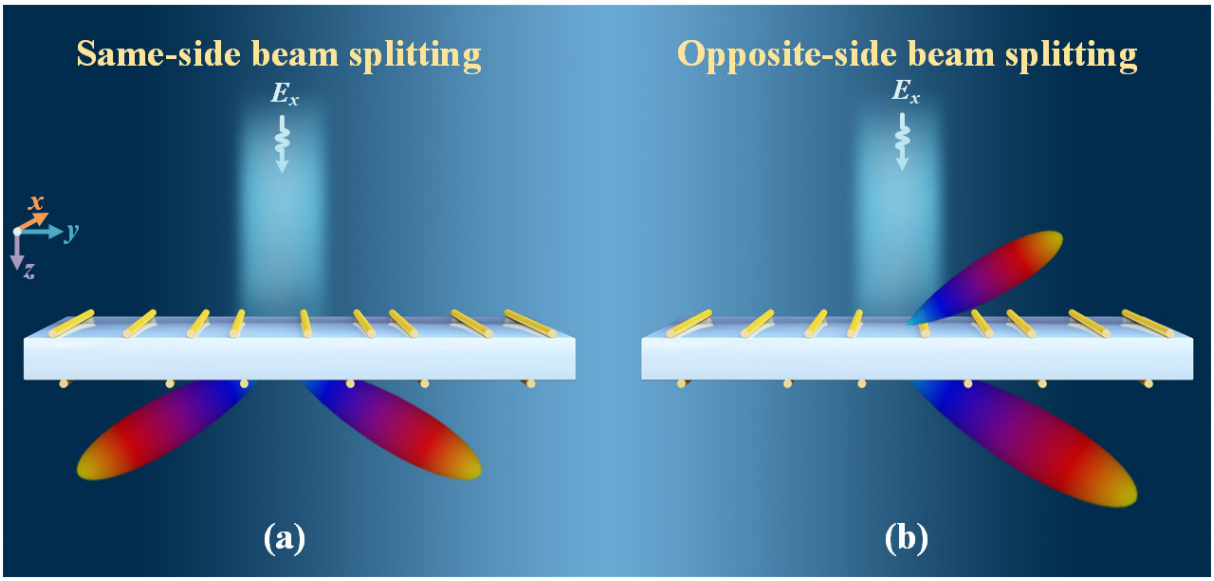

Figure 4.6: Multi-beam manipulation conceptual diagram: (a) same-side beam splitting, (b) opposite-side beam splitting.

For multi-beam manipulation, same-side and opposite-side beam splitting are considered, as depicted in Figure 4.6. In the case of same-side beam splitting, an equal power split beam pointing at -45°/45° is considered, *i.e.*, $P_{-1}^{l} = 1/2$. For opposite-side beam splitting, beams pointing at 45°-reflection/45°-refraction with a power ratio of 3:7 for the +1st reflection mode to the +1st transmission mode are considered, *i.e.*, $P_{1}^{u} = 3/10$. Subsequently, the constellation and the load impedance density of each meta-atom in the supercell are calculated using Eqs. (4.31), (4.34) and (4.35). The dimensions of the meta-atoms can then be determined, and the final parameters of the metagrating supercells are provided in Table 4.2.

Table 4.2. Parameters of the metagratings with same-side and opposite-side beam splitting

Parameters \ Supercell type	Same-side beam splitting	Opposite-side beam splitting
Λ_x (mm)	3	3
Λ_y (mm)	42.43	42.43
h (mm)	2.11	3.58
d_1 (mm)	17.69	12.72
d_2 (mm)	13.66	12.50
d_3 (mm)	17.14	14.80
d_4 (mm)	14.04	5.71
Z_1^u (η/λ)	-*j*3.7342	-*j*6.5647
Z_2^u (η/λ)	-*j*2.8704	-*j*7.2209
Z_3^u (η/λ)	-*j*3.9141	-*j*5.4384
Z_1^l (η/λ)	-*j*4.0259	-*j*5.8628
Z_2^l (η/λ)	-*j*3.9145	-*j*7.4578
L_1 (mm)	4.19	2.53
L_2 (mm)	5.03	2.29
L_3 (mm)	4.05	3.04
L_4 (mm)	3.96	2.83
L_5 (mm)	4.05	2.21

The diagrams for same-side (-45°-transmission and 45°-transmission with a power ratio of 1:1) and opposite-side (45°-reflection and 45°-transmission with a power ratio of 3:7) beam splitting are shown in Figure 4.7(a) and Figure 4.7(c), respectively. The simulated performances of the corresponding supercells are depicted in Figure 4.7(b) and Figure 4.7(d). From the simulation results, it can be observed that the power ratios between the split beams align with the theoretical predictions. For both designs, except for inevitable dielectric as well as Joule losses (same-side beam splitting: 4.02%, opposite-side beam splitting: 6.62%), less than 0.2% of the power is radiated in the direction of undesired diffraction modes (same-side beam

splitting: 0.14%, opposite-side beam splitting: 0.19%).

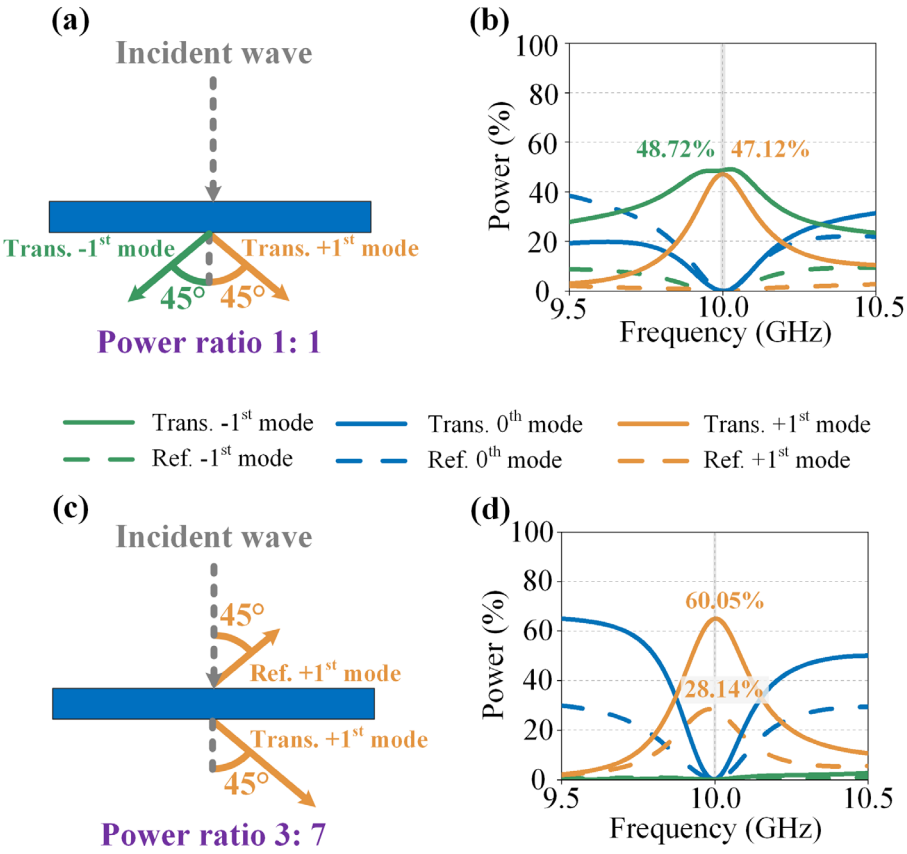

Figure 4.7: Beam-splitting scenarios: (a) same-side beam splitting, (c) opposite-side beam splitting. Simulation results of the supercells: (b) same-side beam splitting, (d) opposite-side beam splitting.

4.2.5 Experimental validation

To further validate the proposed design methodology through experiments, the parameters listed in Table 4.1 are utilized to fabricate the refraction and reflection metagratings using classical PCB technology, as depicted in the photographs in Figure 4.8(a) and (b). The two proof-of-concept prototypes, each comprising 100 × 18 supercells in the *x*- and *y*-directions, respectively, *i.e.*, 300 mm × 574.74 mm and 300 mm × 559.08 mm, are measured using the experimental setup shown in Figure 4.8(c).

The metagrating under test is mounted on a low-index foam support surrounded by microwave absorbing materials, and three standard horn antennas are employed for the measurements. The transmitting antenna is positioned away from the prototype at a distance of 2.5 m to launch a quasi-planar wavefront illumination. Receiving antennas 1 and 2 are mounted on two rotatable mechanical arms to record the scattered waves from the metagrating plate at distances of 2.5 m and 2 m away from the plate, respectively. Finally, the measurement is

conducted by maintaining the transmitter and the metagrating fixed while rotating the mechanical arms with a 1° step.

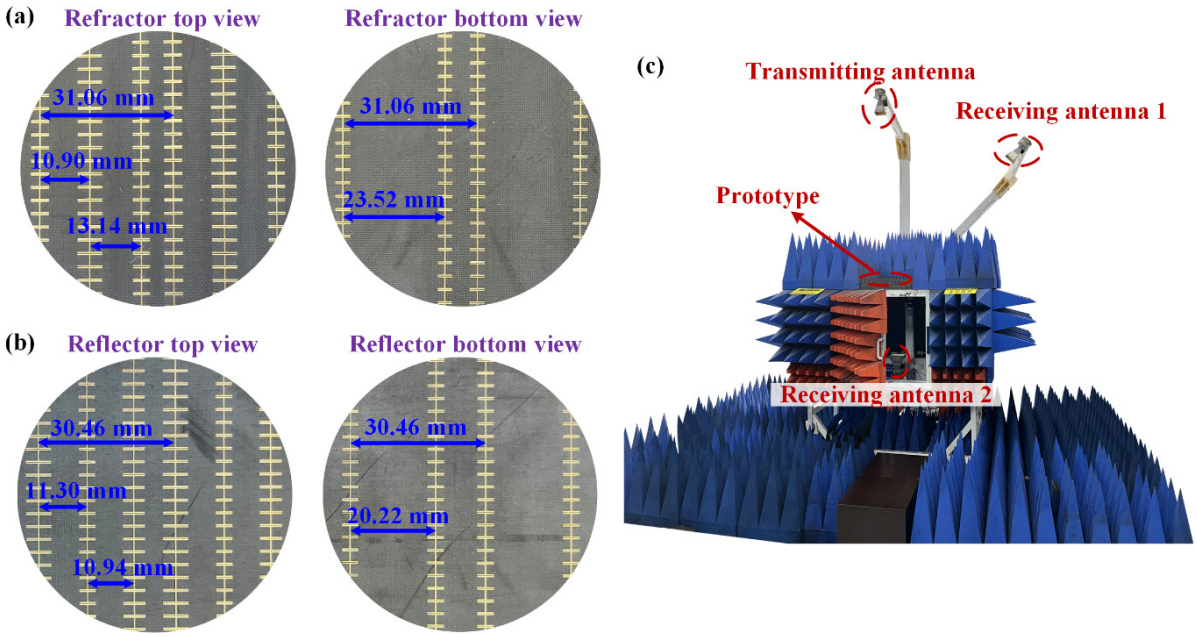

Figure 4.8: Zoomed-in view on two lateral and multiple longitudinal periods of the fabricated metagrating plates: (a) anomalous refractor, (b) anomalous reflector. (c) Experimental setup, consisting of one transmitter and two receiver standard horn antennas, and rotatable arms.

Figure 4.9(a) compares the simulated and measured normalized far-field scattered power of the metagratings at 10 GHz. Besides very small angular errors, the metagratings effectively redirect the incident wave toward the predicted angles. For the 75° anomalous refraction design, the simulation shows a main beam pointing at 73°, while the measurement shows a refraction to 74°. Similarly, for the 70° anomalous reflection design, both simulation and measurement show a main beam pointing at 69°. The observed angular deviations are attributed to the finite size of the metagrating samples. To minimize the deviation with respect to the theoretically expected value, the size of the samples needs to be increased as much as possible.

The diffraction efficiency η_{sca}, defined as the ratio of the power in the direction of the outgoing beam to the total diffracted power of the metagrating, is calculated according to Eq.(3.21). The simulated and measured diffraction efficiency for the 75° anomalous refraction metagrating is found to be 98.24% and 92.65%, respectively. For the 70° anomalous reflection, the diffraction efficiency is 93.26% and 91.19%, in simulation and experiment, respectively. It should be noted that for the total efficiency, Joule losses as well as the edge effects of the board contribute to the power loss.

Finally, the near-field distribution extracted from full-wave simulations, displayed in

Figure 4.9(b), demonstrates that when the incident waves pass through the metagrating board, they both point to the expected angle. Particularly, for the anomalous reflection, it is interesting to observe that no energy is transmitted on the bottom side of the metagrating, even in the absence of a ground plane.

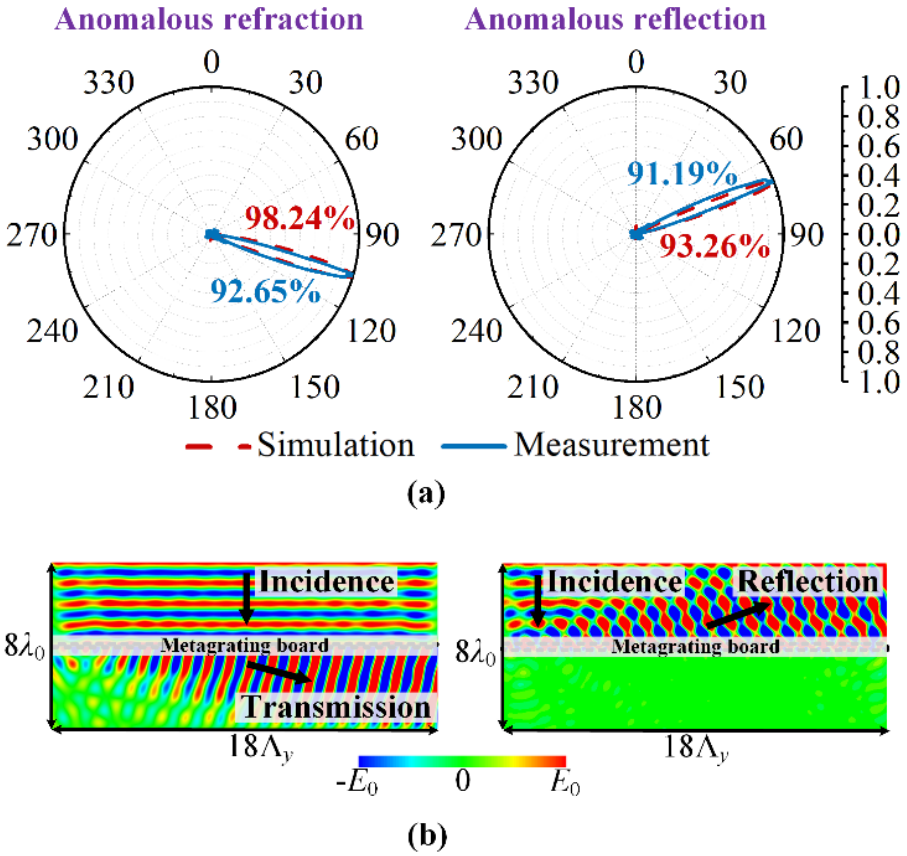

Figure 4.9: (a) Far-field simulation and measurement results of the fabricated metagrating anomalous refractor and anomalous reflector. (b) Near-field simulation result of the fabricated metagrating anomalous refractor and anomalous reflector.

4.3 Uni- and bi-directional electromagnetic absorption in transmissive-type metagratings

4.3.1 Theoretical analysis and synthesis

In the above subsection 4.2, anomalous refraction, anomalous reflection and beam splitting were achieved by controlling the propagating diffraction orders in the transmissive metagratings. Additionally, in subsection 3.4, electromagnetic absorption was successfully demonstrated by suppressing all propagating diffraction orders in reflective metagratings. Consequently, it is natural to inquire whether electromagnetic absorption can also be achieved by suppressing all propagating diffraction orders in transmissive metagratings. Thus, in this

section, further exploration into the suppression of all propagating diffraction orders in the transmissive metagratings to realize wave absorption design is conducted.

The schematic of the considered transmissive metagratings aimed at achieving high-efficiency uni- and bi-directional electromagnetic absorption is illustrated in Figure 4.10(a). Under illumination by TE-polarized electromagnetic waves, uni- or bi-directional absorption can be realized by strategically arranging wires with specific load impedance density on the upper and lower layers of the metagrating. The electromagnetic properties of both the external excitation source and the dielectric substrate of the metagrating align with those described in the previous subsection 4.2. The side view of the supercell composing the metagrating with the established coordinate system is depicted in Figure 4.10(b). The supercell here comprises two conducting wires, one positioned on each face of the dielectric substrate with thickness h, with their coordinates denoted as $(y_1, z_1) = (0, -h)$, $(y_2, z_2) = (d, 0)$.

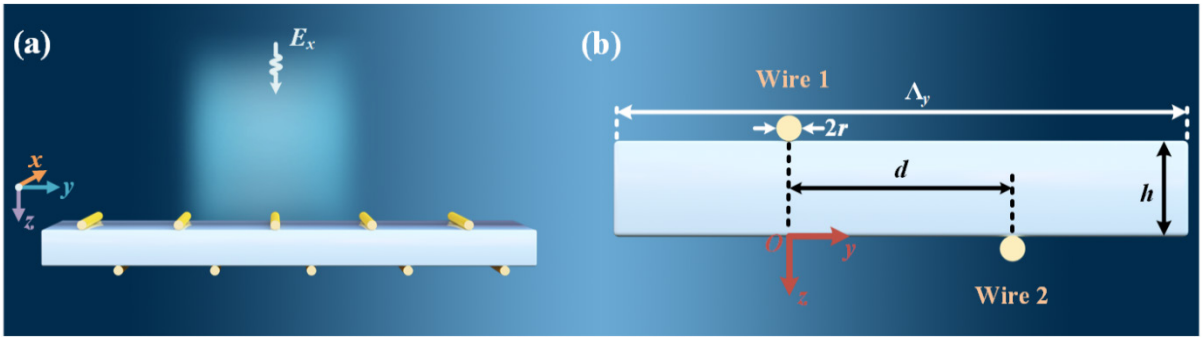

Figure 4.10: (a) Considered transmissive metagrating for wave absorption and excitation sources. (b) Side view of the supercell composing the metagrating.

Built upon the analysis provided in subsection 2.4.2, under the condition of forward normal incidence, the total field within the upper half-space ($z \leq -h$) of the metagrating can be formulated as follows

$$E_{\mathrm{UF}}^{\mathrm{tot}} = E_{\mathrm{in}} e^{-j\beta_0(z+h)} e^{-j\xi_0 y} + \sum_{m=-\infty}^{\infty} E_m^{\mathrm{UF}} e^{-j\xi_m y} e^{j\beta_m(z+h)} \tag{4.37}$$

Similarly, the total field within the lower space ($z \geq 0$) of the metagrating is described as

$$E_{\mathrm{LF}}^{\mathrm{tot}} = \sum_{m=-\infty}^{\infty} E_m^{\mathrm{LF}} e^{-j\xi_m y} e^{-j\beta_m z} \tag{4.38}$$

In the expressions provided, the abbreviations 'UF' and 'LF' denote, respectively, the upper and lower space fields generated under forward incidence. E_m^{UF} and E_m^{LF} represent the amplitudes of the m^{th} order diffraction mode in the upper and lower spaces of the metagrating, respectively. These quantities also correspond to the reflection and transmission diffraction modes, and are defined as follows

$$E_m^{\mathrm{UF}} = -\frac{\eta_0 k_0}{2\Lambda_y}\left(I_{\mathrm{U}}^{\mathrm{F}} \frac{1+\Gamma_m}{\beta_m} + I_{\mathrm{L}}^{\mathrm{F}} \frac{T_m}{\beta_m} e^{j\xi_m d}\right) + \delta_{m0} E_{\mathrm{in}} \Gamma \tag{4.39}$$

$$E_m^{\mathrm{LF}} = -\frac{\eta_0 k_0}{2\Lambda_y}\left(I_{\mathrm{U}}^{\mathrm{F}}\frac{T_m}{\beta_m} + I_{\mathrm{L}}^{\mathrm{F}}\frac{1+\Gamma_m}{\beta_m}e^{j\xi_m d}\right) + \delta_{m0}E_{\mathrm{in}}T \tag{4.40}$$

where $I_{\mathrm{U}}^{\mathrm{F}}$ and $I_{\mathrm{L}}^{\mathrm{F}}$ represent the generated line currents on the upper and lower wires in the supercell under forward illumination, respectively. Additionally, Γ_m and T_m denote the Fresnel reflection and transmission coefficients of the m^{th} diffraction mode, which are specified in Eqs. (2.63) and (2.64).

Since bi-directional absorption is also targeted, an analysis of the field distribution of the same electromagnetic wave when it is incident from the backside is also conducted. For backward incidence, the total field in the upper half-space of the metagrating can be derived as

$$E_{\mathrm{UB}}^{\mathrm{tot}} = \sum_{m=-\infty}^{\infty} E_m^{\mathrm{UB}} e^{-j\xi_m y}\, e^{j\beta_m(z+h)} \tag{4.41}$$

The total field in the lower space ($z \geq 0$) of the metagrating is expressed as follows

$$E_{\mathrm{LB}}^{\mathrm{tot}} = E_{\mathrm{in}} e^{-j\beta_0 z} e^{-j\xi_0 y} + \sum_{m=-\infty}^{\infty} E_m^{\mathrm{LB}} e^{-j\xi_m y}\, e^{-j\beta_m z} \tag{4.42}$$

In order to differentiate it from the field expressions under forward incidence, the abbreviations 'UB' and 'LB' are employed to denote the upper and lower space fields generated under backward incidence. Consequently, E_m^{UB} and E_m^{LB} are then formulated as

$$E_m^{\mathrm{UB}} = -\frac{\eta_0 k_0}{2\Lambda_y}\left(I_{\mathrm{U}}^{\mathrm{B}}\frac{1+\Gamma_m}{\beta_m} + I_{\mathrm{L}}^{\mathrm{B}}\frac{T_m}{\beta_m}e^{j\xi_m d}\right) + \delta_{m0}E_{\mathrm{in}}T \tag{4.43}$$

$$E_m^{\mathrm{LB}} = -\frac{\eta_0 k_0}{2\Lambda_y}\left(I_{\mathrm{U}}^{\mathrm{B}}\frac{T_m}{\beta_m} + I_{\mathrm{L}}^{\mathrm{B}}\frac{1+\Gamma_m}{\beta_m}e^{j\xi_m d}\right) + \delta_{m0}E_{\mathrm{in}}\Gamma \tag{4.44}$$

where $I_{\mathrm{U}}^{\mathrm{B}}$ and $I_{\mathrm{L}}^{\mathrm{B}}$ represent the generated line currents on the upper and lower wires under backward illumination. In the context of backward incidence, where the incidence occurs below the metagratings, the upper diffraction mode E_m^{UB} represents the m^{th} transmission diffraction mode, while E_m^{LB} represents the m^{th} reflection mode.

Here, wave absorption occurs through the interferences between the reflection of the incident wave and the 0^{th} reflection diffraction mode, as well as the transmission of the incidence and the 0^{th} transmission diffraction mode, simultaneously. Consequently, the period Λ_y of the metagrating is selected to ensure that only the 0^{th} diffraction mode is predominant, while other diffraction modes become evanescent. Thus, Λ_y should adhere to the relationship $\Lambda_y < \lambda_0$.

4.3.2 Tailoring uni-directional electromagnetic absorption

The scheme of uni-directional absorption is depicted in Figure 4.11(a), where only the absorption under forward incidence is considered, adhering to the requirement of simultaneously nullifying $E_0^{\mathrm{UF}} = 0$ and $E_0^{\mathrm{LF}} = 0$ in Eqs.(4.39) and (4.40). Consequently, we

can derive

$$-\frac{\eta_0}{2\Lambda_y}\left[I_{\mathrm{U}}^{\mathrm{F}}(1+\Gamma)+I_{\mathrm{L}}^{\mathrm{F}}Te^{j\xi_0 d}\right]+E_{\mathrm{in}}\Gamma=0 \tag{4.45}$$

$$-\frac{\eta_0}{2\Lambda_y}\left[I_{\mathrm{L}}^{\mathrm{F}}(1+\Gamma)e^{j\xi_0 d}+I_{\mathrm{U}}^{\mathrm{F}}T\right]+E_{\mathrm{in}}T=0 \tag{4.46}$$

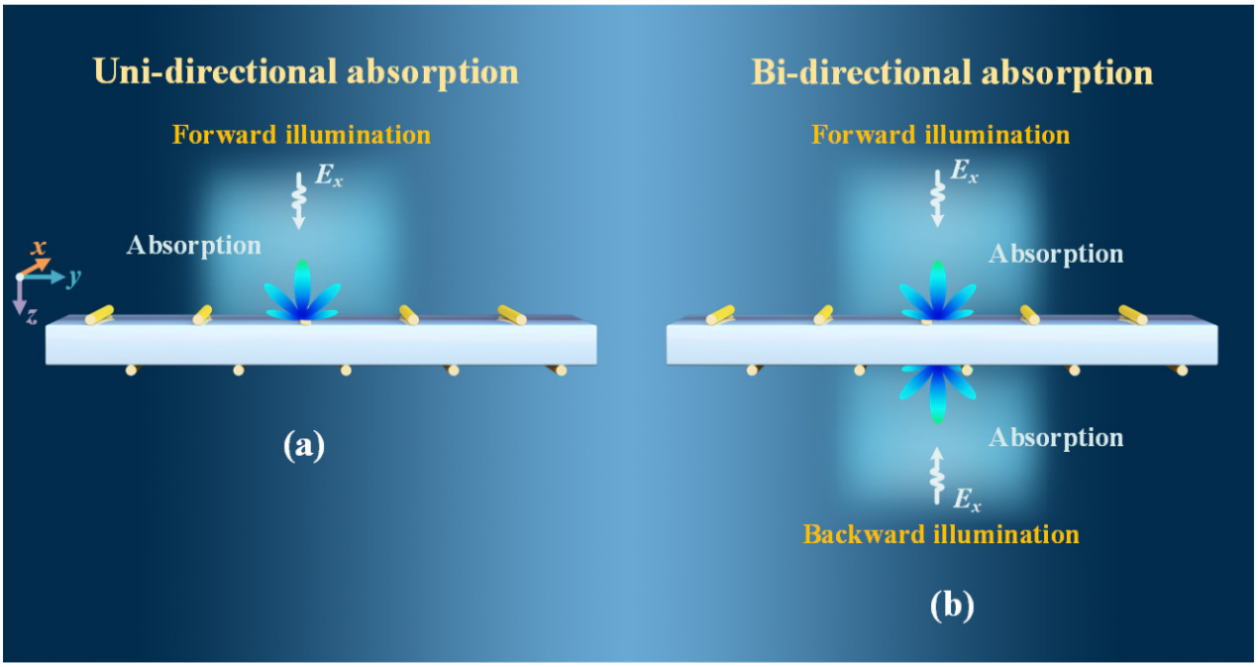

Figure 4.11: Conceptual diagram of a transmissive-type metagrating for electromagnetic absorption: (a) uni-directional absorption, (b) bi-directional absorption.

Then, upon solving the aforementioned system of equations, the expression for the line currents can be derived as follows

$$I_{\mathrm{U}}^{\mathrm{F}}=\frac{\Lambda_y}{\eta_0}E_{\mathrm{in}}p \tag{4.47}$$

$$I_{\mathrm{L}}^{\mathrm{F}}=\frac{\Lambda_y}{\eta_0}E_{\mathrm{in}}q \tag{4.48}$$

where p and q are given as

$$p=2\frac{\Gamma(1+\Gamma)-T^2}{(1+\Gamma)^2-T^2} \tag{4.49}$$

$$q=\frac{2T}{(1+\Gamma)^2-T^2} \tag{4.50}$$

Combining Eqs.(4.37), (4.38), (4.47), (4.48), and Ohm's law $E^{\mathrm{tot}}=ZI$, the required load impedance density of the wires on the upper layer $Z_{\mathrm{U}}^{\mathrm{F}}$ and lower layer $Z_{\mathrm{L}}^{\mathrm{F}}$ for absorption under forward illumination can be calculated. For the fabrication of the metagratings using microstrip structures via printed circuit board (PCB) technology, the cylindrical wires must be replaced with flat ones with relationship $w = 4r$ [48], where w is the width of the flat wire and r is the radius of the cylindrical wire. Consequently, the final load impedance density of the wires on

the upper and lower layers for uni-directional absorption can thus be calculated and simplified as

$$Z_{\mathrm{U}}^{\mathrm{F}} = \frac{\eta_0}{\Lambda_y}\frac{1+\Gamma}{p} - Z_{\mathrm{self}} - \frac{q}{p}Z_{\mathrm{mutual}} \tag{4.51}$$

$$Z_{\mathrm{L}}^{\mathrm{F}} = \frac{\eta_0}{\Lambda_y}\frac{T}{p} - Z_{\mathrm{self}} - \frac{p}{q}Z_{\mathrm{mutual}} \tag{4.52}$$

with

$$Z_{\mathrm{self}} = Z^r(0,0) = \frac{\eta_0(1+\Gamma)}{\Lambda_y} + j\frac{\eta_0}{\lambda_0}\left\{\sum_{m=1}^{\infty}\left[\frac{2\pi(1+\Gamma_m)}{\Lambda_y\alpha_m} - \frac{1}{m}\right] - \ln\left(\frac{\pi w}{2\Lambda_y}\right)\right\} \tag{4.53}$$

$$Z_{\mathrm{mutual}} = Z^t(0,d) = j\frac{k_0\eta_0}{2\Lambda_y}\sum_{m=-\infty}^{\infty}\frac{T_m}{\alpha_m}e^{-j\xi_m d} \tag{4.54}$$

where the functions $Z^r(y,z)$ and $Z^t(y,z)$ are defined in Eqs. (2.71) and (2.72), respectively, and α_m is given as $\alpha_m = j\beta_m$.

By analyzing Eqs.(4.51) and (4.52) it can be observed that to achieve absorption under forward illumination, the metagrating period length Λ_y, the substrate thickness h, the relative permittivity of the substrate ε_r, the line width w of the wires and the horizontal distance d between the wires can be arbitrarily selected. Once these parameters are determined, the load impedance density of the two wires can be calculated accordingly. For instance, considering an operating frequency of 10 GHz and a dielectric substrate such as F_4BM 300 (ε_r = 3 and tan δ = 0.0007), the choice of the horizontal distance d between the two wires entails two different designs: $d = 0$ and $d \neq 0$.

Although from Eqs. (4.51) and (4.52) do not impose restrictions on the choice of parameters, it is important to note that certain inappropriate choices can lead to complexity or practical implementation challenges, such as when the real part of the impedance density becomes negative. Therefore, three main considerations are crucial for parameter selection: the structure must be sparse, *i.e.*, period length Λ_y should not be less than $\lambda_0/2$, the thickness h of the substrate must be lower than $\lambda_0/10$, and finally, for a practical implementation, the real part of the impedance density ($\Re(Z)$) should not be negative.

First, considering the scenario where the meta-atoms on the faces are not aligned ($d \neq 0$), a horizontal distance of d = 4 mm is selected between two meta-atoms. Parameters such as the period length Λ_y and the substrate thickness h are chosen as Λ_y = 20 mm and h = 2 mm, respectively, taking into account the three parameter selection factors mentioned above. Subsequently, the required impedance densities of the two meta-atoms are calculated as $Z_{\mathrm{U}} = Z_{\mathrm{U}}^{\mathrm{F}}$ = (0.1933 - *j*5.4511) η/λ and $Z_{\mathrm{L}} = Z_{\mathrm{L}}^{\mathrm{F}}$ = (0.0836 - *j*4.9104) η/λ, respectively. To realize such a complex load impedance density, the meta-atom model depicted in Fig. 3.16 is employed

for implementation. Furthermore, to ensure the uniformity of the load impedance distribution, the length of the meta-atom in the x-direction is $\Lambda_x = \lambda_0/10$. Finally, the supercell of the metagrating can be constructed, and various views of the supercell are illustrated in Figure 4.12.

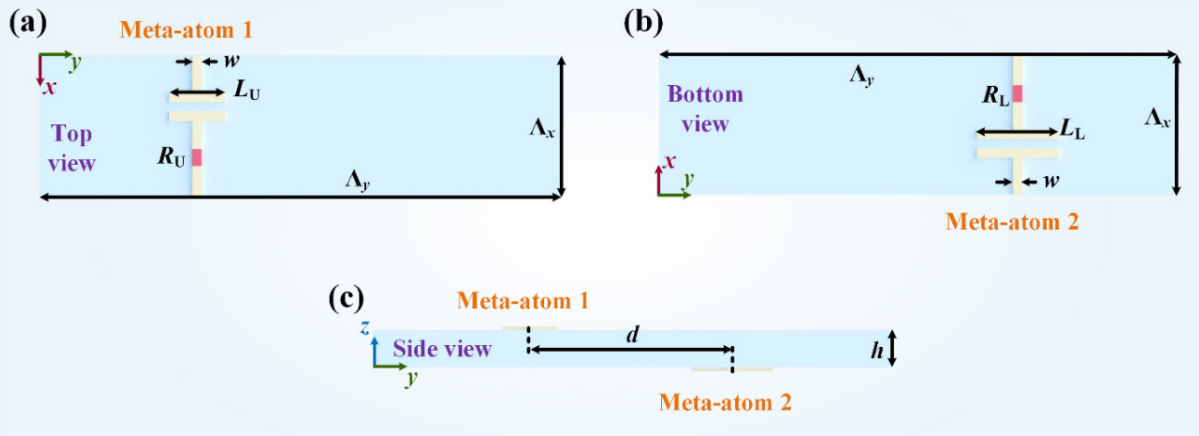

Figure 4.12: Supercell of the metagratings: (a) Top view. (b) Bottom view. (c) Side view.

The length L of the microstrip capacitor can be determined for the required imaginary part of the impedance density $\Im(Z)$ according to Eq.(3.20). Similarly, the resistance value R is obtained for the required real part of the impedance density $\Re(Z)$ according to Eq.(3.29). Subsequently, the capacitor arm length and resistance of the corresponding meta-atoms are calculated as follows: $L_U = 3.05$ mm, $R_U = 7.29\ \Omega$ for the upper meta-atom, and $L_L = 3.38$ mm, $R_L = 3.15\ \Omega$ for the lower meta-atom. Initially, these values serve as ideal starting points for meta-atom modeling and analysis using full-wave simulations in ANSYS HFSS. However, the metal strip capacitor structure inevitably introduces a small amount of impedance density in the real part. Therefore, the parameters L and R need to be optimized in order to achieve the require optimization to achieve optimal results, as conducted in subsection 3.4 for reflective metagratings wave absorption. These optimized values are denoted as CV (calculated value) and OV (optimal value), respectively, and are listed in Table 4.3.

Although the primary focus of the design lies in achieving unidirectional absorption under forward incidence, the structural integrity is also subjected to simulation under backward incidence for comprehensive performance analysis. The simulation outcomes are delineated in Figure 4.13(a), wherein absorption is quantified employing the formula $A = 1\text{-}\Gamma\text{-}T$. Remarkable alterations are discerned in the reflection responses concerning the direction of incident illumination, whereas negligible disparities are observed in the transmission responses. Specifically, when considering unidirectional absorption exclusively, the simulation outcome under forward illumination attains a flawless absorption efficacy at the operational frequency

of 10 GHz, as anticipated. Conversely, under backward illumination, a substantial portion of the incident power is reflected, with a mere 20% being absorbed, primarily attributable to ohmic losses induced by the metallic lines and chip resistors (18%) along with dielectric losses (2%).

Then, in the design where the meta-atoms are aligned above and below (d = 0), the same parameters Λ_y = 20 mm and h = 2 mm are chosen as before. The impedance densities of the upper and lower meta-atoms are calculated as $Z_{\mathrm{U}} = Z_{\mathrm{U}}^{\mathrm{F}}$ = (-0.5539 - j3.9919) η/λ and $Z_{\mathrm{L}} = Z_{\mathrm{L}}^{\mathrm{F}}$ = (0.6115 - j3.8795) η/λ, respectively. However, as encountered earlier, realizing a negative real part of the impedance density is highly challenging. Therefore, alternative suitable values must be selected for Λ_y and h. Accordingly, Λ_y = 15 mm and h = 2.5 mm are chosen, considering the sparse and low-profile features of the metagrating. Subsequently, the required impedance densities of the two meta-atoms are calculated as $Z_{\mathrm{U}} = Z_{\mathrm{U}}^{\mathrm{F}}$ = (0.1221 - j4.4464) η/λ and $Z_{\mathrm{L}} = Z_{\mathrm{L}}^{\mathrm{F}}$ = (0.3419 - j3.8176) η/λ, respectively. The corresponding parameters of the meta-atoms are calculated as follows: L_{U} = 3.73 mm, R_{U} = 4.60 Ω for the upper meta-atom, and L_{L} = 4.35 mm, R_{L} = 12.89 Ω for the lower meta-atom. These parameters are further optimized in simulations.

Table 4.3 Parameters of metagrating supercells for uni- and bi-directional absorption

Parameters \ Supercell type		Uni-directional		Bi-directional		
		$d \neq 0$	$d = 0$	$d \neq 0$	$d = 0$	$d = 0$ (Exp)
Λ_x (mm)		3	3	3	3	3
Λ_y (mm)		20	15	20	17.16	17
h (mm)		2	2.5	4.33	4.33	4
d (mm)		4	0	3.49	0	0
w (mm)		0.2	0.2	0.2	0.2	0.2
Z_{U} (η/λ)		0.1933-j5.4511	0.1221-j4.4464	0.3750-j5.7007	0.4370-j4.7519	0.4318-j4.6500
Z_{L} (η/λ)		0.0836-j4.9104	0.3419-j3.8176	0.3750-j5.7007	0.4370-j4.7519	0.4318-j4.6500
L_{U} (mm)	CV	3.05	3.73	2.91	3.49	3.57
	OV	2.94	3.47	2.78	3.32	3.44
L_{L} (mm)	CV	3.38	4.35	2.91	3.49	3.57
	OV	3.26	4.05	2.78	3.32	3.44
R_{U} (Ω)	CV	7.29	4.60	14.14	16.47	16.27
	OV	5.10	3.91	10.96	13.18	11.5
R_{L} (Ω)	CV	3.15	12.89	14.14	16.47	16.27
	OV	2.21	10.96	10.96	13.18	11.5

CV: calculated value; OV: optimal value.

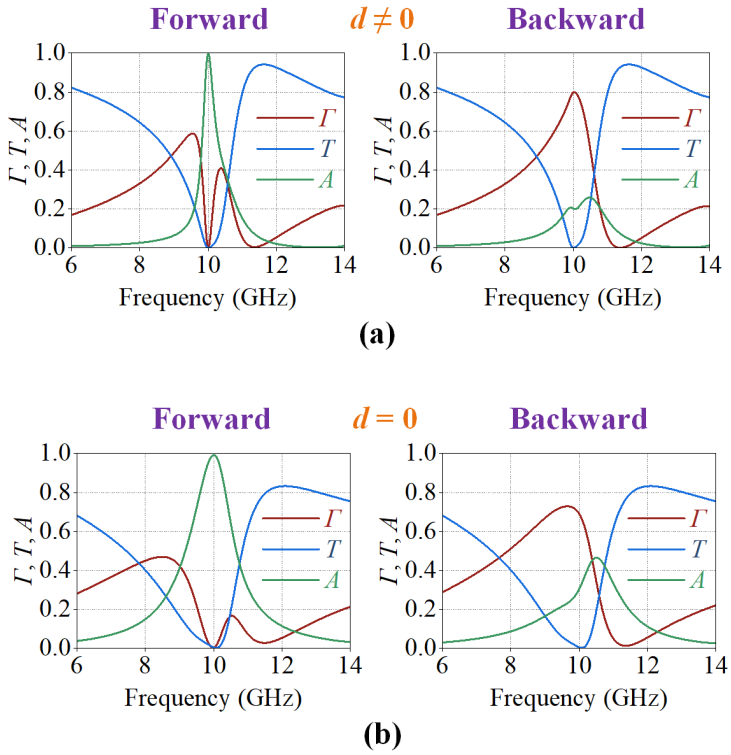

Figure 4.13: Simulation results of the supercell with optimized parameters for uni-directional absorption. (a) $d \neq 0$, (b) $d = 0$.

The simulation results for both forward and backward illuminations of the supercell are depicted in Figure 4.13(b). The results indicate that absorption under forward incidence aligns well with expectations. However, when illuminated from the backward direction, a 70% reflection efficiency is observed. The higher reflection loss observed here compared to the $d \neq 0$ case may be attributed to the larger total resistor value ($R_U + R_L$) utilized, as shown in Table 4.3. Additionally, the larger total resistance also results in a wider absorption bandwidth for $d = 0$ under forward illumination compared to the $d \neq 0$ case, as discussed in subsection 3.4.

4.3.3 Tailoring bi-directional electromagnetic absorption

In this subsection, electromagnetic absorption under both forward and backward illuminations is targeted, as schematically depicted in Figure 4.11(b). In the case of the backward incident wave, it is essential to ensure that $E_0^{\mathrm{UB}} = E_0^{\mathrm{LB}} = 0$ in Eqs.(4.43) and (4.44). Subsequently, the impedance density of the meta-atoms on the top and bottom faces of the metagrating can be obtained following the same analytical methodology in subsection 4.3.2 as

$$Z_{\mathrm{U}}^{\mathrm{B}} = \frac{\eta_0}{\Lambda_y}\frac{T}{q} - Z_{\mathrm{self}} - \frac{p}{q}Z_{\mathrm{mutual}} \tag{4.55}$$

$$Z_{\mathrm{L}}^{\mathrm{B}} = \frac{\eta_0}{\Lambda_y}\frac{1+\Gamma}{p} - Z_{\mathrm{self}} - \frac{q}{p}Z_{\mathrm{mutual}} \tag{4.56}$$

where $Z_{\mathrm{U}}^{\mathrm{B}}$ and $Z_{\mathrm{L}}^{\mathrm{B}}$, respectively, denote the required load impedance density of the wires on the upper and lower layers under backward illumination. Therefore, to ensure simultaneous absorption under both forward and backward illuminations, it is imperative to ensure that $Z_{\mathrm{U}}^{\mathrm{F}}$ in Eq.(4.51) is identical to $Z_{\mathrm{U}}^{\mathrm{B}}$ in Eq.(4.55), and $Z_{\mathrm{L}}^{\mathrm{F}}$ in Eq.(4.52) is identical to $Z_{\mathrm{L}}^{\mathrm{B}}$ in Eq.(4.56). Thus, we can establish

$$\left(\frac{q}{p}-\frac{p}{q}\right)Z_{\mathrm{mutual}}-\left(\frac{1+\Gamma}{p}-\frac{T}{q}\right)=0 \tag{4.57}$$

After some algebraic simplification and analysis, the solutions of this equation are as follows

$$\frac{1+\Gamma}{p}-\frac{T}{q}=0 \tag{4.58}$$

$$\sum_{m=-\infty}^{\infty}\frac{T_m}{\alpha_m}\exp\left(-j\frac{2\pi m}{\Lambda_y}d\right)=0 \tag{4.59}$$

From Eq.(4.58), the value of parameter *h* can be solved as

$$h=\frac{(2n-1)\lambda_0}{4\sqrt{\varepsilon_r}}\,(n=1,2,3,\dots) \tag{4.60}$$

Similarly, the parameters Λ_y and *d* can be solved using Eq.(4.59). Substituting Eqs.(4.58) and (4.59) into Eqs.(4.55) and (4.56), the impedance densities for the meta-atoms for bi-directional absorption are obtained as

$$Z_{\mathrm{U}}=Z_{\mathrm{L}}=\frac{\eta_0}{\Lambda_y}\frac{1}{\varepsilon_r+1}-j\frac{\eta_0}{\lambda_0}\left\{\sum_{m=1}^{\infty}\left[\frac{2\pi(1+\Gamma_m)}{\Lambda_y\alpha_m}-\frac{1}{m}\right]-\ln\left(\frac{\pi w}{2\Lambda_y}\right)\right\} \tag{4.61}$$

Hence, it is necessary to ensure symmetry in the metagrating with similar designs on the top and bottom faces when aiming for similar bi-directional feature.

Here also, two types of metagratings, depending on whether the upper and lower meta-atoms are aligned or not, are considered for bi-directional absorption. Unlike the previous uni-directional absorption design where each parameter can be chosen with no theoretical restrictions, here the value of parameter *h* has to satisfy Eq.(4.60). Additionally, parameters Λ_y and *d* are mutually determining factors according to Eq.(4.59), *i.e.*, after choosing one of the parameters, the other parameter is also determined.

Consideration is given to the scenario where the alignment of the top and bottom meta-atoms is non-coincident ($d \neq 0$). To preserve the sparse configuration of the metagrating, the supercell's periodicity is set as Λ_y = 20 mm, while the inter-element spacing, *d*, is determined using Eq.(4.59) yielding to *d* = 3.49 mm. Furthermore, for achieving a low-profile metagrating, the minimum permissible value of *h* is selected in accordance with Eq.(4.60), yielding to *h* = 4.33 mm. Consequently, the impedance densities required for the two meta-atoms can be derived using Eq.(4.61) as $Z_{\mathrm{U}} = Z_{\mathrm{L}} = (0.3750\text{-}j5.7007)\eta/\lambda$. Subsequently, the pertinent parameters of the meta-atoms are computed employing Eqs.(4.20) and (4.39), yielding $L_{\mathrm{U}} = L_{\mathrm{L}}$

= 2.91 mm and $R_U = R_L = 14.14\ \Omega$. By fine-tuning these parameters using simulations, optimal outcomes can be attained, as detailed in Table 4.3.

Simulations are conducted for both forward and backward incidences, as illustrated by the results depicted in Figure 4.14 (a). The reflection and transmission curves exhibit identical behavior in both scenarios due to the perfect symmetry of the structure from top to bottom, resulting in the anticipated phenomenon of perfect wave absorption at the operational frequency. Notably, an additional peak with an absorption rate of approximately 50% manifests at 13 GHz. This occurrence is attributed to the impedance densities and spatial arrangements of the meta-atoms, which facilitate partial absorption at 13 GHz, albeit not meeting the criteria for complete absorption. Consequently, the exploration of achieving multiple absorption peaks through a system of equations in the theoretical model could be a prospective avenue for further investigation, potentially necessitating the incorporation of supplementary meta-atoms.

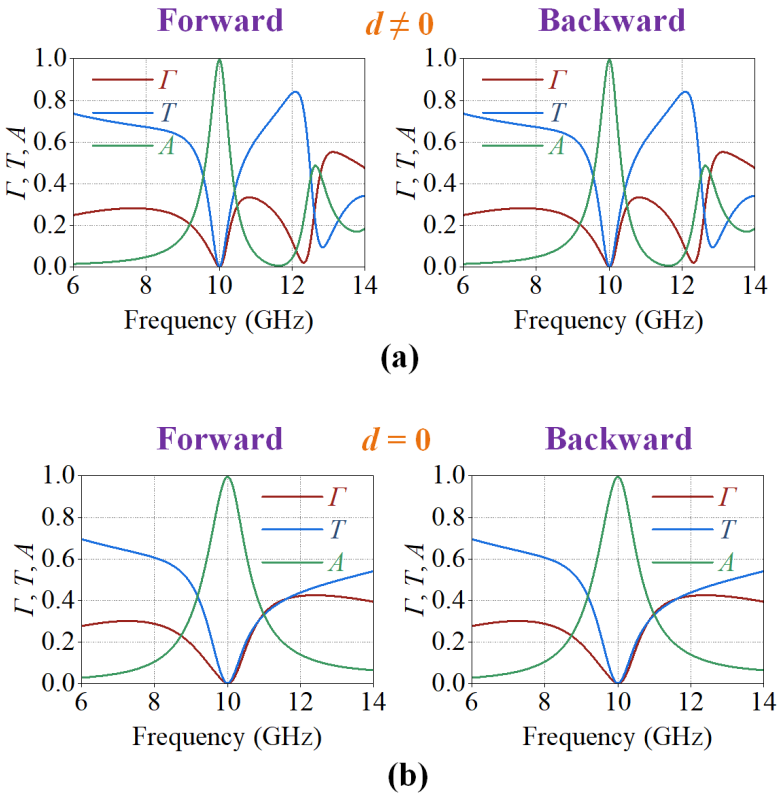

Figure 4.14: Simulation results of the supercell with optimized parameters for bi-directional absorption. (a) $d \neq 0$, (b) $d = 0$.

In the scenario where the alignment of the top and bottom meta-atoms is perfect, *i.e.*, $d = 0$, the period length of the supercell is computed as Λ_y, = 17.16 mm using to Eq.(4.59) Similarly, a substrate thickness of h = 4.33 mm is chosen to maintain a low profile. Subsequently, the required impedance densities of the two meta-atoms are determined via Eq.(4.61) as $Z_U = Z_L$ =

$(0.4370\text{-}j4.7519)\eta/\lambda$ with the corresponding parameters of the meta-atoms calculated as $L_U = L_L = 3.49$ mm and $R_U = R_L = 16.47$ Ω. The simulation results depicted in Figure 4.14(b) exhibit fully symmetrical characteristics of reflection, transmission, and absorption across frequency for both incident waves. Notably, akin to the uni-directional configuration, the structure demonstrates a broader absorption bandwidth when the top and bottom layers are perfectly aligned ($d = 0$), owing to the increased total resistor value ($R_U + R_L$) of the meta-atoms.

4.3.4 Experiments and discussions

For proof-of-concept validation, the metagrating structure with perfect alignment ($d = 0$), optimized for bi-directional electromagnetic absorption, is fabricated using PCB technique. The resistance value can be approximated using commercial 01005 series chip resistors. Regarding the dielectric substrate, all parameters are derived from a rigorous solution of equations. Since the parameter h is constrained by commercially available substrates, solving the equations directly becomes infeasible. In this context, the system of overdetermined equations necessitates the application of the least squares method to determine the optimal solution. Initially, the original substrate thickness $h = 4.33$ mm is adjusted to the commercially available value of 4 mm, and the original period length $\Lambda_y = 17.16$ mm is rounded to the nearest integer $\Lambda_y = 17$ mm. Subsequently, the optimal solution is sought using the nonlinear least-squares solver lsqnonlin in Matlab. Upon obtaining the optimal impedance densities $Z_U = Z_L = (0.4318\text{-}j4.6500)\eta/\lambda$ maximizing bi-directional wave absorption, the parameters of the meta-atoms are calculated and refined to finalize the design process, as detailed in Table 4.3.

The $d = 0$ bi-directional absorber metagrating is successfully fabricated, incorporating chip resistors into the structure. The fabricated prototype comprises 100 × 35 supercells in both the x- and y-directions, resulting in dimensions of 300 mm × 595 mm. Detailed zoom views of the top and bottom faces of the prototype are depicted in Figure 4.15(a). The measurement setup schematic corresponds to the configuration illustrated in Figure 4.8(c). Due to practical constraints aimed at preventing antenna collisions, the reflection coefficient is measured for an incidence angle of $\theta_i = -2°$ and a receiving angle $\theta_r = 2°$. The simulation and measurement results are compared in in Figure 4.15(b).

Despite inherent discrepancies stemming from fabrication deviations and the limited sample size of the metagrating, the measurement results manifest slight deviations in comparison to the simulated data. Nonetheless, the measured absorption efficiency achieves approximately 92% at 10 GHz, thereby corroborating the favorable bi-directional absorption

characteristics of the device. Further evaluation of the device's performance entails the determination of a figure of merit (FOM) at -10 dB utilizing Eq.(3.35). The FOM extracted from experimental data under forward and backward illuminations is computed as 0.028 and 0.027, respectively. In comparison to the wave absorption based on reflective metagratings discussed in Chapter 3.4 and referenced [49], the FOM of wave absorption in transmissive metagratings is relatively smaller. Consequently, reflective metagratings remain a preferred option for wave absorption design, especially when prioritizing uni-directional absorption and a broader absorption bandwidth.

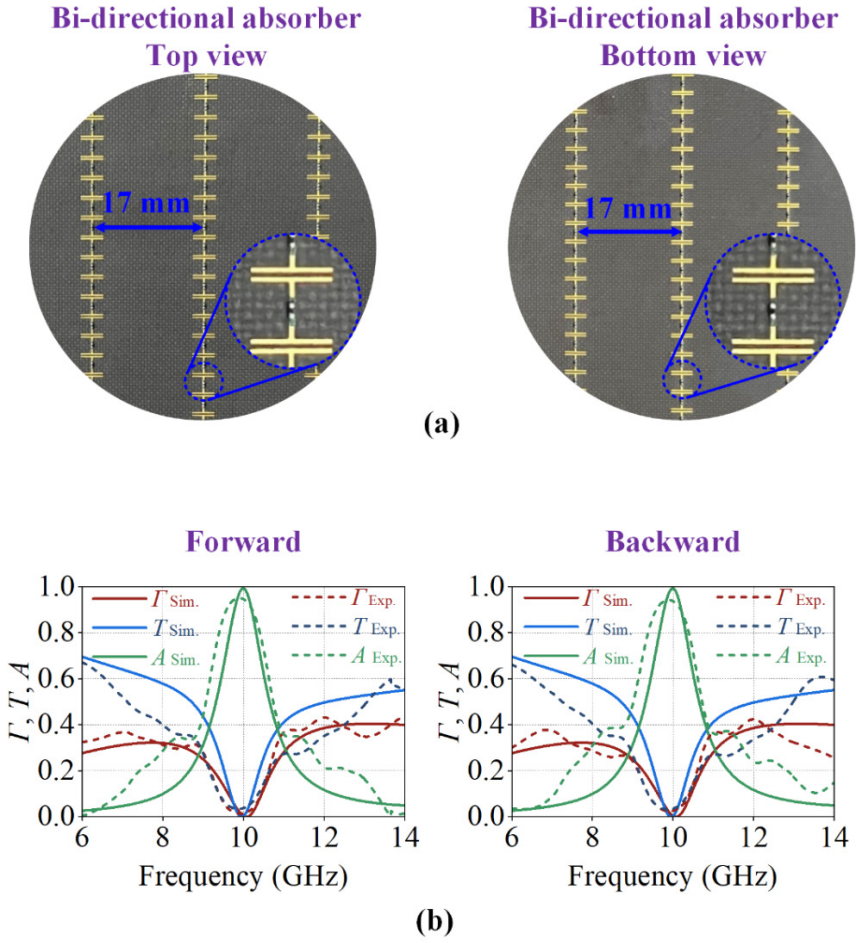

Figure 4.15: (a) Top and bottom views of the fabricated metagrating bi-directional absorber. (c) Simulated and measured reflection Γ, transmission T, and absorption A coefficients of metagrating bi-directional absorber under forward and backward illuminations.

4.4 Janus metagratings

4.4.1 Theoretical analysis and synthesis

In Section 4.3, while focusing solely on designing uni-directional wave absorption, we

exclusively considered absorption under forward incidence, neglecting design considerations for backward incidence. However, simulation results revealed that under backward incidence, the design predominantly exhibited reflection (80%) with a minor portion (20%) contributing to absorption. Consequently, with such a transmissive metagrating, it prompts inquiry into the feasibility of achieving a design that serves distinct functions when excited from the forward and backward sides, thus embodying the concept of Janus metagratings.

Henceforth, in this section, the analysis and design of Janus metagratings will be continued based on the same excitation source and the metagrating structure depicted in Figure 4.10. Here, different combinations of the three cases of total transmission, total reflection, and total absorption are primarily considered, namely transmission under forward incidence/reflection under backward incidence, transmission under forward incidence/absorption under backward incidence, and absorption under forward incidence/reflection under backward incidence. The period Λ_y of the metagrating is also chosen to satisfy the condition where only the 0th diffraction mode is present, while other diffraction modes are evanescent. This condition necessitates that Λ_y should satisfy the relationship $\Lambda_y < \lambda_0$.

Unlike section 4.3, where only absorption was considered, in this context, transmission and reflection are also taken into account. For the amplitudes of the 0th diffraction modes in the upper and lower spaces of the metagrating under forward incidence, denoted by Eq.(4.39) and (4.40), they can be represented as $E_0^{\mathrm{UF}} = E_{\mathrm{in}}\mathrm{A}^{\mathrm{UF}}$ and $E_0^{\mathrm{LF}} = E_{\mathrm{in}}\mathrm{A}^{\mathrm{LF}}$, respectively. Similarly, for the amplitudes of the 0th diffraction modes in the upper and lower spaces of the metagrating under backward incidence, specified by Eq.(4.43) and (4.44), they can be expressed as $E_0^{\mathrm{UB}} = E_{\mathrm{in}}\mathrm{A}^{\mathrm{UB}}$ and $E_0^{\mathrm{LB}} = E_{\mathrm{in}}\mathrm{A}^{\mathrm{LB}}$, respectively. Consequently, Janus metagratings can be designed with distinct functionalities by assigning different values to A^{UF}, A^{LF}, A^{UB}, A^{LB}. For instance, in the case of considering transmission under forward incidence and reflection under backward incidence, the assignments are $\mathrm{A}^{\mathrm{UF}} = 0, \mathrm{A}^{\mathrm{LF}} = e^{j\varphi_{\mathrm{LF}}}, \mathrm{A}^{\mathrm{UB}} = 0, \mathrm{A}^{\mathrm{LB}} = e^{j\varphi_{\mathrm{LB}}}$, where φ_{LF} and $\varphi_{\mathrm{LB}} \in [0, 2\pi)$. Similarly, when considering transmission under forward incidence and absorption under backward incidence, the assignments are $\mathrm{A}^{\mathrm{UF}} = 0, \mathrm{A}^{\mathrm{LF}} = e^{j\varphi_{\mathrm{LF}}}, \mathrm{A}^{\mathrm{UB}} = 0, \mathrm{A}^{\mathrm{LB}} = 0$. Finally, in the scenario of absorption under forward incidence and reflection under backward incidence, the assignments are $\mathrm{A}^{\mathrm{UF}} = 0, \mathrm{A}^{\mathrm{LF}} = 0, \mathrm{A}^{\mathrm{UB}} = 0, \mathrm{A}^{\mathrm{LB}} = e^{j\varphi_{\mathrm{LB}}}$.

Next, an analysis is conducted on designing the metagratings to achieve different wavefront manipulations under forward incidence. Following the aforementioned discussion, $E_0^{\mathrm{UF}} = E_{\mathrm{in}}\mathrm{A}^{\mathrm{UF}}$ and $E_0^{\mathrm{LF}} = E_{\mathrm{in}}\mathrm{A}^{\mathrm{LF}}$ are substituted into Eqs.(4.39) and (4.40). Consequently,

the corresponding line currents can be derived as

$$I_{\mathrm{U}}^{\mathrm{F}} = \frac{\Lambda_0}{\eta_0} E_{\mathrm{in}} p' \tag{4.62}$$

$$I_{\mathrm{L}}^{\mathrm{F}} = \frac{\Lambda_0}{\eta_0} E_{\mathrm{in}} q' \tag{4.63}$$

with

$$p' = 2\frac{(1+\Gamma)(\Gamma - \mathrm{A}^{\mathrm{UF}}) - T(T - \mathrm{A}^{\mathrm{LF}})}{(1+\Gamma)^2 - T^2} \tag{4.64}$$

$$q' = 2\frac{T(1+\mathrm{A}^{\mathrm{UF}}) - (1+\Gamma)\mathrm{A}^{\mathrm{LF}}}{(1+\Gamma)^2 - T^2} \tag{4.65}$$

Then, by combining Eqs.(4.37), (4.38), (4.62) and (4.63), and Ohm's law $E^{\mathrm{tot}} = ZI$, the required load impedance density of the wires on the upper layer $Z_{\mathrm{U}}^{\mathrm{F}}$ and lower layer $Z_{\mathrm{L}}^{\mathrm{F}}$ can be calculated as

$$Z_{\mathrm{U}}^{\mathrm{F}} = \frac{\eta_0}{\Lambda_y}\frac{1+\Gamma}{p'} - Z_{\mathrm{self}} - \frac{q'}{p'} Z_{\mathrm{mutual}} \tag{4.66}$$

$$Z_{\mathrm{L}}^{\mathrm{F}} = \frac{\eta_0}{\Lambda_y}\frac{T}{q'} - Z_{\mathrm{self}} - \frac{p'}{q'} Z_{\mathrm{mutual}} \tag{4.67}$$

where Z_{self} and Z_{mutual} are defined as per Eqs.(4.53) and (4.54).

Similarly, the analysis for achieving different wavefront manipulations under backward incidence can also be conducted, following the approach used for forward incidence. Thus, for $E_0^{\mathrm{UB}} = E_{\mathrm{in}}\mathrm{A}^{\mathrm{UB}}$ and $E_0^{\mathrm{LB}} = E_{\mathrm{in}}\mathrm{A}^{\mathrm{LB}}$, the required load impedance density of the wires on the upper layer $Z_{\mathrm{U}}^{\mathrm{B}}$ and lower layer $Z_{\mathrm{L}}^{\mathrm{B}}$ can be derived as

$$Z_{\mathrm{U}}^{\mathrm{B}} = \frac{\eta_0}{\Lambda_y}\frac{T}{p''} - Z_{\mathrm{self}} - \frac{q''}{p''} Z_{\mathrm{mutual}} \tag{4.68}$$

$$Z_{\mathrm{L}}^{\mathrm{B}} = \frac{\eta_0}{\Lambda_y}\frac{1+\Gamma}{q''} - Z_{\mathrm{self}} - \frac{p''}{q''} Z_{\mathrm{mutual}} \tag{4.69}$$

with

$$p'' = 2\frac{T(1+\mathrm{A}^{\mathrm{LB}}) - (1+\Gamma)\mathrm{A}^{\mathrm{UB}}}{(1+\Gamma)^2 - T^2} \tag{4.70}$$

$$q'' = 2\frac{(1+\Gamma)(\Gamma - \mathrm{A}^{\mathrm{LB}}) - T(T - \mathrm{A}^{\mathrm{UB}})}{(1+\Gamma)^2 - T^2} \tag{4.71}$$

Parameters p', q', p'', q'' are generalized forms of parameters p and q in Eqs.(4.49) and (4.50). Whereas p and q are tailored for wave-absorption-only designs, p', q', p'', q'' encompass the potential for arbitrary wavefront manipulation designs

To actualize the designs of the Janus metagratings, it is imperative to ensure that the design of the meta-atoms remains consistent when simultaneously achieving the wavefront manipulations corresponding to forward and backward incidence, *i.e.*, $Z_{\mathrm{U}}^{\mathrm{F}} = Z_{\mathrm{U}}^{\mathrm{B}}$ and $Z_{\mathrm{L}}^{\mathrm{F}} = Z_{\mathrm{L}}^{\mathrm{B}}$. After a series of algebraic simplifications, a simplified equation can be derived as

$$(1+\Gamma)(p''-q')+T(q''-p')=0 \tag{4.72}$$

By solving the Eq. (4.72), solutions can be obtained that satisfy $Z_{\mathrm{U}}^{\mathrm{F}}=Z_{\mathrm{U}}^{\mathrm{B}}$ and $Z_{\mathrm{L}}^{\mathrm{F}}=Z_{\mathrm{L}}^{\mathrm{B}}$, thereby ensuring the feasibility of the Janus metagrating design scheme for the corresponding function.

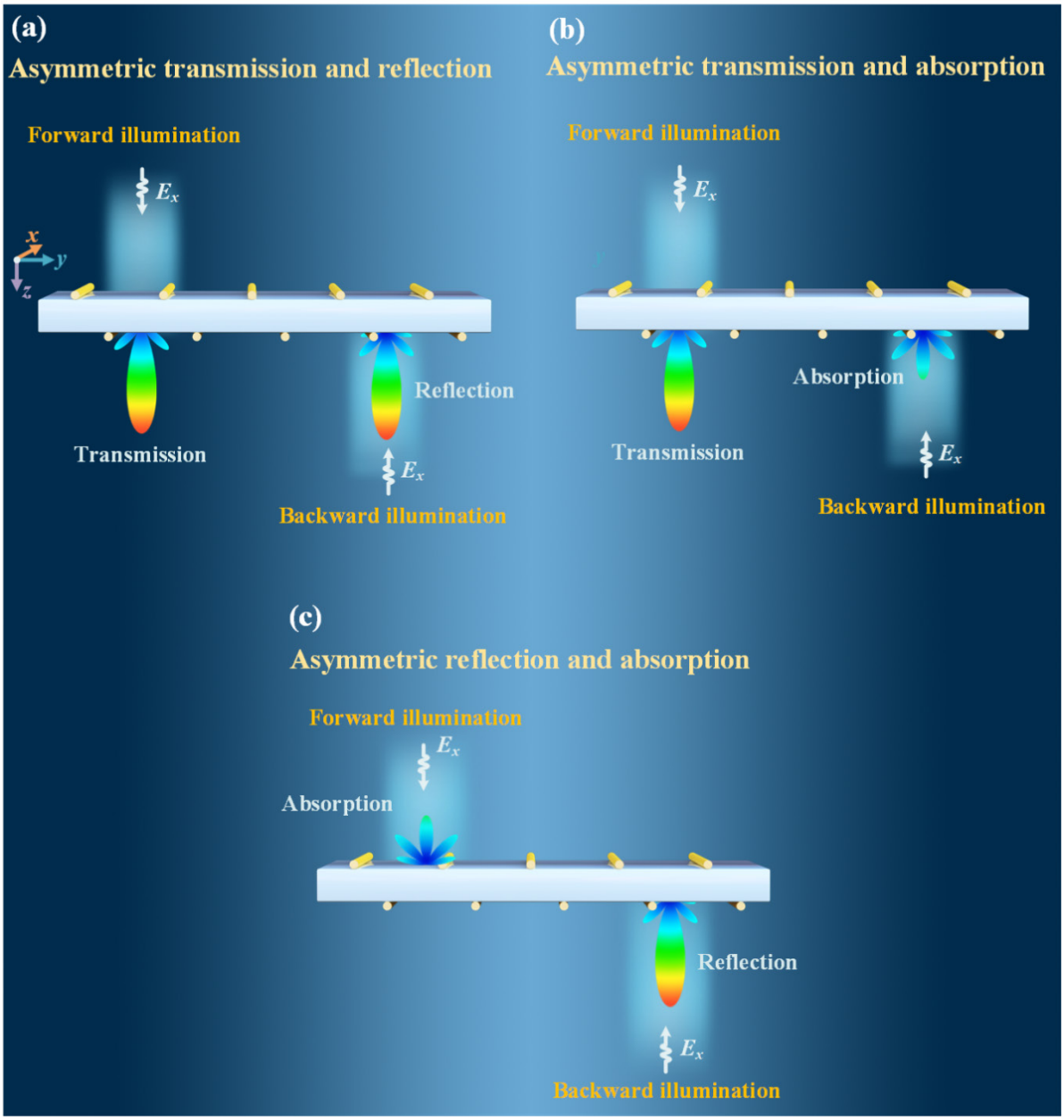

Figure 4.16: Janus metagrating wavefront manipulation conceptual diagram: (a) asymmetric transmission and reflection (b) asymmetric transmission and absorption, (b) asymmetric absorption and reflection.

4.4.2 Transmission under forward incidence and reflection under backward incidence

The scheme depicting asymmetric transmission and reflection is presented in Figure

4.16(a). Based on the analysis conducted in subsection 4.4.1, it is established that when considering transmission under forward incidence and reflection under backward incidence, the parameters are defined as follows: $\mathrm{A}^{\mathrm{UF}}=0,\mathrm{A}^{\mathrm{LF}}=e^{j\varphi_{\mathrm{LF}}},\mathrm{A}^{\mathrm{UB}}=0,\mathrm{A}^{\mathrm{LB}}=e^{j\varphi_{\mathrm{LB}}}$. By substituting these values into Eqs.(4.64), (4.65), (4.70) and (4.71), the parameters p',q',p'',q'' can be calculated. Then, by submitting them into Eqs. (4.72) and performing some algebraic simplifications, it is evident that $e^{j\varphi_{\mathrm{LF}}}=0$, which is clearly unsolvable. Thus, it can be concluded that the design of achieving transmission under forward incidence and reflection under backward incidence cannot be realized here.

4.4.3 Transmission under forward incidence and absorption under backward incidence

The scheme illustrating asymmetric transmission and absorption is depicted Figure 4.16(b). Based on the analysis conducted in subsection 4.4.1, it is established that when considering transmission under forward incidence and reflection under backward incidence, the parameters are defined as follows: $\mathrm{A}^{\mathrm{UF}}=0,\mathrm{A}^{\mathrm{LF}}=e^{j\varphi_{\mathrm{LF}}},\mathrm{A}^{\mathrm{UB}}=0,\mathrm{A}^{\mathrm{LB}}=0$. Subsequently, following the analysis in subsection 4.4.2, it is deduced that $e^{j\varphi_{\mathrm{LF}}}=0$, rendering the design unachievable.

4.4.4 Absorption under forward incidence and reflection under backward incidence

The scheme depicting asymmetric absorption and reflection is presented in Figure 4.16(c). According to the analysis conducted in subsection 4.4.1, when absorption under forward incidence and reflection under backward incidence are considered, the parameters are defined as follows: $\mathrm{A}^{\mathrm{UF}}=0,\mathrm{A}^{\mathrm{LF}}=0,\mathrm{A}^{\mathrm{UB}}=0,\mathrm{A}^{\mathrm{LB}}=e^{j\varphi_{\mathrm{LB}}}$. Similarly, following the analysis in subsection 4.4.2, it is found that Eq. (4.72) reduces to an identity in this scenario, indicating that the equations of $Z_{\mathrm{U}}^{\mathrm{F}}=Z_{\mathrm{U}}^{\mathrm{B}}$ and $Z_{\mathrm{L}}^{\mathrm{F}}=Z_{\mathrm{L}}^{\mathrm{B}}$ have identical solutions. Therefore, we can opt to solve either one of them. In this case, $Z_{\mathrm{U}}^{\mathrm{F}}=Z_{\mathrm{U}}^{\mathrm{B}}$ is chosen to solve, and it is obtained that

$$\frac{\eta_0}{\Lambda_y}\left(\frac{1+\Gamma}{p\prime}-\frac{T}{p\prime\prime}\right)-\left(\frac{q'}{p'}-\frac{q''}{p''}\right)Z_{\mathrm{mutual}}=0 \tag{4.73}$$

Next, $J=\frac{\eta_0}{\Lambda_y}\left(\frac{1+\Gamma}{p\prime}-\frac{T}{p\prime\prime}\right)-\left(\frac{q'}{p'}-\frac{q''}{p''}\right)Z_{\mathrm{mutual}}$ is defined as a complex number. Eq.(4.73) is then equated to $\Re(J)=0$ and $\Im(J)=0$. Such a system of equations contains two equations and four unknowns: d,Λ_y,h and φ_{LB}. Consequently, the values of two parameters can be arbitrarily determined, and then the values of the remaining two can be calculated. Considering the

symmetry of the position of the upper and lower meta-atoms of the metagrating, two types of metagratings are considered for the design, depending on whether the upper and lower meta-atoms are aligned or not.

First, let us consider the case where the top and bottom meta-atoms are not aligned, *i.e.*, $d \neq 0$. Although there is no strict limitation on the choice of parameters according to Eq.(4.73), certain inappropriate choices may render practical implementation complex or impossible, such as when the real part of the impedance density is negative. Therefore, we adopt the same selection strategy for the parameters as outlined in subsection 4.3, which involves considering parameters ensuring practical feasibility: the structure must maintain sparsity, *i.e.*, the period length Λ_y should not be less than $\lambda_0/2$, the thickness h of the substrate must be lower than $\lambda_0/10$, and finally, for a practical implementation, the real part of the impedance density should not be negative. Following judicious parameter screening, the period of the metagrating Λ_y and the thickness of the substrate h are chosen as $\Lambda_y = 16$ mm and $h = 2$ mm, respectively. Subsequently, the spacing between the two meta-atoms $d = 1.46$ mm and the parameter $\varphi_{LB} = 2.1951$ rad can be calculated according to $\Re(J) = 0$ and $\Im(J) = 0$. Then, the required impedance densities of the two meta-atoms can be calculated via Eqs.(4.66) and (4.67), or Eqs. (4.68) and (4.69), as $Z_U = -j4.3926\ \eta/\lambda$ and $Z_L = (0.2752 - j3.8552)\ \eta/\lambda$, respectively.

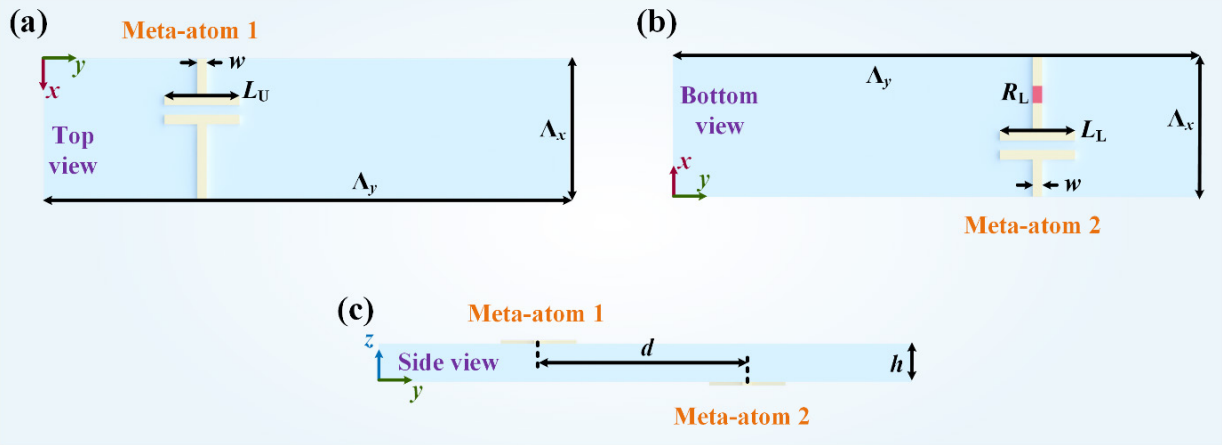

Figure 4.17: Supercell of the Janus metagratings: (a) Top view. (b) Bottom view. (c) Side view.

To realize the required load impedance densities, the microstrip capacitor model and the model with a microstrip capacitor in series with a 01005 series chip resistor are utilized to implement the meta-atoms, respectively. Different views of the supercell are shown in Figure 4.17.

Table 4.4 Parameters of Janus metagrating supercells

Parameters \ Supercell type		$d \neq 0$	$d = 0$	$d = 0$ (Exp)
Λ_x (mm)		3	3	3
Λ_y (mm)		16	16	16
h (mm)		2	2.53	2.5
d (mm)		1.46	0	0
φ_{LB} (rad)		2.1951	1.8504	2.3000
w (mm)		0.2	0.2	0.2
Z_U (η/λ)		-j4.3926	-j4.4301	-j4.300
Z_L (η/λ)		0.2752-j3.8552	0.3938-j3.9073	0.3500-j4.0000
L_U (mm)	CV	3.78	3.75	3.86
	OV	3.59	3.60	3.6
L_L (mm)	CV	4.31	4.25	4.15
	OV	4.01	3.99	4
R_L (Ω)	CV	10.37	14.85	13.19
	OV	7.57	10.84	11.5

CV: calculated value; OV: optimal value.

Then, the capacitor arm length and resistance of the corresponding meta-atoms can be calculated via Eqs.(3.20), (3.29) as: L_U = 3.78 mm, L_L = 4.31 mm and R_L = 10.37 Ω. As in subsection 4.3, considering that the metal strip capacitor structure inevitably introduces a small amount of impedance density in the real part, the final parameters L and R need to be optimized in ANSYS HFSS to achieve the optimum results. These values are represented as CV (calculated value) and OV (optimal value), respectively, and are listed in Table 4.4.

The simulation results of both forward and backward illuminations of the supercell are depicted in Figure 4.18(a), where Γ denotes reflection and T denotes transmission, while absorption is calculated using the formula $A = 1-\Gamma-T$. The simulation results illustrate that the absorption under forward incidence aligns well with expectations, whereas under backward illumination, 96% reflection efficiency is observed. The transmission curves exhibit consistent behavior for both forward and backward incidences. In comparison to the previous design shown in Figure 4.13(a), where only uni-directional wave absorption is considered, the current analysis introduces an additional design aspect aimed at achieving total reflection under backward incidence in Janus metagratings. Consequently, the final results demonstrate effectiveness, as the loss of reflection decreases from approximately 20% to 4%.

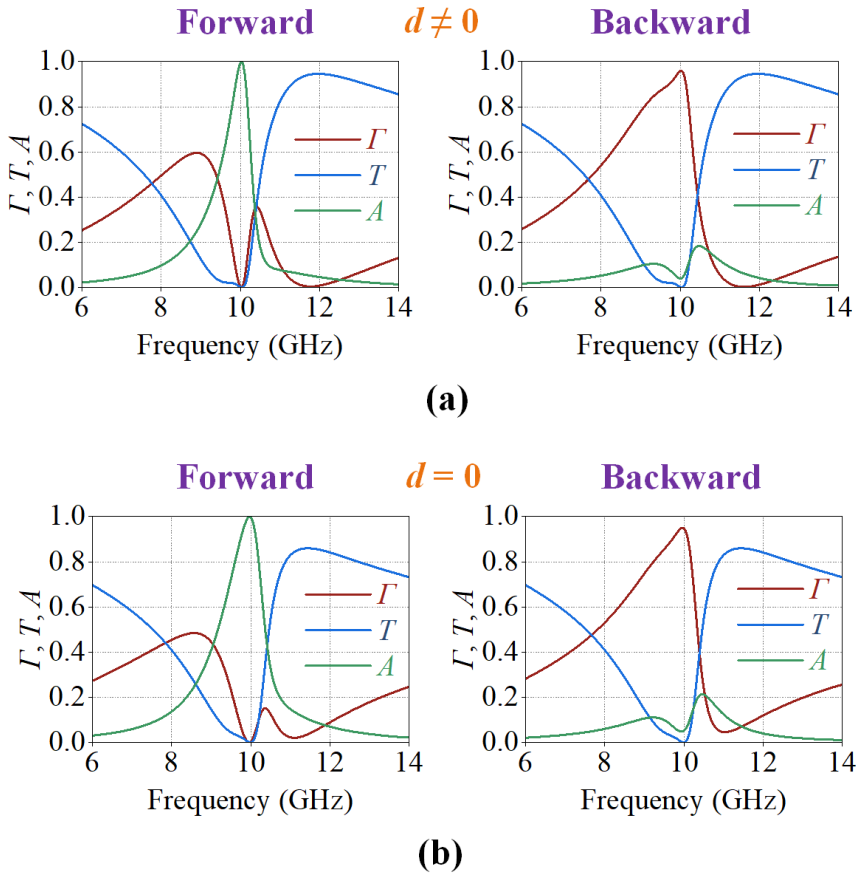

Figure 4.18: Simulation results of the supercell with optimized parameters for bi-directional absorption. (a) $d \neq 0$, and (b) $d = 0$.

Then, the design where the meta-atoms are aligned both above and below, *i.e.*, $d = 0$, is considered. Given that d, Λ_y, h and φ_{LB} are mutually determining factors, after setting $d = 0$, the sparsity of the metagrating is prioritized. Hence, the period Λ_y is also chosen Λ_y = 16mm. Subsequently, the thickness h and the parameter φ_{LB} are calculated as h = 2.53mm and φ_{LB} = 1.8504 rad , respectively, meeting the low-profile requirement of metagratings (h is smaller than λ_0/ 10). Then, the required impedance densities of the two meta-atoms are calculated as Z_U = - j4.4301 η/λ and Z_L = (0.3938 – j3.9073) η/λ, respectively. The corresponding parameters of the meta-atoms are calculated as: L_U = 3.75 mm, L_L = 4.25 mm, R_L = 14.85 Ω, which are further optimized in simulations.

The simulation results for both forward and backward illuminations of the supercell are presented in Figure 4.18(b). These results reveal that the absorption under forward incidence aligns well with expectations, while under backward illumination, a 95% reflection efficiency is observed. The higher reflection loss observed here compared to the case where $d \neq 0$ may be attributed to the utilization of a larger resistor value R_L, as indicated in Table 4.4. Additionally, the larger resistance contributes to a wider absorption bandwidth for d = 0 under forward

illumination compared to the case where $d \neq 0$.

4.4.5 Experiments and discussions

For a proof-of-concept validation, the $d = 0$ Janus metagrating structure for asymmetrical absorption and reflection is considered for fabrication using PCB technique. The resistance value can be approached using the commercial 01005 series chip resistor. Concerning the dielectric substrate, all parameters are obtained based on a rigorous solution of the equations. Since the parameter h is fixed for commercially available substrates, this means that the equation will be unsolvable. The original substrate thickness h = 2.53 mm is adjusted to a commercially available value of 2.5 mm. Then, the optimal solution is searched by the nonlinear least-squares lsqnonlin solver in Matlab. After finding the optimal value of the impedance densities Z_U = -j4.300 η/λ and Z_L = (0.3500-j4.0000) η/λ that simultaneously maximize both absorption under forward incidence and reflection under backward incidence, the parameters of the meta-atoms can be calculated and optimized to complete the design process, and are listed in Table 4.4.

Then the d = 0 Janus metagrating is fabricated and chip resistors are integrated. The fabricated prototype consists of 100 × 37 supercells in x- and y-directions, corresponding to 300 mm × 592 mm. Zoom views of the top and bottom faces of the prototype are displayed in Figure 4.19(a). The experimental setup and measurement procedure are identical to those described in subsection 4.3.4. The simulation and measurement results are compared in Figure 4.19(b).

Although some unavoidable deviations in fabrication and the limited size of the metagrating sample may have resulted in discrepancies between the measurement and simulation results, it is evident that the fabricated Janus metagrating board exhibits favorable wave absorption characteristics under forward incidence, as well as satisfactory reflection characteristics under backward incidence at the working frequency of 10 GHz.

It should be noted that although only Janus metagratings with different combinations of transmission, reflection, and absorption are considered in the analysis and design in this section, designs of Janus metagratings with asymmetric transmission and reflection as well as asymmetric transmission and absorption were excluded by the analytical result. However, this limitation stems from the assumption that each supercell contains only two meta-atoms. It is foreseeable that by increasing the number of meta-atoms within each supercell in future iterations, the design freedom may be augmented, thus enabling the realization of asymmetric transmission and reflection, as well as asymmetric transmission and absorption.

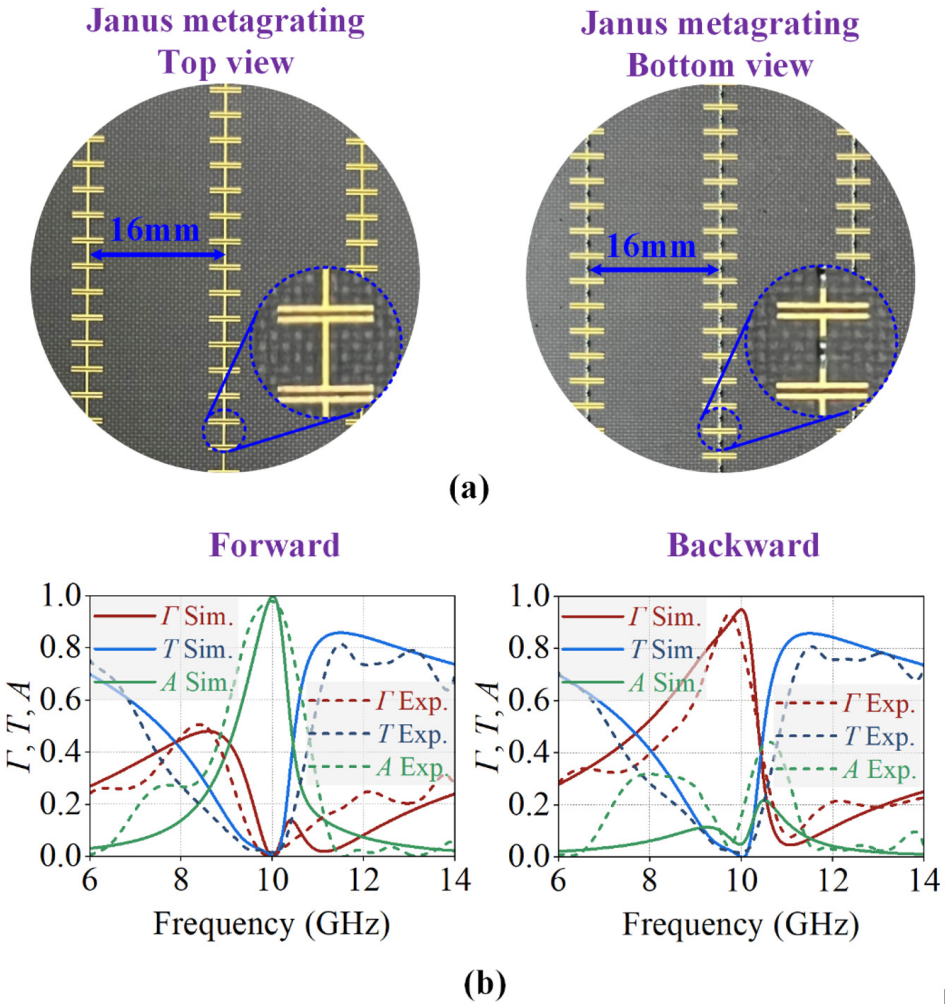

Figure 4.19: (a) Top and bottom views of the fabricated Janus metagrating for asymmetrical absorption / reflection. (b) Simulated and measured reflection Γ, transmission T, and absorption A coefficients under forward and backward illuminations.

Furthermore, the methodology outlined in this study can serve as a foundation for exploring the design of more versatile Janus metagratings. For instance, by judiciously selecting values for A^{UF}, A^{LF}, A^{UB}, A^{LB}, Janus metagratings with varying ratios of reflection, transmission, and absorption can be actualized. For example, designs featuring 50% reflection and 50% transmission under forward incidence, coupled with 10% reflection and 90% transmission under backward incidence, can be pursued, among other configurations.

4.5 Conclusion

In this chapter, I have embarked on a series of wavefront manipulation designs utilizing transmissive metagratings. These designs span anomalous refraction, anomalous reflection, beam splitting, uni- and bi-directional wave absorption, and asymmetrical reflection and

absorption. Rooted in fully analytical design schemes, these closed-form analytical formulations serve as a robust theoretical foundation for crafting diverse wavefront manipulations based on transmissive metagratings.

Compared to existing approaches in wavefront manipulation with transmissive metagratings, this chapter introduces a more intuitive fully analytical design methodology for anomalous reflection, anomalous refraction, and beam splitting. Moreover, the realization of uni- and bi-directional wave absorption and Janus metagrating wavefront manipulation represents novel contributions in this chapter.

Experimental verification is conducted for all designs presented herein, except for beam splitting, to ensure their validity and correctness. The favorable agreement between experimental results and theoretical predictions underscores the significant promise of wavefront manipulation designs based on transmissive metagratings for various applications, including future wireless communications, radar detection, electromagnetic stealth, and beyond. This promise is underpinned by the simplicity and sparsity of the metagrating structure itself, alongside the utilization of advanced analytical models facilitating effective and swift design across diverse frequency bands.

General conclusions and outlooks

In the course of my PhD research, I have focused on metagratings for efficient wavefront manipulation. Detailed workflows have been developed for the design of metagratings, utilizing an analytical framework and simulation estimation. These methodologies have been applied to realize proof-of-concept prototypes, with experimental validation presented and thoroughly discussed. The work started with an introduction to the state-of-the-art on metamaterials and metasurfaces in Chapter 1, where the concept of metagratings, an advanced design methodology for efficient wavefront manipulation, has been detailed. Chapter 2 has provided a theoretical background on metagratings based on Maxwell’s equations and Ohm’s law, serving as the foundation for subsequent design efforts in Chapters 3 and 4, which respectively focused on reflective and transmissive metagratings for efficient wavefront manipulation.

To summarize, Chapter 1 has offered a historical view on metamaterial development, tracing back to Veselago's pioneering work on negative refractive index materials in 1968 and culminating in the experimental validation of metamaterials in the early 2000 s. The emergence of metasurfaces, conducted by Capasso's concept of generalized Snell's law in 2011, marked a significant milestone in wave manipulation, enabling precise control of electromagnetic wavefronts. Chapter 2 has dealt with the analysis of electromagnetic characteristics within metagratings, focusing on plane wave incidence and planar periodic structures. Four key aspects were examined: multilayer media reflection/transmission, radiated field analysis of polarization currents, load impedance design, and period length optimization for efficient diffraction. Reflective metagratings have been studied in Chapter 3, elucidating design methodologies for single and multi-beam generation, and electromagnetic absorption. Special attention has been given to zero load-impedance metagratings, offering a practical solution for high frequencies. Chapter 4 has extended the investigation to transmissive metagratings, which presented additional challenges due to the presence of both reflection and transmission diffraction modes. Design strategies for single and multi-beam manipulation, as well as electromagnetic absorption, have bben discussed. Notably, the concept of Janus metagratings has been introduced, paving the way for asymmetric wavefront manipulation.

In conclusion, this thesis has established a comprehensive framework for metagrating design, addressing fundamental wavefront manipulation challenges. The exploration of reflective and transmissive metagratings has demonstrated their efficiency in achieving diverse wavefront manipulations, validated through simulations and experiments. This work not only advances theoretical understanding but also holds significant implications for practical applications in electromagnetic wavefront manipulation. Exciting opportunities for further innovation and progress in metagratings research are anticipated, promising new horizons in the field.

While this thesis has provided significant efforts in advancing the analytical designs of metagratings, there remain avenues for further exploration and improvement. Future research in this field can consider the following ideas:

- **Multifunctional metagratings:** Investigate designs that simultaneously achieve multiple functionalities, enhancing the versatility and utility of metagratings in practical applications.
- **Dynamic metagratings:** Explore the feasibility of metagratings with dynamic, reconfigurable properties, allowing adaptive wavefront control in response to changing environmental conditions or application requirements.
- **Integration with emerging technologies:** Investigate the integration of metagratings with emerging technologies such as artificial intelligence and machine learning to optimize designs and enhance performance.
- **Broader frequency ranges:** Extend the analytical designs to cover broader frequency ranges, enabling the application of metagratings in diverse electromagnetic spectrum domains.
- **Practical antenna applications:** Address challenges related to the practical implementation of metagratings in antenna applications, including antenna aperture as well as antenna feed techniques.

List of publications

Publications in scientific journals

As First Author

1. **Z. Tan**, J. Yi, Q. Cheng, and S. N. Burokur, *Design of Perfect Absorber Based on Metagratings: Theory and Experiment*, IEEE Trans. Antennas Propag. 71, 1832 (2023).
2. **Z. Tan**, J. Yi, S. Wang, X. Chen, and S. N. Burokur, *Closed-Form Analytical Design of a Beamforming Reflective Metagrating with a Relatively Low Number of Meta-Atoms*, Opt. Mater. Express 13, 624 (2023).
3. **Z. Tan**, J. Yi, X. Chen, M. Lin, Z. H. Jiang, D. H. Werner, and S. N. Burokur, *Fully Analytical Design of Dual-Wire PCB Metagratings for Beam Steering and Splitting*, IEEE Trans. Antennas Propag. 71, 5452 (2023).
4. **Z. Tan**, J. Yi, V. Popov, and S. N. Burokur, *Efficient Beam Splitting Using Zero-Load-Impedance Metagratings*, Opt. Lett. 48, 3275 (2023).
5. **Z. Tan**, J. Yi, B. Ratni, and S. N. Burokur, *Fully Analytical Design of Electromagnetic Transmissive Metagratings for Highly Efficient Extreme-Angle Beam Refraction and Reflection*, Phys. Rev. Applied, 21, 024009 (2024).

As contributor

6. J. Yi, W. Zhou, **Z. Tan**, M. Lin, X. Chen, and S. N. Burokur, *Dual-Polarized Metagrating for Controlling Diffraction Patterns in Orthogonal Planes*, IEEE Trans. Antennas Propag. 71, 8753 (2023).
7. L. Zhu, R. Dai, J. Yi, X. Chen, **Z. Tan**, M. Lin, and S. N. Burokur, *Bifunctional Microwave Metagrating Used as Reflectarray for Diffraction Pattern Manipulation*, IEEE Antennas Wireless Propag. Lett. 22, 2155 (2023).
8. S. Wang, S. Xuan, **Z. Tan**, B. Xue, J. Yi, X. Chen, and S. N. Burokur, *Design and Validation of a Metagrating for Dual Operation*, IEEE Antennas Wireless Propag. Lett. **22**, 3003 (2023).

International conferences

1. **Z. Tan** and J. Yi, *Generalized Analytical Approach for Designing Printed Circuit Board Metagratings*, in *2022 International Conference on Microwave and Millimeter Wave Technology (ICMMT)* (IEEE, Harbin, China, 2022).
2. **Z. Tan**, J. Yi, B. Ratni, and S. N. Burokur, *Anomalous Reflection or Refraction Based on Transmissive Metagratings with Few Meta-Atoms*, in *2023 IEEE International Symposium on Antennas and Propagation and USNC-URSI Radio Science Meeting (USNC-URSI)* (IEEE, Portland, OR, USA, 2023).
3. **Z. Tan**, J. Yi, B. Ratni, and S. N. Burokur, *Asymmetric Electromagnetic Absorption and Reflection Based on Transmissive Metagratings*, in *2023 IEEE International Symposium on Antennas and Propagation and USNC-URSI Radio Science Meeting (USNC-URSI)* (IEEE, Portland, OR, USA, 2023).
4. **Z. Tan**, J. Yi, B. Ratni, and S. N. Burokur, *Dual-Polarized Metagrating Absorbers*, in *2023 XXXVth General Assembly and Scientific Symposium of the International Union of Radio Science (URSI GASS)* (IEEE, Sapporo, Japan, 2023).
5. **Z. Tan**, J. Yi, B. Ratni, and S. N. Burokur, *Transmissive-type Metagratings with Few Meta-Atoms for Beam Splitting*, in *2024 18th European Conference on Antennas and Propagation (EuCAP)* (IEEE, Glasgow, Scotland, 2024).

Bibliography

[1] V. G. Veselago, *The Electrodynamics of Substances with Simultaneously Negative Values of e and m*, Sov. Phys. Usp. **10**, 509 (1968).

[2] J. B. Pendry, A. J. Holden, W. J. Stewart, and I. Youngs, *Extremely Low Frequency Plasmons in Metallic Mesostructures*, Phys. Rev. Lett. **76**, 4773 (1996).

[3] J. B. Pendry, A. J. Holden, D. J. Robbins, and W. J. Stewart, *Magnetism from Conductors and Enhanced Nonlinear Phenomena*, IEEE Transactions on Microwave Theory and Techniques **47**, 2075 (1999).

[4] R. A. Shelby, D. R. Smith, and S. Schultz, *Experimental Verification of a Negative Index of Refraction*, Science **292**, 77 (2001).

[5] J. B. Pendry, D. Schurig, and D. R. Smith, *Controlling Electromagnetic Fields*, Science **312**, 1780 (2006).

[6] U. Leonhardt, *Optical Conformal Mapping*, Science **312**, 1777 (2006).

[7] D. Schurig, J. J. Mock, B. J. Justice, S. A. Cummer, J. B. Pendry, A. F. Starr, and D. R. Smith, *Metamaterial Electromagnetic Cloak at Microwave Frequencies*, Science **314**, 977 (2006).

[8] N. Yu, P. Genevet, M. A. Kats, F. Aieta, J.-P. Tetienne, F. Capasso, and Z. Gaburro, *Light Propagation with Phase Discontinuities: Generalized Laws of Reflection and Refraction*, Science **334**, 333 (2011).

[9] N. Yu, F. Aieta, P. Genevet, M. A. Kats, Z. Gaburro, and F. Capasso, *A Broadband, Background-Free Quarter-Wave Plate Based on Plasmonic Metasurfaces*, Nano Lett. **12**, 6328 (2012).

[10] X. Ni, A. V. Kildishev, and V. M. Shalaev, *Metasurface Holograms for Visible Light*, Nat Commun **4**, 2807 (2013).

[11] L. Liu, X. Zhang, M. Kenney, X. Su, N. Xu, C. Ouyang, Y. Shi, J. Han, W. Zhang, and S. Zhang, *Broadband Metasurfaces with Simultaneous Control of Phase and Amplitude*, Advanced Materials **26**, 5031 (2014).

[12] S. Sun, Q. He, S. Xiao, Q. Xu, X. Li, and L. Zhou, *Gradient-Index Meta-Surfaces as a Bridge Linking Propagating Waves and Surface Waves*, Nature Mater **11**, 426 (2012).

[13] W. Luo, S. Xiao, Q. He, S. Sun, and L. Zhou, *Photonic Spin Hall Effect with Nearly 100% Efficiency*, Advanced Optical Materials **3**, 1102 (2015).

[14] N. M. Estakhri and A. Alù, *Recent Progress in Gradient Metasurfaces*, J. Opt. Soc. Am. B **33**, A21 (2016).

[15] C. Pfeiffer and A. Grbic, *Metamaterial Huygens' Surfaces: Tailoring Wave Fronts with Reflectionless Sheets*, Phys. Rev. Lett. **110**, 197401 (2013).

[16] M. Selvanayagam and G. V. Eleftheriades, *Discontinuous Electromagnetic Fields Using Orthogonal Electric and Magnetic Currents for Wavefront Manipulation*, Opt. Express **21**, 14409 (2013).

[17] A. Epstein and G. V. Eleftheriades, *Huygens' Metasurfaces via the Equivalence Principle: Design and Applications*, J. Opt. Soc. Am. B **33**, A31 (2016).

[18] M. Selvanayagam and George. V. Eleftheriades, *Circuit Modeling of Huygens Surfaces*, Antennas Wirel. Propag. Lett. **12**, 1642 (2013).

[19] J. P. S. Wong, M. Selvanayagam, and G. V. Eleftheriades, *Design of Unit Cells and Demonstration of Methods for Synthesizing Huygens Metasurfaces*, Photonics and Nanostructures - Fundamentals and Applications **12**, 360 (2014).

[20] S. L. Jia, X. Wan, X. J. Fu, Y. J. Zhao, and T. J. Cui, *Low-Reflection Beam Refractions by Ultrathin Huygens Metasurface*, AIP Advances **5**, 067102 (2015).

[21] Y. Ra'di, V. S. Asadchy, and S. A. Tretyakov, *One-Way Transparent Sheets*, Phys. Rev. B **89**, 075109 (2014).

[22] M. Kim, A. M. H. Wong, and G. V. Eleftheriades, *Optical Huygens' Metasurfaces with Independent Control of the Magnitude and Phase of the Local Reflection Coefficients*, Phys. Rev. X **4**, 041042 (2014).

[23] M. Selvanayagam and G. V. Eleftheriades, *Polarization Control Using Tensor Huygens Surfaces*, IEEE Trans. Antennas Propagat. **62**, 6155 (2014).

[24] A. Epstein and G. V. Eleftheriades, *Passive Lossless Huygens Metasurfaces for Conversion of Arbitrary Source Field to Directive Radiation*, IEEE Trans. Antennas Propagat. **62**, 5680 (2014).

[25] A. Epstein, J. P. S. Wong, and G. V. Eleftheriades, *Cavity-Excited Huygens' Metasurface Antennas for near-Unity Aperture Illumination Efficiency from Arbitrarily Large Apertures*, Nat Commun **7**, 10360 (2016).

[26] Y. Ra'di, D. L. Sounas, and A. Alù, *Metagratings: Beyond the Limits of Graded Metasurfaces for Wave Front Control*, Phys. Rev. Lett. **119**, 067404 (2017).

[27] A. Epstein and O. Rabinovich, *Unveiling the Properties of Metagratings via a Detailed Analytical Model for Synthesis and Analysis*, Phys. Rev. Applied **8**, 054037 (2017).

[28] O. Rabinovich and A. Epstein, *Analytical Design of Printed Circuit Board (PCB) Metagratings for Perfect Anomalous Reflection*, IEEE Trans. Antennas Propagat. **66**, 4086 (2018).

[29] O. Rabinovich, I. Kaplon, J. Reis, and A. Epstein, *Experimental Demonstration and In-Depth Investigation of Analytically Designed Anomalous Reflection Metagratings*, Phys. Rev. B **99**, 125101 (2019).

[30] V. Popov, F. Boust, and S. N. Burokur, *Controlling Diffraction Patterns with Metagratings*, Phys. Rev. Applied **10**, 011002 (2018).

[31] V. Popov, F. Boust, and S. N. Burokur, *Constructing the Near Field and Far Field with Reactive Metagratings: Study on the Degrees of Freedom*, Phys. Rev. Applied **11**, 024074 (2019).

[32] V. Popov, M. Yakovleva, F. Boust, J.-L. Pelouard, F. Pardo, and S. N. Burokur, *Designing Metagratings via Local Periodic Approximation: From Microwaves to Infrared*, Phys. Rev. Applied **11**, 044054 (2019).

[33] V. Popov, F. Boust, and S. N. Burokur, *Beamforming with Metagratings at Microwave Frequencies: Design Procedure and Experimental Demonstration*, IEEE Trans. Antennas Propagat. **68**, 1533 (2020).

[34] A. Casolaro, A. Toscano, A. Alu, and F. Bilotti, *Dynamic Beam Steering With Reconfigurable Metagratings*, IEEE Trans. Antennas Propagat. **68**, 1542 (2020).

[35] O. Rabinovich and A. Epstein, *Arbitrary Diffraction Engineering With Multilayered Multielement Metagratings*, IEEE Trans. Antennas Propagat. **68**, 1553 (2020).

[36] G. Xu, G. V. Eleftheriades, and S. V. Hum, *Analysis and Design of General Printed Circuit Board Metagratings With an Equivalent Circuit Model Approach*, IEEE Trans. Antennas Propagat. **69**, 4657 (2021).

[37] O. Rabinovich and A. Epstein, *Nonradiative Subdiffraction Near-Field Patterns Using*

Metagratings, Appl. Phys. Lett. **118**, 131105 (2021).

[38] Y. Raadi and A. Alu, *Metagratings for Efficient Wavefront Manipulation*, IEEE Photonics J. **14**, 2207513 (2022).

[39] A. Díaz-Rubio, V. S. Asadchy, A. Elsakka, and S. A. Tretyakov, *From the Generalized Reflection Law to the Realization of Perfect Anomalous Reflectors*, Sci. Adv. **3**, e1602714 (2017).

[40] H. W. Tian, X. G. Zhang, W. X. Jiang, X. Li, Y. K. Liu, C. Qiu, and T. J. Cui, *Programmable Controlling of Multiple Spatial Harmonics via a Nonlinearly Phased Grating Metasurface*, Adv Funct Materials **32**, 2203120 (2022).

[41] Y. Wang, Y. Yuan, Y. Liu, X. Ding, B. Ratni, Q. Wu, S. N. Burokur, G. Hu, and K. Zhang, *Extreme Diffraction Management in Phase-Corrected Gradient Metasurface by Fourier Harmonic Component Engineering*, Laser & Photonics Reviews **17**, 2300152 (2023).

[42] V. Popov, S. N. Burokur, and F. Boust, *Conformal Sparse Metasurfaces for Wavefront Manipulation*, Phys. Rev. Applied **14**, 044007 (2020).

[43] F. Villamizar, C. Martel, F. Boust, and S. N. Burokur, *Sparse Metasurfaces for Scattering Cross Section Reduction of Arbitrarily Shaped Metallic Bodies*, ACS Appl. Electron. Mater. **5**, 2259 (2023).

[44] V. Popov, B. Ratni, S. N. Burokur, and F. Boust, *Non-Local Reconfigurable Sparse Metasurface: Efficient Near-Field and Far-Field Wavefront Manipulations*, Advanced Optical Materials **9**, 2001316 (2021).

[45] S. Tretyakov, *Analytical Modeling in Applied Electromagnetics*. Artech House, Boston (2003).

[46] G. Xu, S. V. Hum, and G. V. Eleftheriades, *Dual-Band Reflective Metagratings With Interleaved Meta-Wires*, IEEE Trans. Antennas Propagat. **69**, 2181 (2021).

[47] Z. Tan, J. Yi, S. Wang, X. Chen, and S. N. Burokur, *Closed-Form Analytical Design of a Beamforming Reflective Metagrating with a Relatively Low Number of Meta-Atoms*, Opt. Mater. Express **13**, 624 (2023).

[48] Z. Tan, J. Yi, X. Chen, M. Lin, Z. H. Jiang, D. H. Werner, and S. N. Burokur, *Fully Analytical Design of Dual-Wire PCB Metagratings for Beam Steering and Splitting*, IEEE Trans. Antennas Propagat. **71**, 5452 (2023).

[49] F. Boust, T. Lepetit, and S. N. Burokur, *Metagrating Absorber: Design and Implementation*, Opt. Lett. **47**, 5305 (2022).

[50] E. G. Loewen and E. Popov, *Diffraction Gratings and Applications*, Boca Raton, FL, USA: CRC Press (1997).

Université Paris Nanterre | École doctorale Connaissance, langage, modélisation

Titre : Métaréseaux électromagnétiques pour la manipulation efficace de fronts d'onde
Mots clés : métaréseau, rayonnement électromagnétique, fronts d'onde, absorption

Résumé : Par rapport aux métasurfaces traditionnelles, les métaréseaux ont démontré des avantages prononcés dans la manipulation efficace du front d'onde au cours de ces dernières années. Ces avantages découlent principalement de deux facteurs clés : premièrement, les métaréseaux éliminent efficacement la désadaptation d'impédance d'onde entre les ondes entrantes et sortantes, permettant ainsi d'avoir une efficacité quasi-optimale dans la manipulation du front d'onde. Deuxièmement, la structure simplifiée et éparse des métaréseaux les rend beaucoup plus faciles à réaliser que les métasurfaces traditionnelles, qui impliquent souvent des exigences de résolution structurelle complexes, en particulier à des fréquences élevées.

Cette thèse s'efforce d'établir une méthodologie de conception plus intuitive et plus rigoureuse pour la manipulation du front d'onde basée sur les métaréseaux, tout en explorant de nouvelles voies dans le domaine. Menée conjointement par l'Université Paris Nanterre et Xi'an Jiaotong University, l'étude commence par une analyse complète des caractéristiques électromagnétiques inhérentes aux métaréseaux, visant à clarifier les principes fondamentaux régissant la manipulation du front d'onde. Cette analyse englobe la dérivation des coefficients de réflexion et de transmission dans les milieux multicouches, l'analyse des caractéristiques du rayonnement et des considérations méticuleuses pour obtenir une manipulation optimale du front d'onde.

Les travaux de recherche portent sur les subtilités de la conception des métaréseaux réfléchissants, en abordant les défis et en concevant des stratégies pour les rayonnements mono- et multi-faisceaux et pour l'absorption électromagnétique, en explorant l'influence de diverses configurations structurelles sur la bande passante d'absorption. Notamment, le concept de métaréseaux à impédance de charge nulle est introduit et des applications potentielles sont explorées, en particulier dans les scénarios à hautes fréquences. Enfin, les travaux de recherche étendent leur exploration aux métaréseaux transmissifs, dans le but de démontrer leurs capacités à réaliser diverses manipulations, englobant la réflexion anormale, la réfraction anormale, la division du faisceau, l'absorption d'ondes unidirectionnelle et bidirectionnelle et la manipulation asymétrique du front d'onde.

Title : Electromagnetic metagratings for efficient wavefront manipulation
Keywords : metagrating, electromagnetic radiation, wavefront, absorption

Abstract: Compared to traditional metasurfaces, metagratings have demonstrated pronounced advantages in efficient wavefront manipulation in recent years. These advantages primarily stem from two key factors: first, metagratings effectively eliminate wave impedance mismatch between incoming and outgoing waves, thus facilitating near-optimal efficiency in wavefront manipulation. Second, the sparsely arranged and simplified structure of metagratings renders them significantly easier to fabricate compared to traditional metasurfaces, which often entail complex structural resolution requirements particularly at high frequencies.

This doctoral research endeavors to establish a more intuitive and rigorous design methodology for metagrating-based wavefront manipulation while also exploring novel avenues in the domain. Conducted jointly by Université Paris Nanterre and Xi'an Jiaotong University, the study starts with a comprehensive analysis of the electromagnetic characteristics inherent to metagratings, aiming to elucidate the fundamental principles governing wavefront manipulation. This analysis encompasses the derivation of reflection and transmission coefficients in multilayered media, examination of radiation characteristics, and meticulous considerations for achieving optimal wavefront manipulation.

Subsequent investigations deal with the design intricacies of reflective metagratings, addressing challenges and devising strategies for both single-beam and multi-beam radiations and for electromagnetic absorption, exploring the influence of diverse structural configurations on absorption bandwidth. Notably, the concept of zero load-impedance metagratings is introduced and potential applications are explored particularly in high-frequency band scenarios. Finally, the research extends its exploration to transmissive metagratings, aiming to demonstrate their capabilities in achieving diverse wavefront manipulations, encompassing anomalous reflection, anomalous refraction, beam splitting, uni- and bi-directional wave absorption, and asymmetrical wavefront manipulation.